Determination of Rainfall Parameters for Specific Attenuation Due to Rain for Different Integration Times for Terrestrial Line-of-Sight Links in South Africa

By

Mary Nabangala

Dissertation submitted in fulfillment of the requirement for the degree

MASTER OF SCIENCE IN ENGINEERING: ELECTRONIC ENGINEERING

UNIVERSITY OF KWAZULU-NATAL

March, 2016

Supervisor:

Prof. Thomas Joachim Odhiambo Afullo

Co-supervisor:

Dr. Akintunde Ayodeji Alonge

As the candidate's Supervisors we agree to the submission of this dissertation

Prof. Thomas Joachim Odhiambo Afullo

Signed …… Date: …….

Dr. Akintunde Ayodeji Alonge

Signed …… Date: …….

Declaration 1 - Plagiarism

I, **Mary Nabangala**, declare that:

1. The research reported in this dissertation, except where otherwise indicated, is my original research.
2. This dissertation has not been submitted for any degree or examination at any other university.
3. This dissertation does not contain other persons' data, pictures, graphs or other information, unless specifically acknowledged as being sourced from other persons.
4. This dissertation does not contain other persons' writing, unless specifically acknowledged as being sourced from other researchers. Where other written sources have been quoted, then:
    a) their words have been re-written but the general information attributed to them has been referenced;
    b) where their exact words have been used, their writing has been placed inside quotation marks, and referenced.
5. Where I have reproduced a publication of which I am an author, co-author or editor, I have indicated in detail which part of the publication was actually written by myself alone and have fully referenced such publications.
6. This dissertation does not contain text, graphics or tables copied and pasted from the Internet, unless specifically acknowledged, and the source being detailed in the dissertation and in the References sections.

Signed …… Date: …….

Mary Nabangala

Declaration 2 - Publications

Mary N. Ahuna, Thomas J. Afullo, Akintunde A. Alonge, "30-Second Integration Time Power Law Conversion Model for Rainfall Attenuation in South Africa", Paper presented at the *IEEE* Fifth International Conference on Wireless Communications, Vehicular Technology, Information Theory and Aerospace & Electronic Systems, Hyderabad, India, December 13-16, 2015.

Mary N. Ahuna, Thomas J. Afullo and Akintunde A. Alonge, "30-Second and One-Minute Rainfall Rate Modelling and Conversion for Millimetric Wave Propagation in South Africa", *SAIEE African Research Journal*, Vol. 107, pp. 17-29, March 2016.

Signed …… Date: …….

Mary Nabangala

Dedication

This thesis is dedicated to my family.

For their limitless support, love and encouragement

Acknowledgements

Above all, my sincere appreciation goes the Almighty God for granting me the gift of life and good health for the completion of this work. Secondly, my profound gratitude and appreciation goes to my supervisors, Professor Thomas J. Afullo and Dr. Akintunde A. Alonge for their guidance, suggestions and criticisms during the undertaking of this research.

I would also like to thank all staff members in the School of Electrical, Electronics and Computer Engineering, University of KwaZulu-Natal, South Africa, for their contribution in the success of this research work. A big thank you to Dr. Peter Akuon for his constructive suggestions, Mr. Khaye Dlamini, the school administrator, for his great assistance.

To my postgraduate colleagues and friends, a big thank you – especially Mr. Abraham Nyete, Mr, Mike Asiyo and Steven Awino.

I will be forever grateful to my family for their moral support and boundless understanding that greatly assisted me escape the study-related stress during my study period.

Abstract

Currently, there have been large demand for end-user services that use large bandwidths, while requiring best throughputs; these requirements are often not realistic because of meagre allocation of radio resources. Consequently, for many networks, the traditional option of migrating to higher frequency bands in the microwave and millimeter wave spectrum (3-300 GHz) is often the immediate solution. However, this option suffers a huge drawback most especially at geographical locations which experience signal deterioration from larger levels of hydrometeors (presence of water in the atmosphere). More importantly, the influence of ubiquitous hydrometeors such as precipitation, is reputed to be a major constraint to communication links between base stations at microwave and millimeter bands. This often cripples many radio networks, as a result of incessant and spontaneous outages experienced during rainfall events. Therefore, there is need for radio system engineers to acquire sufficient information on effects of rain in a particular locality for planning and design of reliable communication links. In this work, the choice of approaching this problem tallies with the International Telecommunication Union (ITU) concept of rainfall rate point estimation but with emphasis on measurements at lower integration time of 30-seconds.

This dissertation considers local rainfall rate measurements from 10 locations across South Africa at 5-minute integration time as obtained from South African Weather Services. Using rainfall measurements at one-minute and 30-second data from the coastal city of Durban (29°52'S, 30°58'E), various rainfall rate conversion models are obtained for these selected locations by applying rainfall statistics at higher integration time. Power-law functions obtained over South Africa reveals that rainfall statistics at 30-second integration time provides more information compared with one-minute and 5-minute integration times. In addition, a comparison of these results with ITU-R estimations have shown a close agreement with rainfall rates at 99.99% availability at the investigated locations.

Furthermore, a comparison of rainfall Drop Size Distribution (DSD) at 30-second and one-minute integration time over Durban is undertaken to establish temporal variability in disdrometer measurements. These variations are compared using statistical DSD models of lognormal and modified gamma distributions with two parameter estimation techniques: Method of Moments (MM) and Method of Maximum Likelihood (ML). Datasets employed are subset rainfall measurements with seasonal cycles comprising of summer, autumn, winter and spring, and on lumped yearly basis. Finally, investigations of the effects of rainfall integration time on rainfall attenuation are compared over Durban using one-minute and 30-second data. For this purpose, Mie scattering theory is employed to calculate the power-law coefficients and the frequency dependency of rainfall measurements at 30-seconds integration time.

TABLE OF CONTENTS

List of figures

List of tables

List of acronyms

Acronym		Meaning
BET	-	Bethlehem
BLM	-	Bloemfontein
CTN	-	Cape Town
DBN	-	Durban
ELD	-	East London
IRN	-	Irin
MFK	-	Mafikeng
MSB	-	Mossel Bay
PLK	-	Polokwane
UPT	-	Upington
MM	-	Method of Moments
ML	-	Maximum likelihood
LG	-	Lognormal DSD model
GM	-	Modified gamma DSD model
ITU-R (H)	-	Horizontal polarization
ITU-R (V)	-	Vertical polarization
DSD	-	Drop-Size Distribution
ECS	-	Extinction Cross Section
ITU-R	-	International Telecommunications Union-Radio communication sector
CHI	-	Chi Square Error technique
SAWS	-	South African Weather Services

List of symbols

Symbol		Meaning
R_τ	-	Rain rate at required integration time
R_T	-	Rain rate at available integration time
R_1	-	Rain rate at one-minute integration time
R_{30s}	-	Rain rate at 30-second integration time
R_5	-	Rain rate at 5-minute integration time
$R_{0.01}$	-	Rain rate exceeded at 0.01% of an average year
R_Y	-	Rain rate at location Y
H_{60s}	-	Specific attenuation resulting from horizontally polarized waves at 60-sec integration time
H_{30s}	-	Specific attenuation resulting from horizontally polarized waves at 30-sec integration time
V_{60s}	-	Specific attenuation resulting from vertically polarized waves at 60-sec integration time
V_{30s}	-	Specific attenuation resulting from vertically polarized waves at 30-sec integration time
k_H and α_H	-	Frequency dependent coefficients for horizontal polarization
k_V and α_V	-	Frequency dependent coefficients for vertical polarization
N_T	-	Drop concentration parameter for lognormal DSD
N_m	-	Drop concentration parameter for gamma DSD
a_T, b_T	-	Regression coefficients for lognormal drop concentration parameter
μ_{MM}	-	Lognormal mean parameter for method of moments parameter estimation
μ_{ML}	-	Lognormal mean parameter for method of maximum likelihood parameter estimation
σ_{MM}	-	Lognormal standard deviation parameter for method of moments parameter estimation
σ_{ML}	-	Lognormal standard deviation parameter for maximum likelihood parameter estimation
a_μ, a_σ, b_μ, b_σ	-	Regression coefficients for lognormal mean and standard deviation parameters
C_i	-	Number of rain drops in the *i*th channel
$C_{i,30s}$	-	Number of drops in the *i*th channel at 30-second integration time
$C_{i,60s}$	-	Number of drops in the *i*th channel at 60-second integration time

a_{ci} and b_{ci}	-	Regression coefficients for channel drop conversions
Q_{ext}	-	Cross section extinction
a_{ext} and b_{ext}	-	Frequency and temperature dependent cross section extinction coefficients
A_S	-	Specific attenuation
$\alpha_{GM\text{-}30}$	-	Coefficient α for gamma DSD model at 30-sec integration time
$\alpha_{GM\text{-}60}$	-	Coefficient α for gamma DSD model at 60-sec integration time
α_{30s}	-	Model α coefficient at 30-sec integration time
α_{60}		Model α coefficient at 60-sec integration time
k_{30s}	-	Model k coefficient at 30-sec integration time
k_{60s}		Model k coefficient at 60-sec integration time

CHAPTER 1

General introduction

1.1 Introduction

It is estimated, currently, that the wireless industry stands as a 1 trillion USD global business [*Rappaport et al.,* 2015]. This has been instigated by the need for higher bandwidths and data rates demanded by emerging technologies such as fourth-generation (4G) Long Term Evolution (LTE) cellular technology and IEEE 802.11n wireless internet standards, online broadcast companies, local multipoint distribution systems (LMDS) [*Ajayi and Ofoche,* 1984; *Islam et al.,* 2009; *Rappaport et al.,* 2015]. This need has driven wireless communication service providers towards operating in the microwave and millimeter wave bands. Some major benefits of wireless communication include deployment in mission-critical industrial applications and life-or-death military applications. Additionally, wireless technology is also easy to install and is relatively maintenance-free. If correctly engineered and installed, wireless systems can last maintenance-free for several tens of years because the absence of physical cables in the wireless medium increases the life-time of wireless links, provided that the transmitter and receiver are maintained properly. However, rain-induced attenuation is of great concern to wireless microwave communication systems engineers especially at frequencies above 10 GHz as a source of link outages [*Ajayi and Ofoche,* 1984; *Emiliani et al.,* 2009].

In addition to rain-induced attenuation, other notable microwave link outage factors include equipment failure and sub-standard link design objectives contributed by designers [*Ojo et al.,* 2009]. Therefore, ITU-R [*ITU-R F.1703-0,* 2005] provides a set of acceptable link performance for terrestrial microwave communication networks in the form of quality and availability objectives link lengths between 50 km and 2500 km. For access level part of the network, the recommended availability objective is 99.95% in both directions. For national and international levels, objective availability proposed are between 99.986% and 99.7% for 50 km and 2500 km links respectively [*ITU-R F.1703-0,* 2005]. For most terrestrial and satellite links, at least an objective availability of 99.99% is often desired [*ITU-R P.837-6,* 2012*; Moupfouma,* 1987], for adequate provision of link reliability. For successful design of satellite and terrestrial microwave systems, design engineers require sufficient information on rain attenuation for the region in consideration. This information can be estimated via analysis of rain rate data collected over a particular location for a relatively long period of time [*Ajayi and Ofoche,* 1984*; Emiliani et al.,* 2009*; Islam et al,* 2009*; Malinga et al.,* 2009]. There is a general agreement that for effective prediction of rainfall effects over radio links at microwave and millimeter wave bands, rainfall data measurements should be obtained from equipment with lower sampling times. Consequently, for effective prediction of rainfall effects over radio links at microwave and millimeter bands, measured data with integration

times at one-minute and or lower, are important [*Misme and Fimbel,* 1975*; Ajayi and Ofoche,* 1984]. These lower integration time data can be utilized to obtain rainfall distributions and useful conversion factors for effective radio planning. Also, research has shown that varying the integration time affects mainly the higher rainfall rates at smaller percentages of time [*Rodgers*, 1976; *Crane,* 1977; *Jones and Sims*, 1978; *Crane*, 1996]. These rainfall higher rainfall rates are of great importance because this is where the signal is highly affected by rain. Link designers use these rainfall rates in the design of reliable links, and hence the more accurate these values are determined, the more reliable shall the designed links become.

1.2 Problem formulation and motivation

Many network service providers lose their clientele due to link outages during rainy periods. The goal of wireless link designers is to plan and design communication links that are capable of providing reliable links for high throughput with as minimized link outages as possible. Commonly, a design performance of 99.99% system availability is desired for the satisfaction of end users. From previous work on rainfall study campaigns over South Africa, data with integration time of one minute and higher have been used. In this study, we explore the analysis of data with a lower integration time of 30 seconds in conjunction with higher integration time data and carry out a comparison between these two integration times. Additionally, this investigation is carried out to determine if rainfall data sampled at a lower integration time yields more information required by microwave system engineers for design and implementation of reliable microwave wireless links.

1.3 Objectives

The objectives of this study are geared towards:

1. Development of rainfall cumulative distributions and conversion factors over Durban for 1-minute and 30-second integration time rainfall data
2. Development of rainfall rate conversion models for 30-second and one-minute data in South Africa
3. Rainfall DSD modelling over Durban using one-minute and 30-second and 60-second integration times.
4. Correlation and comparison of DSD patterns over Durban for 30-second and one-minute integration time.
5. DSD conversions between 30-second and 60-second integration times

6. Comparison of specific attenuation predicted from 30-second and one-minute data based on seasonal and annual variations.

1.4 Dissertation overview

Chapter 1 highlights the motive behind wireless service providers migrating from longer wave bands to shorter wave bands in the millimeter and microwave regions. In this chapter, also a motivation for this study is presented. Additionally, objectives of the study and publications are also highlighted.

In Chapter 2, a literature review is presented on the impact of atmospheric effects on the millimeter and microwave signal as it propagates through the atmosphere. Additionally, microstructures of rain, rainfall rate prediction models, rain drop size distribution models and rainfall attenuation models and attenuation mitigation techniques are discussed in this chapter.

Rainfall rate models are developed for South Africa in Chapter 3 using data collected at three different integration times. These models are then validated and thereafter, specific attenuation values are determined at 30-second integration time and compared with specific attenuation at one-minute integration time.

In Chapter 4, rainfall Drop Size Distributions (DSDs) models are developed over Durban and a comparison is carried out for 30-second and one-minute integration times. Rainfall DSDs from measurements data are thereafter used to determine conversion factors for conversion from 60-second DSD to 30-second DSD. Modelled rainfall DSD were are then subjected to error analysis using the Root Mean Square Error (RMSE) technique.

Models developed in Chapter four, are used in Chapter five for estimation of rainfall specific attenuation at 30-second and one-minute integration times. Thereafter, error analysis is again performed on model estimates of specific attenuation over Durban.

Chapter 6 presents the conclusion and a recommendation on the future work for improvements.

1.5 Original contributions

- Development of rainfall rate conversion factors for 30-seconds over South Africa
- Comparison of specific attenuation values estimated from data measured using one-minute and 30-second sampling intervals.
- Development of DSD models using 30-second data over Durban

- Estimation of specific attenuation using developed rainfall DSD models and carrying out a comparison based on annual and seasonal variations for 30-second and one-minute integration times over Durban

1.6 Publications and journals

Mary N. Ahuna, Thomas J. Afullo, Akintunde A. Alonge, "30-Second Integration Time Power Law Conversion Model for Rainfall Attenuation in South Africa", Paper presented at the IEEE Fifth International Conference on Wireless Communications, Vehicular Technology, Information Theory and Aerospace & Electronic Systems, Hyderabad, India, December 13-16, 2015.

Mary N. Ahuna, Thomas J. Afullo and Akintunde A. Alonge, "30-Second and One-Minute Rainfall Rate Modelling and Conversion for Millimetric Wave Propagation in South Africa", *SAIEE African Research Journal*, Vol. 107, pp. 17-29, March 2016.

CHAPTER 2

Literature review

2.1 Introduction

The need for larger bandwidths is unavoidable in the delivery of communication service to the clientele by communications network service providers. However, the option of migrating to higher frequencies in Ka- and V-bands is hampered by link outages due to rain as a natural phenomenon that varies in space and time. In this chapter, the effect of the atmosphere on the electromagnetic wave is highlighted with more attention given to rain as the major contributor to the signal degradation. The extent to which rain affects a high frequency wave propagating through the atmosphere depends on its microstructural properties like the rain rate, rain drop size and rain drop density. These properties are also presented, alongside rainfall rate distribution and conversion models. Also, a literature review is carried out on rain drop size distribution models together with their parameter estimation techniques. And lastly, rainfall attenuation due to rain is presented mathematically together with methods of minimizing it along a microwave link for provision reliable communication in the microwave and millimeter wave bands.

2.2 Clear air signal propagation

A microwave signal propagating through the atmosphere, and especially the lower part of the atmosphere, suffers degradation from unpredictability nature of the atmospheric characteristics that change hourly, daily, monthly, or yearly [*Crane, 2003*]. Consequently, knowledge of statistics of one or more of effects of this layer on an electromagnetic signal becomes essential for microwave systems designers. Operating at millimetre and microwave wave bands results in an advantage of frequency re-use for short distance communications, however, these bands suffer from high signal degradation as the wave propagates through the atmosphere. Other notable propagation impairments that affect signal transmission over satellite and terrestrial networks include clear air atmospheric effects, sand, dust storms; fading due to obstruction, multipath, beam spreading and scintillation [*ITU-R P.618-11,* 2013].

The lower atmosphere is characterized as being absorptive, refractive and inhomogeneous. These characteristics impose great impact on an electromagnetic signal wave especially in the millimetre and microwave wave bands. Extreme refractive layers in the troposphere are the major source of electromagnetic wave signal fading. These effects include beam scattering, diffraction, diffusion and antenna decoupling [*Crane,* 1996; *Ippolito,* 2008; *ITU-R P.530-15,* 2013*; Asiyo and Afullo,* 2013]. When an obstacle is present on the propagation path of an electromagnetic wave, it causes the transmitted wave to arrive at its destination via two or more paths that may have been caused by multiple reflections and refractions. Concerning *diffusion*, reflecting materials tend to appear rougher at small wavelengths and

causes most of the signal to diffuse into the reflecting material instead of being reflected and as a result diminishes the signal received at the receiver. The direction of a signal propagating through the atmosphere is likely to be diverted as a result of inhomogeneity in the propagation medium. This effect is referred to as *scattering* [*Ippolito*, 2008].

In clear air conditions, an electromagnetic wave signal is subjected to scattering, diffraction and absorption. The main contributors to these factors being oxygen and water molecules, as shown in Figure 2.1. Thus, an electromagnetic propagated through clear air is also subject to loss of its energy as it propagates from the transmitting end to the receiving end.

The extent of the effect of the atmosphere on an electromagnetic wave is dependent on the frequency of transmission, atmospheric pressure, temperature and water vapour concentration. It is estimated that principal components of the atmosphere, by volume, are: nitrogen (78%), oxygen (21%), carbon dioxide (0.1%), argon (0.9%) and water vapour (variable). The current temperature of the atmosphere limits the water content level, resulting in very small levels in cold regions like the polar and upto 4% in the tropics. Once the water vapour contents rises above 4%, condensation starts and excess water vapour is released out of the air [*Ippolito,* 2008]. Among these components, oxygen and water vapour exhibit observable resonance at transmission bands up to 100 GHz. Signal attenuation by water vapour exhibits a quadratic function on its dependency on water vapour density at high densities above 12 gm^{-3} [*Karmakar et al*, 2010]. To evaluate propagation effects on a signal propagating through the atmosphere, [*Liebe,* 1989] proposed four main input parameters as frequency in GHz, total pressure in kPa, temperature in °C and relative humidity in percentage (%).

Figure 2.1 shows specific attenuation arising from gaseous absorption for a signal propagating through the atmosphere. From Figure 2.1, it observed that oxygen has absorption peaks at 60 GHz and 118.74 GHz. Similarly, for water vapour, the absorption effect also peaks at 22 GHz as well as at 183.3 GHz. Regions between absorption peaks are referred to as *transmission windows,* which become transparent to electromagnetic propagation. In Figure 2.1, transmission windows appear at 35 GHz, 94 GHz, 140 GHz and 220 GHz.

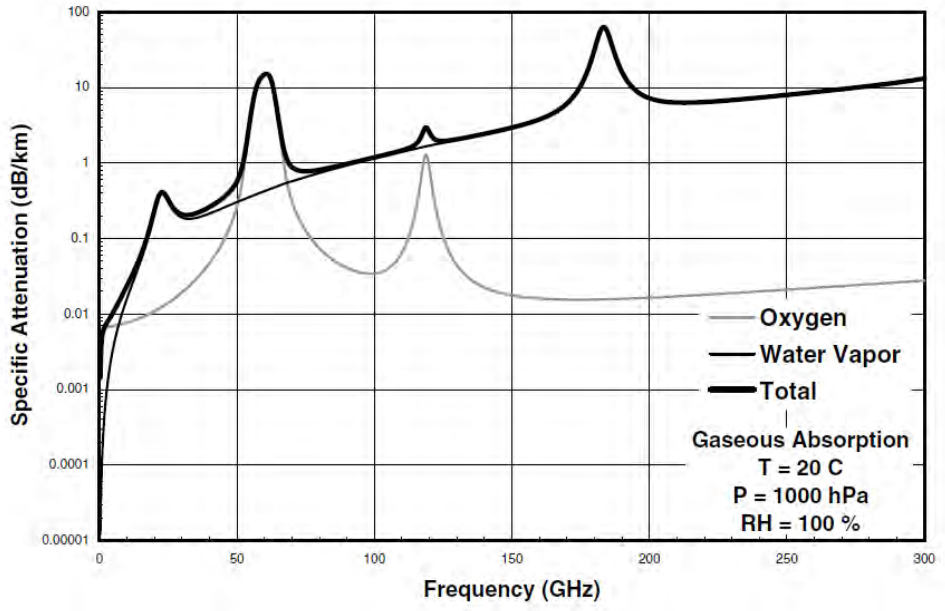

Fig. 2.1: Clear air specific attenuation as a function of [*Crane,* 2003].

In wireless communication, the free space equation that is frequently used relates the transmitted power, P_T and received power P_R is given by [*Crane,* 2003; *Elbert,* 2004; *Ippolito,* 2008]:

$$\frac{P_R}{P_T} = \left[\frac{G_T G_R \lambda^2}{(4\pi d)^2}\right] g_T(\theta, \Phi) g_R(\theta', \Phi') \tag{2.1}$$

where G_T and G_R are transmitter and receiver gains respectively, λ is the wavelength of the electromagnetic wave, d is the range or distance between two antennae, $g_T(\theta, \Phi)$ and $g_R(\theta, \Phi)$ are relative directive gains at spherical angles (θ, Φ).

From (2.1), the transmission loss can be re-arranged and written as:

$$P_R = P_T \left[\frac{G_T G_R \lambda^2}{(4\pi d)^2}\right] g_T(\theta, \Phi) g_R(\theta', \Phi') \quad \text{[Watts]} \tag{2.2}$$

Taking logarithms on both sides of the equation,

$$10\log_{10}(P_R) = 10\log_{10}\left[\frac{P_T G_T G_R \lambda^2 g_T g_R}{(4\pi d)^2}\right] g_T(\theta, \Phi) g_R(\theta', \Phi') \quad \text{[dB]} \tag{2.3}$$

$$P_R(\text{decibels}) = P_T + G_T + g_T + G_R + g_R + 20\log_{10}(\lambda) - 20\log_{10}(d) - 22 \quad (2.4)$$

where P_T, G_T, g_T, g_R are in decibels.

The power lost in the medium is the transmitted power, less the received power. This loss can thus be expressed as:

$$L = P_T - P_R = -(G_T + g_T + G_R + g_R + 20\log_{10}(\lambda) - 20\log_{10}(d) - 22) \quad [\text{decibels}] \quad (2.5)$$

where antenna gain *G* is in decibels relative to an isotropic antenna (dBi), the distance, *d*, and wavelength λ are in the same units.

2.3 Effects of hydrometeors on the signal propagation

Apparently, even on a bright day, humidity (or moisture) is present in the atmosphere [*Tamošiunaite et al.*, 2011]. In whichever form, hydrometeors have great impact on electromagnetic waves at frequencies above 10 GHz [*Crane, 2003; Ippolito,* 2008; *Tamošiunaite et al.,* 2011]. Most common hydrometeors include water vapour, fog, clouds and precipitation in the form of rain, snow and hail. In the presence of an electromagnetic wave, these hydrometeors become lossy dielectrics floating in air, with rain being the major cause of signal attenuation [*Crane*, 1996]. Clouds may not have great impact on electromagnetic wave, but it is true that they occur appear more frequently than rain. They are composed of suspended water droplets of less than 0.01 cm in diameter and the specific attenuation due to clouds can be estimated as [*Freeman*, 2007]:

$$\alpha_C = K_C M \qquad [\text{dB/km}] \quad (2.6)$$

where K_C, a function of frequency and temperature, is the attenuation constant and *M* is the liquid water content given in g/m^3.

Fog is regarded as condensed atmospheric water vapor that remains suspended in the air and can be a great concern to system link designers in the determination of reliable links more so, along coastal regions [*Freeman*, 2007; *Tamosiunaite*, 2011]. Normalized fog attenuation is expressed as [*Altshuler*, 1984]:

$$A = -1.347 + 0.0372\lambda + \frac{18}{\lambda} - 0.022T \qquad [(dB/km)/(g/m^3)] \qquad (2.7)$$

where λ is the wavelength in [mm] and valid for -8 < T< 25C and T is the temperature

In terms of water content, the empirical formula for estimating the fog attenuation is expressed as [*Altshuler*, 1984]:

$$V = 0.024M^{-0.65} \qquad [km] \qquad (2.8)$$

where *M* is the water content given in [g/m^3] and *V* is the fog visibility for drop diameters from 0.3μm and 10 μm.

2.4 Microstructural properties of rain

Rain can be described as a collection of water droplets falling back to the surface of the earth from the sky. The study of microstructural properties such as the rainfall rate, rain drop sizes, rain drop size distribution and the rain drop falling velocity gives a better understanding on the magnitude of the contribution of rain on the signal attenuation on a microwave link. The size of the rain drop and the rain drop size distribution (DSD) are very important parameters that affect the microwave in this band [*Kumar et al.*, 2002].

A rain drop in free fall can exist in different shapes from a sphere, a spheroid, oblate-spheroid or even a hamburger. Above 4 mm, the base of a drop acquires a concave shape [*Lie et al.,* 2000*; Goddard,* 2011]. Also, drops at different diameters fall with varying fall velocities as shown in Figure 2.2, clearly indicating that larger drops fall with higher velocities than small-sized drops.

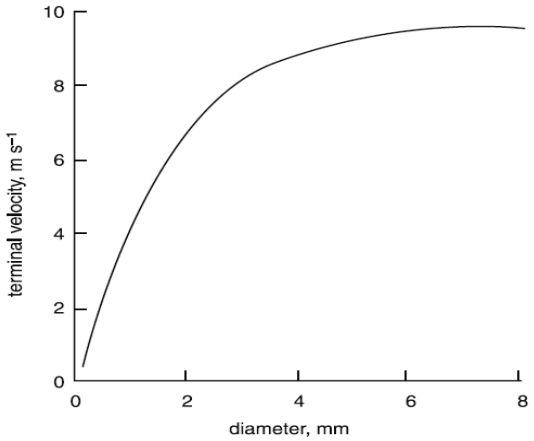

Figure 2.2 Terminal velocity of rain drops as a function of diameter [*Goddard,* 2011]

Rain can be classified into two classes as convective rain and stratiform rain [*Moupfouma,* 1987*; Kumar et al.,* 2011]. The latter type of rain is formed when warm air meets cooler air, forming nimbostratus clouds before falling back to ground as rain. The stratiform rain tends to be long-lasting, widespread and associated with low rainfall rates. On the other hand, convective rains results when hot and moist air rises, forming convective clouds (cumulonimbus) which then fall back to the ground as rain, over a certain area for a relatively shorter duration [*Crane*, 1996]. This type of rain is common in the tropics and is associated with high rainfall rates.

2.5 Rain rate measurement and cumulative distributions

For optimal wireless network service in a medium affected by rain, cumulative distributions represent an evaluation technique that can be used to identify the percentage of exceedence probability of rainfall rate. These probabilities enable communication systems design experts to define acceptable fade margin levels required by base stations in the reduction of network outages during rainy periods. Generally, a rainfall rate value corresponding to 0.01% exceedence (or 99.99% rainfall availability), is of major interest for sustainability of satellite and terrestrial communication links [*Moupfouma,* 1987; *ITU-R P.837-6,* 2012*;*]. This important rainfall rate is frequently referred to as $R_{0.01}$ and is measured in mm/h. Figure 2.4 shows an example of a cumulative distribution for various availability requirements against a parameter of performance.

2.5.1 Rainfall rate measurements

For decades, national meteorological administrations have been indispensable sources of rainfall measurements. These administrations archive measured rainfall data that is collected over relatively long periods of time. Alternatively, rainfall measurements can also be obtained by carrying out independent measurements using rain gauges, disdrometers and radars [*Moupfouma,* 1987; *Crane,* 1996*; Islam et al.,* 2009*; Akuon and Afullo,* 2011]. Amongst the three types of measuring instruments, the rain gauge is the most commonly used instrument because it is cost effective and can easily be installed [*Emiliani et al.,* 2009]. Different types of rain gauges exist including tipping bucket rain gauges, optical rain gauges, the standard (graduated cylinder) rain gauges, weighing precipitation gauges. Figure 2.3 shows three most common types of rainfall measurement instruments.

The tipping bucket rain gauge consists of a collector funnel that captures rainfall and directly the water into the tipping bucket device via a delivery pipe. The bucket is pivoted through its centre to allow the water to be emptied once the bucket is full. This action of emptying the bucket magnetically closes and opens a reed switch, and consequently, sends a pulse signal to the data logger. Most tipping bucket rain

gauges have calibration tips of 0.2 mm, 0.5 mm and 1 mm. The disdrometer, on the other hand, utilizes an electromechanical sensor in the form of a Styrofoam body and two moving coils that move downwards upon receiving an impact from the falling rain drop. This downward motion induces a voltage in the sensing coil, whose amplitude indicates the size of the rain drop that caused the impact [*Distromet System*, 2000; *Afullo*, 2011]. Lastly, an optical rain gauge uses an optical sensor to detect irregularities that are caused by particles falling through a beam of infrared light.

The tipping bucket rain gauge and the disdrometer instruments have varying levels of accuracy and measurement errors, with the disdrometer having an improved sensitivity to low rainfall rates (< 2 mm/h) than the rain gauge [*Wang*, 2006]. Another benefit of using a disdrometer in data measurement is its ability to measure rainfall drop size distribution, alongside rain rate measurements. This has greatly revolutionized raindrop size distribution studies all over the world. However, the rain gauge still is an inexpensive means of measuring data across the globe.

Rainfall rate, measured in mm/h, is the intensity of rainfall and is measured by calculating the amount of rain that falls on the surface of the earth per unit area per unit of time [*Tamošiunaite et al.,* 2011]. Green [*Green,* 2004] emphasised that rain attenuation is determined by the rate at which rain is currently falling and not just by the measure of how much it is falling. For the successful analysis of rainfall data, vital parameters including rainfall rate (R), total duration (T) of the propagation experiment, total time (t) of the experiment in which the rain rate R is exceeded and t as a percentage (P) of the total time, T must be provided, [*Moupfouma,* 1987]. A relationship existing between these four parameters are given in (2.9):

$$\mathrm{P}(\%) = \frac{\mathrm{t}}{\mathrm{T}} \times 100 \tag{2.9a}$$

where t is given as:

$$\mathrm{t} = \sum_{\mathrm{i}=1}^{\mathrm{N}} \delta_{\mathrm{ti}} \qquad [\mathrm{minutes}] \tag{2.9b}$$

$$\mathrm{R} = \frac{\mathrm{q}}{\mathrm{P}(\%)^{\mathrm{v}}} \qquad [\mathrm{mm/h}] \tag{2.9c}$$

where q and v are climatic zone dependent parameters.

Rainfall rate intensity, R, in mm/h, can also be sub-divided into regimes as drizzle rain ($R < 5$ mm/h), widespread rain (5 mm/h $\leq R <$10 mm/h), showers (10 mm/h $\leq R <$ 40 mm/h) and thunderstorms ($R \geq$ 40 mm/h) [*Ajayi and Adimula,* 1996; *Afullo,* 2011*; Alonge,* 2011]. In whichever form rain is, and it will always be a major cause of attenuation to an electromagnetic wave that comes in contact with its molecules; and the shorter the wavelength of the signal, the higher the signal attenuation. The magnitude of the effect of rain on an electromagnetic wave largely depends on a number of factors including the rain drop size, the fall velocity of the rain drop and the concentration of raindrops per unit volume, also referred to as the mean inter-drop distance

(a) (b) (c)

Figure 2.3 Rainfall rate measuring instruments (a) disdrometer (b) tipping bucket rain gauge (c) optical rain gauge

2.5.2 Rainfall rate cumulative distributions

Rainfall rate exceeded for 0.01% of an average year, equivalent to 99.99% system availability, is of great interest to system designers. This particular rainfall rate is commonly used in the estimation of rainfall attenuation over a microwave link for a performance of 99.99% link availability. ITU-R P.837-1 provides a table with cumulative distribution values for different climatic regions that do not have point rainfall rate measurements, as shown in Table 2.1. From *Ippolito* (2008), Figure 2.4 shows a general relationship between a parameter of interest, for instance, rainfall rate and the percentage of time a particular rainfall rate is equaled or exceeded. Another example is from *Ajayi and Ofoche* (1984), where fast response rain gauges with various integration times were used to generate rainfall rate cumulative distributions for at Ile-Ife, Nigeria. Graphs of these distributions, shown in Figure 2-5, confirm that lower integration times provide higher rainfall rates.

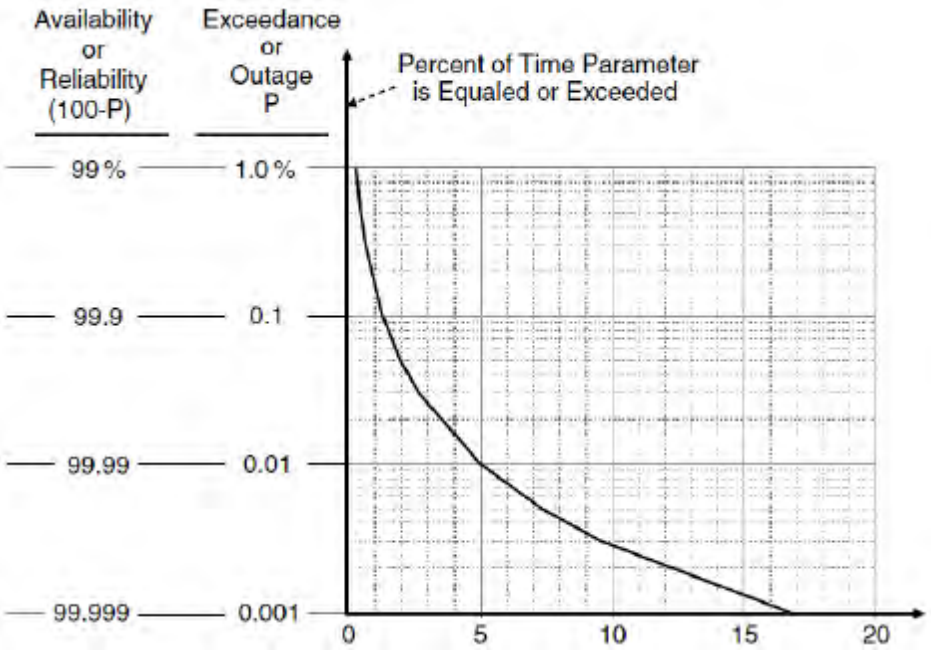

Figure 2.4: Percentage of time parameter is equaled or exceeded [*Ippolito,* 2008]

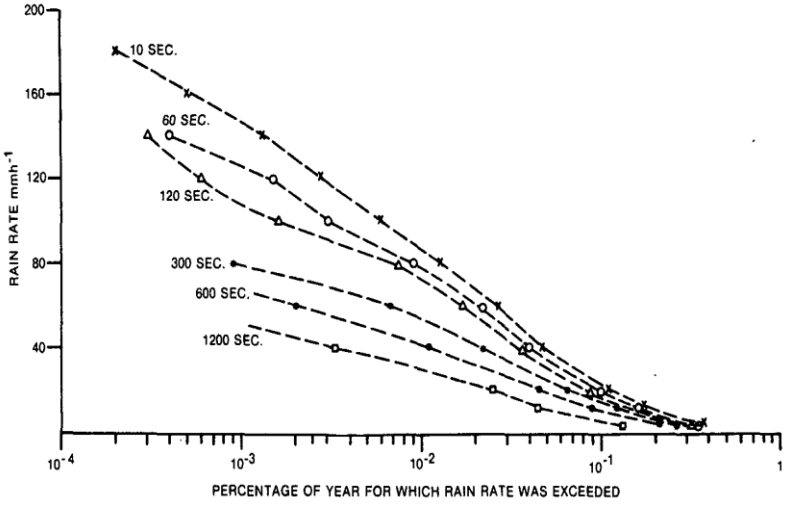

Figure 2.5: Cumulative distribution of rain at different integration times over Ile-Ife, Nigeria [*Ajayi and Ofoche,* 1984]

2.5.3 Rainfall rate conversion Models

There are two main approaches used for rainfall rate conversion - use of equivalent rainfall rates or application of the same probability of rainfall rate occurrence [*Ooi and Mandeep,* 2013]. Segal (1986), based on the first approach, proposed a method of conversion that was expressed as the proportion of the equally probable rainfall rate in the form:

$$R_\tau = aR_T{}^b \qquad [mm/h] \tag{2.10}$$

$$\rho_\tau(P) = \frac{R_1(P)}{R_\tau(P)} \qquad [mm/h] \tag{2.10}$$

where the conversion factor, $\rho_\tau(P)$ expressed as a power law as:

$$\rho_\tau(P) = aP^b \tag{2.11b}$$

where $R_1(P)$ represents the rainfall rate in a 1-minute integration time with the possibility of occurrence P, $R_\tau(P)$ is the rainfall rate in τ-min integration time and the parameters a and b are the regression coefficients that are derived from the computed rainfall data.

In a follow-up to Segal's method, *Chebil and Rahman* (1999) approached the matter by introducing additional variables of the exponential principle with the aim of increasing the flexibility of the method. The conversion of 60-minute to 1-minute rainfall distribution is expressed as:

$$\rho_{60}(P) = \frac{R_1(P)}{R_{60}(P)} \tag{2.12}$$

where $\rho_{60}(P)$ is expressed as a mixed Power-Exponential Law and is given by:

$$\rho_{60} = aP^b + ce^{(d)} \tag{2.13}$$

Where P is the percentage of time, $R_1(P)$ and $R_{60}(P)$ are the precipitation rate in 1-minute and 60-minute integration times to the percentage of time respectively, and *a, b, c* and *d* are the regression variables.

Ajayi and Ofoche (1984), making use of data collected at Ile-Ife between September 1979 and December, 1981, observed that most prediction methods require shorter rainfall rate statistics of at least 30 seconds to 5 minutes. For accurate prediction of rain attenuation in any given location, rainfall rate statistics of

less or equal to 1-minute integration time is preferred due to the rapidly changing nature of rainfall. From their work it was established that a power law relationship exists between the equiprobable rain rates of two integration times given in (2.14). *Ajayi and Ofoche* (1984) then established a relationship of 1 minute and 5 minutes integration times as:

$$R_1 = 0.991 R_5^{1.098} \qquad [\text{mm/h}] \tag{2.14}$$

where R_1 and R_5 are the 1-minute and equiprobable 5-minute rainfall rates respectively.

Results obtained by *Ajayi and Ofoche* (1984), shown in (2.14), were comparable with those of *Flavin* (1982), shown in (2.15), that had been examined at 6 minutes and 1 minute cumulative distributions for four locations in Europe, United States, Canada and Australia.

$$R_1 = 0.990 R_6^{1.054} \qquad [\text{mm/h}] \tag{2.15}$$

2.6 Rainfall Rate Distribution Models

Rain rate models are very useful for prediction of point rainfall-rate cumulative distributions for a location. There are a number of empirical models that have been developed by earlier researchers for the prediction of point rainfall-rate cumulative distribution [*Rice and Holmberg,* 1973; *Olsen,* 1999; *Dissanayake et al.,* 2002; *Ojo et al.,* 2008*; Chun and Mandeep,* 2013]. These models include Rice and Holmberg (1973) model, Moupfouma (1987) model, Moupfouma and Martins (1995) model, ITU-R P.837-6 (2012) model and Crane's models [1985; 1996*;* 2003].

In estimation of rain attenuation, *Olsen* (1999) emphasized the need for accurate rainfall rate predictions to avoid design of costly systems arising from over-prediction, or design of unreliable systems due to under-prediction. These models include the work of Crane [*Crane,* 1996] which greatly influenced the zonal models for ITU-R. Segal (1996) also developed a model that influenced the ITU-R zonal models by developing rainfall zones in countries like Canada. Watson *et al*. [*Watson et al,* 1982] also developed an approach that provides high quality estimates of rain intensity which was used to obtain rain rate values for use in fading calculations.

2.6.1 Rice-Holmberg (R-H) rain rate model

Rice and Holmberg (1973), using extensive long term statistics from over 150 locations throughout the world, developed the R-H model. This model constructs a rain rate distributions from the thunderstorm rain (mode 1) and "other rain" (mode 2). The total distribution is the sum of the two modes:

$$\mathrm{M} = \mathrm{Mode\ 1} + \mathrm{Mode\ 2} \quad [\mathrm{mm}] \tag{2.16}$$

The percentage of an average year for which the rain rate exceeds R mm/h at a medium location is given by [*Dissanayake et al.,* 1997; *Dissanayake et al.,* 2003],

$$\mathrm{P(R)\%} = \frac{\mathrm{M}}{87.6}\{0.03\beta \mathrm{e}^{-0.03\mathrm{R}} + 0.2(1-\beta)[\mathrm{e}^{-0.258\mathrm{R}} + 1.86\mathrm{e}^{-1.63\mathrm{R}}]\} \tag{2.17}$$

where M is the average annual accumulation of rainfall [mm], β is the thunderstorm component of M and R is the clock minute rain rate in mm/h.

The value of β and M can be read from the provided world maps as provided in *Rice and Holmberg* (1973), or can be calculated as [*Rice and Holmberg*, 1973; *Dissanayake et al.,* 2002],

$$\beta = \frac{\mathrm{M_1}}{\mathrm{M}} \tag{2.18a}$$

where M_1 is the average annual accumulation of thunderstorm rain [mm].

Also, beta can be determined as:

$$\beta = \beta_0[0.25 + 2\mathrm{e}^{-0.35}(1 + 0.125\mathrm{M})/\mathrm{U}] \tag{2.18b}$$

$$\beta_0 = 0.03 + 0.97\mathrm{e}^{-5\exp(-0.004\mathrm{M_m})} \tag{2.18c}$$

where U and M_m are the average number of thunderstorm days expected during an average year and the highest monthly precipitation observed in the total period of the experiment respectively.

The R-H model was later extended by *Dutton and Dougherty* (1974) to include an attenuation prediction property, which was deficient in the earlier R-H (1973) model. The modified model is given as:

$$P(R) = \begin{cases} 0.0114(T_{11} + T_{12})e^{-\frac{R}{R_1'}}, & R < 5 \text{ mm/h} \\ 0.0114T_{21}\exp\left(-\sqrt[4]{\frac{R}{R_{21}}}\right) & 5 \le R \le 30 \\ 0.0114T_{11}\exp(-R/\bar{R}_{11}) & R > 30 \end{cases} \quad (2.19)$$

where T_{11}, T_{21}, R'_1 and $\bar{R}$ are linear combinations of M, β and $D = 24 + 3M$, determined from regression equations.

The R-H model, when compared with measured data, suffers a drawback in underestimating rainfall rates at 0.01% and lower [*Crane,* 1996].

2.6.2 Crane rain rate models

In his contributions towards rainfall studies, Crane (1980) developed his first model that is popularly known as the Crane Global model. The second model, the 2-Component *Crane* (1982) model, used a path integrated technique in which a link calculation resulted from the sum of separately computed volume cell contribution and debris contribution. This is a closed-form probability distribution model that, separately, handles the contributions of volume cells and debris during the prediction of rain rate cumulative distribution functions (CDFs). This model was developed to determine the probability that a specified attenuation level is exceeded and this probability is the sum of probabilities associated with each component. The empirical rain rate distribution function is given by *Crane* (1996) as:

$$P(r \ge R) = P_C(r \ge R) + P_D(r \ge R) - P_{CD}(r \ge R) \quad (2.20a)$$

with

$$P_C(r \ge R) = P_C e^{-R/R_C} \quad (2.20b)$$

$$P_D(r \ge R) = P_N N\left(\frac{\ln R - \ln R_D}{S_D}\right) \quad (2.20c)$$

$$= \frac{P_N}{\sqrt{2\pi}S_D}\int_R^{\infty} \exp\left[\frac{1}{2}\left(\frac{\ln R/R_D}{S_D}\right)^2\right] \quad (2.20d)$$

$$P_{CD}(r \ge R) = P_C(r \ge R)P_D(r \ge R) \approx 0 \quad (2.20e)$$

where $P(r \geq R)$ is the probability that observed rain rate r exceeds specified rain rate R, $P_C(r \geq R)$, $P_D(r \geq R)$ and $P_{CD}(r \geq R)$ are the CDF's for volume cells, debris and joint CDF for volume cells and debris in that order, r and R are rain rates respectively, P_C & P_D are probability of cell and debris respectively, R_C and R_D are average rain rate in cell and median rain rate in debris respectively, N is the normal distribution function and S_D is the standard deviation of natural logarithm of rain rate.

The Revised 2-Component model was later introduced in 1989 and included, other features, spatial correlation and statistical variations of rain within a cell.

2.6.3 The Moupfouma I Model

This is a three-parameter model that bears a resemblance to an exponential distribution at higher rates and lognormal distribution at lower rain rates. It was developed by *Moupfouma* (1987). The model takes in rainfall rates as inputs and generates probabilities corresponding to those rainfall rates. The Moupfouma I model is expressed as:

$$P(r \geq R) = 10^{-4}\left(\frac{R_{0.01}}{r}\right)^{b} e^{\left(\lambda r^{1-s}\left[\left(\frac{R_{0.01}}{r}\right)-1\right]\right)} \tag{2.21a}$$

where r and R are rain rates in mm/h and,

$$b = 8.22(R_{0.01})^{-0.584} \tag{2.21b}$$

$$\mu = \lambda r^{-s} \tag{2.21c}$$

In the Moupfouma (1987), values of λ and s are given by ITU-R according to climatic zones *Moupfouma* (1987) as given in Table 2.1. One notable shortcoming of this model is the lack of probability distribution property.

Table 2.1 ITU-R parameters for Moupfouma models [*ITU-R P.837-1,* 1994]

Param.	**Climatic Zones**										
	D	**E**	**F**	**G**	**H**	**J**	**K**	**L**	**M**	**N**	**P**
λ	0.18	0.05	0.07	0.14	0.06	0.07	0.05	0.05	0.05	0.033	0.035
s	0.33	0.29	0.32	0.28	0.19	0.18	0.17	0.22	0.09	0.06	0.1

2.6.4 The Moupfouma and Martin Model

This is another empirical rainfall rate prediction model that was developed by Moupfouma and Martin (1995) to overcome the shortcomings of the Moupfouma I model. This model proved better for both tropical and temperate climates and can is expressed as:

$$P(R \geq r) = 10^{-4}\left(\frac{R_{0.01}}{r+1}\right)^{b} \exp[\mu(R_{0.01} - r)] \tag{2.22a}$$

where r, in mm/h, is the rainfall rate exceeded for a fraction of the time, $R_{0.01}$ is the rainfall rate exceeded for 0.01% of time and b is approximated by the expression:

$$b = \left(\frac{r - R_{0.01}}{R_{0.01}}\right)\ln\left(1 + \frac{r}{R_{0.01}}\right) \tag{2.22b}$$

and μ in equation (2.22a) is given by the expression:

$$\mu = \left(\frac{4\ln 10}{R_{0.01}}\right)\exp\left(-\lambda\left(\frac{r}{R_{0.01}}\right)\right) \tag{2.22c}$$

where $\lambda = 1.066$ and $\gamma = 0.214$

2.7 Rain Drop Size Distribution (DSD) Models

In the endeavor of estimating rain attenuation, a detailed knowledge of the rain drop size distribution (DSD) is a necessity. Rain drop size distributions depend on several factors including rainfall intensity, precipitation type, wind share, cloud type and circulation system [*Das et al.,* 2010]. Hence it is not a simple task to describe rain drop distribution by a universal, simple and precise model due to the spatial, temporal variability and complexity involved in the formation of rainfall [*Rodgers et al.,* 1976; *Medeiros et al.,* 1986; *Das et al.,* 2010]. Despite this difficulty, there is need to establish the rain drop size distribution at a given rain rate for calculation and modeling of rainfall attenuation. A number of DSD models exist such as the exponential DSD model, modified gamma model, lognormal DSD model, Erlang DSD model and Weibull DSD model. Parameters for these models are estimated using method of moments technique and the maximum likelihood method [*Das et al*., 2010; *Alonge*, 2011].

2.7.1 Lognormal Rainfall DSD Model

The Lognormal rainfall DSD is three-parameter distribution function that is described by the expression [*Feingold and Levin*, 1986; *Kozu and Nakamura,* 1991； *Timothy et al*., 2002]:

$$N(D_i) = \frac{N_T}{\sigma D_i \sqrt{2\pi}} \exp\left\{-\frac{1}{2}\left[\frac{\ln(D_i) - \mu}{\sigma}\right]^2\right\} \quad [m^{-3}mm^{-1}] \tag{2.23}$$

where N_T is the total number of rain drops, Di is the mean drop diameter in mm, μ and σ are the mean and standard deviation of drop sizes respectively.

Previous studies have shown that observed DSDs in tropical and sub-tropical regions tend to follow the lognormal distribution [*Das and Maitra,* 2000*; Alonge and Afullo,* 2011]. In their studies, *Moupfouma and Tiffon* (1982), *Ajayi and Olsen* (1985), *Massambani and Morales* (1988), M*assambani and Rodriguez* (1990) confirmed that the L-P and M-P models overestimated the number of rain drops in the small and large diameter regions. *Ajayi and Olsen* (1985), using a method of regression and data ranging from 0.25mm/h to 150 mm/h with data obtained at Ile-Ife, obtained a two-parameter lognormal model with parameters μ and σ with an additional parameter N_T for measurement fittings.

2.7.2 Modified Gamma Rainfall DSD Model

This is a three-parameter rainfall DSD model given by [*Atlas and Ulbrich,* 1974; *Ulbrich*, 1983; *Kozu and Nakamura* 1991]:

$$N(D_i) = N_m (D_i)^{\mu} \exp(-\Lambda D_i) \qquad [m^{-3}mm^{-1}] \tag{2.24}$$

Where $N(D_i)$ is the rain drop size distribution, N_m is the scaling parameter, μ is the shape parameter and Λ is the slope parameter and D_i is the mean rain drop diameter in the interval D to $D+\Delta D$.

According to Ulbrich (1983), this statistical DSD model responds well to rainfall DSDs at both low and high rainfall rates. It has been applied, in the past, in tropical and sub-tropical rain climates of Taiwan and Singapore [*Tseng et al,* 2005; *Lakshmi et al.,* 2011*; Kumar et al.,* 2010*],* South Africa *[Afullo,* 2011*; Alonge and Afullo,* 2011*; Owolawi, 2011; Alonge and Afullo,* 2012], India [*Das and Maitra, 2010*], Malaysia [*Yakubu et al., 2014; Lam et al., 2015*], Nigeria [*Ajayi and Olsen*, 1985;], USA [*Zheng et al., 2000*], among others.

2.8 Attenuation due to rain

With the assumptions that (1) the intensity of an electromagnetic wave decays exponentially as the wave passes through a rain cell, (2) raindrops are assumed to be spherical and (3) the contribution of each drop

are additive and independent of each other, an electromagnetic wave propagating through a rain cell with an extent, *d*, in the direction of propagation is expressed as [*Ippolito,* 1996*; Ippolito,* 2008]:

$$A_{dB} = \int_0^d A_S dx \tag{2.25}$$

where A_S is the specific attenuation of the rain cell and d is the extent of the propagation path from $x = 0$ to $x = d$.

Applying the assumption of an exponentially decaying wave as it propagates through a rain cell, the received power is given as [*Ippolito,* 2008]:

$$P_r = P_t e^{-kd} \tag{2.26}$$

where k is the attenuation coefficient for the rain cell, P_t and P_r are transmitted and received power, respectively.

A simple and straight forward way of expressing electromagnetic wave attenuation is [*Ippolito,* 2008]:

$$A_{dB} = 10\log_{10}\left(\frac{P_t}{P_r}\right) \tag{2.27}$$

Using (2.26) and (2.27), attenuation can then generally be expressed as:

$$A_{dB} = 4.343kd \qquad [dB] \tag{2.28a}$$

with

$$k = \rho Q_t \tag{2.28b}$$

and

$$Q_t(r, \lambda, m) = Q_s + Q_a \qquad [mm^2] \tag{2.28c}$$

where ρ is the drop density, Q_t is the attenuation cross section of the raindrop, Q_s and Q_a are scattering and absorption cross sections respectively.

Consequently, from (2.25) and (2.28), the specific attenuation can be computed as:

$$A_{dB} = 4.343 \int Q_t(r, \lambda, m)\eta(r)dr \qquad [dB/km] \tag{2.29}$$

Numerous experimental research works on specific attenuation have revealed that attenuation increases with increase in frequency and with decrease in elevation angle. As an example, from experimental study carried out *Ippolito* (2008) using five different elevation angles and a range of frequencies, graphs of Figure 2.6 supports this claim.

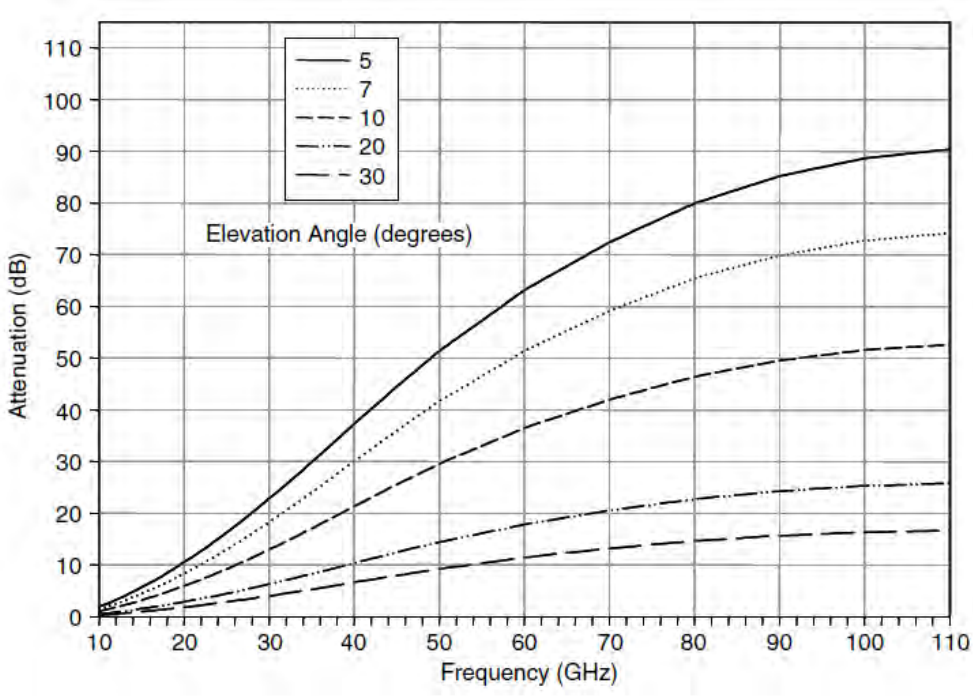

Figure 2.6 Total path rain attenuation as a function of elevation angle and frequency [*Ippolito,* 2008]

Also, research has established that a relationship that follows a power-law function exists between specific attenuation, A_S, and rainfall rate, R, in mm/h and is expressed as [*ITU-R P.838-3,* 2005; *Freeman*, 2007] as:

$$A_S = kR^{\alpha} \qquad [dB/km] \tag{2.31}$$

where k and α are frequency and temperature dependent regression coefficients.

When using (2.31), ITU-R P.838-5 (2005) provides the values of k and α as k_H and α_H for horizontal polarization and k_V and α_V for vertical polarization. These values are given in Appendix B. Additionally, Figure 2.7 shows the dependence of specific attenuation on frequency of operation.

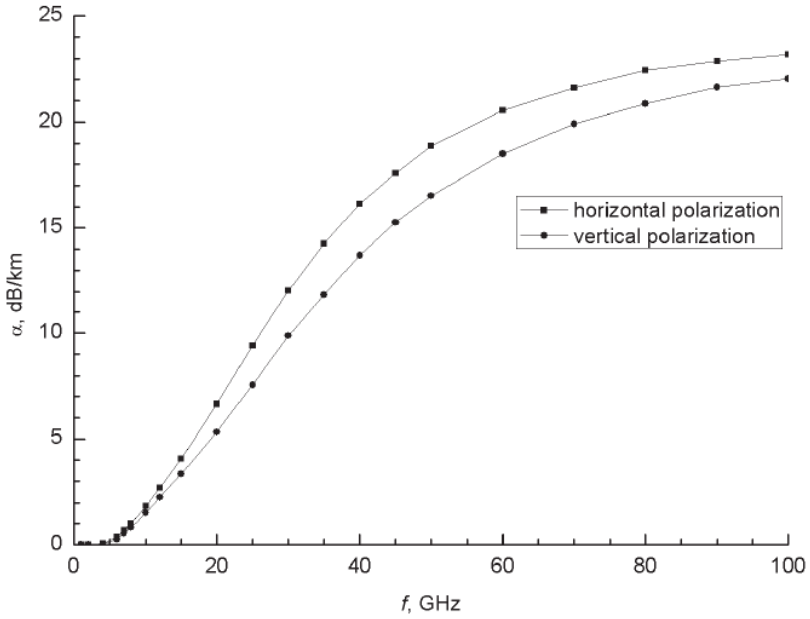

Figure 2.7 Dependency of specific attenuation due to rain on frequency [*Tamošiunaitė et al.,* 2011]

2.9 Rain Fade Mitigation Techniques

As millimeter and microwave bands are becoming indispensable in the wireless communication realm due to scramble for large bandwidths by wireless communication service providers, means and ways have to be found to cope with existing rain effects on the signal propagation in the millimeter wave band. This calls for employment of techniques to ensure that path attenuation does not exceed the available power margin. Two major classes of these techniques are *power restoral* and *signal modification restoral*. In power restoral class, techniques employed do not alter the basic format of the signal during the process of restoring the link. Some of the techniques employed here include beam diversity, site diversity, power control and use of low data rates. On the other hand, in the signal modification restoral class, techniques employed modify the basic characteristics of the signal. These techniques include time diversity, frequency diversity, bandwidth reduction, Adaptive Forward Error Correction and Adaptive Coded Modulation (ACM) [*Ippolito,* 2008*; Das et al.,* 2007*; Das et al.,* 2011]. A lot of research has been and is on-going for ACM technique [*Cioni et al.,* 2003*; Cioni et al,* 2004]. Some limitations may exist in the usage of some fade mitigation techniques. As an example, in the use of power control technique, extra power is transmitted when signal attenuation on the link is detected. However, this technique may not be technically nor economically viable at very high fade margins experienced at the much desired high frequency bands because this can result in wastage of power transmitted during non-rainy periods. Also in the usage of low data rates, as much as this reduces the bit error rate (BER) below

a certain desired threshold, a disadvantage of this technique is that there is usage of capacity even in the absence of the fade.

2.10 A review on Rainfall DSD studies in South Africa

Significant research work on rainfall DSD has been carried out associated with rainfall microstructural properties and microphysics for an accurate estimation of rainfall attenuation on microwave Line-of-sight (LOS) links over South Africa, and particularly, in Durban, for radio propagation in microwave and millimetre wave bands [*Owolawi et al.,* 2009; *Owolawi,* 2011*; Akuon and Afullo,* 2011; *Afullo,* 2011; *Alonge and Afullo,* 2012*; Odedina and Afullo,* 2012*; Malinga et al.,* 2013; *Alonge and Afullo,* 2014]. For instance, *Alonge and Afullo* (2014) carried out a comparison study on the microphysics of rain based on different regimes for two climatic locations, a tropical and a sub-tropical. In one of these studies, *Odedina and Afullo* [2008] proposed rainfall zones for attenuation prediction based on International Telecommunication Union (ITU) recommendation P.837-4 nomenclature [*ITU-R P.837-4, 2003*]. In their work, *Odedina and Afullo* (2012) also suggested that rain fading is severe in the north eastern provinces of South Africa compared to the western provinces. In a further experimental campaign on rainfall over South Africa, *Owolawi* (2011) was able to develop rainfall rate contour maps for South Africa's locations for 5-minute to 1-minute integration times. This study reinforced earlier investigations of *Odedina and Afullo* (2008). In addition, the rainfall drop size distribution (DSD) technique approach in [*Afullo, 2011*] enhanced initial efforts on rain rate campaign over Durban. *Alonge and Afullo* (2012) applied parameter estimation techniques to confirm that the lognormal and gamma DSDs gave the best characteristics of drop sizes over Durban. They further used this approach to establish the seasonal variability of DSDs in Durban. Their results predicted that summer and autumn seasons are periods associated with high probabilities of outages in wireless networks.

South Africa is a subtropical country whose climate is large moderated by two water body masses, the Indian Ocean in the east and the Atlantic Ocean in the west. From the influence of these two oceans, the eastern coast is relatively warmer than the western coast as a result of warm eastern Agulhas and Cold Benguela currents respectively. Figure 2.8 shows locations 9 provinces of South Africa as of the writing of this work.

,

Figure 2.8 Map of South Africa showing locations of study [www.places.co.za]

2.11 Chapter Summary

In this chapter, an overview is presented on the propagation of an electromagnetic wave at millimeter wave band and its interaction with atmospheric factors and rain. Consequently, rain, as the major contributor to the quality of the signal received, is examined in detail, based on its types, measurement intervals, drop size and drop shapes. Consequently, rain fade mitigation techniques have also been discussed. A review is also carried out on various existing rainfall rate models, rainfall drop size distribution models and rainfall attenuation models are discussed. These models, based empirical, analytical and statistical functions, form a good basis for rainfall attenuation estimation.

In the next chapter, rainfall rate modelling over South Africa using the power-law rain rate function is carried out. Thereafter, results of developed models are examined and validated using existing models developed over other regions of the world.

CHAPTER 3

Rain Rate Conversion Factors

3.1 Introduction

In the successful prediction of rainfall attenuation over a microwave link, system design engineers require accurate rain rate data to achieve a given link availability objective. There has been an immense agreement by researchers that for proper rainfall attenuation prediction, rainfall data measurements should be collected at an integration time of 60-second or lower [*Ajayi and Ofoche,* 1984; *Crane,* 1996*; Fashuyi et al.,* 2006; *ITU-R P.837-5,* 2007]. However, it is observed that most data available in meteorological departments are of hourly, daily or even monthly integration time. These longer resolution time data may be adequate for providing enough information for a large-scale farmer or a forester, but unfortunately, for a telecommunication systems engineer, the information provided may be inadequate for accurate prediction of rainfall attenuation along a satellite or terrestrial communications link [*Ajayi et al.*, 1996]. In Chapter two, rainfall rates and integration times were discussed in detail. In this chapter, these two rainfall microstructure and power-law function models are extended in the development of rainfall rate conversion models that will provide more accurate rain rate data at lower integration times.

Locations under study, were drawn from 8 out of 9 provinces of South Africa. The 9 provinces, are: Western Cape, Northern Cape, North West, Free State, Eastern Cape, KwaZulu Natal and Limpopo. These 7 provinces together with their locations are Western Cape (Cape Town, Mossel Bay), Northern Cape (Upington), North West (Mafikeng), Free State (Bloemfontein, Bethlehem), Easter Cape (East London), KwaZulu Natal (Durban) and finally, Limpopo (Polokwane). These locations exhibit different climates as shown by the map of Figure 3.6 according to Koppen-Geiger climate classification.

3.2 Data Measurements and Processing

Rainfall rate data measurements in this study were obtained from the Joss-Waldvögel (JW) RD-80 disdrometer installed at the roof top of the building, University of KwaZulu-Natal, Howard College. The disdrometer unit consists of two main components referred to as the outdoor unit and indoor unit. The setup for this equipment is shown in Figure 3.1., comprising of the outdoor unit (sensor) with a droplet receiving area of 0.005 m^2, the processor and the power supply. Apart from the outdoor unit, the other two units are indoor units that are housed in the weather monitoring room. More information in the operation of this type of the disdrometer is given by *Distromet System* (2000). This measurement instrument is capable of processing rainfall data into 20 channels via the indoor unit, [*Distromet System*, 2000] with each of the channels related to rain drops with diameter, D_i, in the range $0.3\ mm \leq D_i \leq$

5.4 *mm* (*See* Table C-1 in Appendix C). The accuracy of this measurement instrument is ±5%. From this instrument, the rainfall rate, *R,* is related to the mean drop diameter, D_i, by [*Ajayi et al.,* 1996; *Distromet System*, 2000; *Bartholomew,* 2009*; Lakshmi and Lee,* 2011; *Alonge and Afullo*, 2012]:

$$R = \frac{6\pi \times 10^{-4}}{A \times T} \sum_{i=1}^{20} D_i{}^3 C_i \quad [mm/h] \tag{3.1}$$

where C_i is the number of rain drops in the *i*th class; *T* is the sampling time given as 60 seconds; and *A* is the sampling area given as 0.005 m^2.

Disdrometer data measurements were collected at integration times of 30 seconds and 60 seconds. The 30-second data set and the 60-second dataset were collected over periods of 24 months and 27 months respectively, over Durban (29°52'S, 30°58'E) using the same disdrometer calibrated to different integration times. In addition to these two datasets, additional, 5-minute integration time dataset, collected over a period of 10 years, was obtained from the South African Weather Services (SAWS) for 10 locations in South Africa. A summary of these measurements is presented in Table 3.1.

Table 3.1 Rainfall rate data measurements

Integration Time	Duration (Months)	Instrument Used
30-second (Durban)	24	Disdrometer
1 minute (Durban)	27	Disdrometer
5 minute (10 locations)	132	Rain Gauge

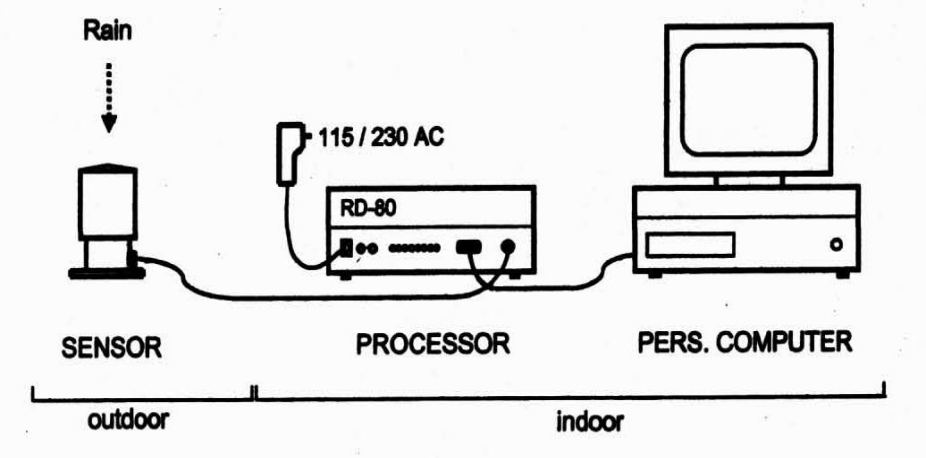

Figure 3.1 Disdrometer type RD-80 set up

3.3 Rainfall rate cumulative distributions and modelling over Durban

As was discussed in Section 2.5.2, cumulative distributions become useful to systems design engineers in the design of microwave links. In this section, measurement data obtained at three integration times are used to generate cumulative distributions over Durban shown in Figure 3.2. These cumulative distributions show rainfall rates exceeded with probability, P, where $0.004\% < P < 9.5\%$. Similarly, in Table 3.2, a summary of rain rate values at different integration times for percentages of rainfall rates exceeded between 0.01% and 1% are presented. Observations from Figure 3.2 show that the 30-second cumulative distribution is above the one-minute distribution with a margin of 4.8 mm/h at 99.99% system

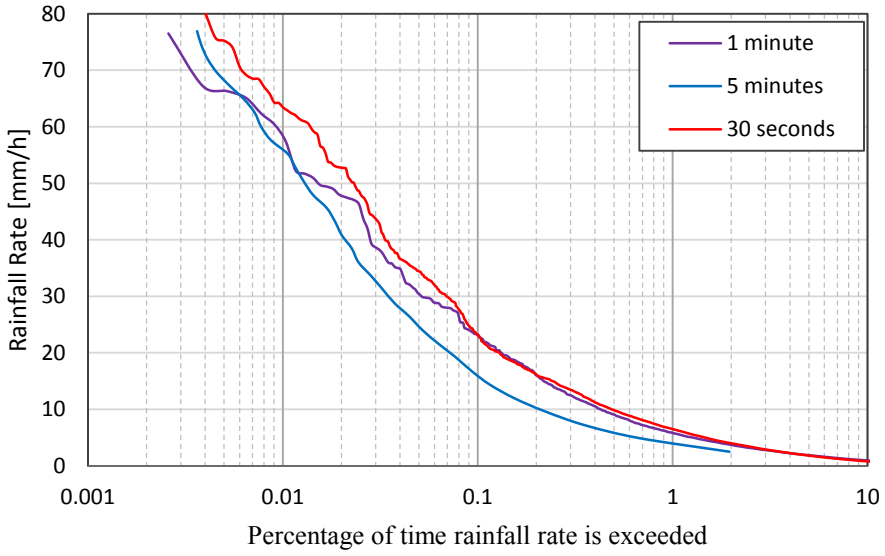

Figure 3.2 Cumulative distributions from measured rainfall rates for different integration times over Durban

Table 3.2 Measured Rain Rate exceeded for various integration times over Durban

Integration Time(Sec)	Rainfall Rate Exceeded				
	R_1	$R_{0.3}$	$R_{0.1}$	$R_{0.03}$	$R_{0.01}$
30	6.5	13.6	24.7	43.9	64.3
60	5.8	12.5	23.2	38.3	59.5
300	3.0	8.5	16.8	32.0	55.2

availability requirement. Application of (3.13) and ITU-R parameters in Table 3.13, this corresponds to

a specific attenuation margin of 1.2 dB/km at a frequency of 60 GHz using horizontal polarization. This is a vital source of information because this part of the graph is the high system availability region that suffers greatly from rainfall attenuation. This further confirms that 30-second integration time data provides more information required for estimation of rainfall attenuation compared to one-minute data.

It is thus manifested in Figure 3.2 that the rainfall rate increases as the integration time decreases. This also confirms that a rainfall rate measuring instrument with a long integration time will not capture shorter peaks present in the high rain intensity, resulting to lower measured rainfall intensities per unit length of time.

From Table 3.2, it is observed that R_1 value for 30-second integration time is 6.5 mm/h, $R_{0.1}$ is 24.7 mm/h and $R_{0.01}$ is 64.3 mm/h. For one-minute integration time, corresponding values are 5.8 mm/h, 23.2 mm/h and 59.5 mm/h at 1%, 0.1% and 0.01% probability of rainfall rate exceeded, respectively. For 5-minute integration time, rainfall rates are 3 mm/h, 16.8 mm/h and 55.2 mm/h at the same probabilities of exceedence.

From these results, it is observed that $R_{0.01}$ determined over Durban at one-minute integration time is 59.5 mm/h. This value is comparable to the predicted value of 63 mm/h in ITU-R [*ITU-R P.837-1,* 1994] for this region (region M) and it also supports the findings of *Akuon and Afullo* (2011) and [*Alonge,* 2011].

Rainfall rate conversion models exist for conversion from higher integration time rainfall rates, $R_{(T\ min)}$, to one-minute integration time rainfall rates, $R_{(1\ min)}$ [*Moupfouma,* 1987*; Owolawi,* 2011*; Crane,* 1996*; Matricciani,* 2011] (See Section 2.5). Among existing models, Matricciani (2011) proposed a more mathematical approach that aims at resolving errors present in the *T*-min probability distribution (PD). These errors include upward translation and clockwise or anti-clockwise rotation of the *T*-min PD at a fraction of time, *P*%, where $P > 1$. In this study, we choose to use the power-law relationship method due to its simplicity and ability to provide useful information in modelling. This conversion is beneficial in the development of rain rate models that can be applied in the prediction of rainfall attenuation for a given region, [*Islam, 2009; ITU-R P.618-11,* 2013].

There are two main approaches used for rain rate conversion - use of equivalent rainfall rates or application of the same probability of rainfall rate occurrence [*Ooi and Mandeep,* 2013]. The method adopted in this dissertation is the equal probability method. Using 5-minute, one-minute and 30-second data collected over Durban, conversion factors for conversion from higher to lower integration times were generated using the power-law fit and are shown in Figures 3.3, 3.4 (a) and 3.4(b). Subsequently,

these conversion factors are compared to those obtained by other researchers in different parts of the world.

3.3.1 Determination of conversion factors for one-minute integration time

A power-law relationship relating rainfall rate at the required integration time, τ, and rainfall rate at available integration time, T, at equal probabilities of exceedence, exists for $\tau < T$ as [*Ajayi and Ofoche,* 1984*; ITU-R P.837-5,* 2007]:

$$R_\tau(P) = \mu[R_T(P)]^\lambda \qquad (3.2)$$

where μ and λ are regression coefficients, $R_\tau(P)$ and $R_T(P)$ are equiprobable rainfall rates at required and available integration times exceeded for a percentage P of the year respectively.

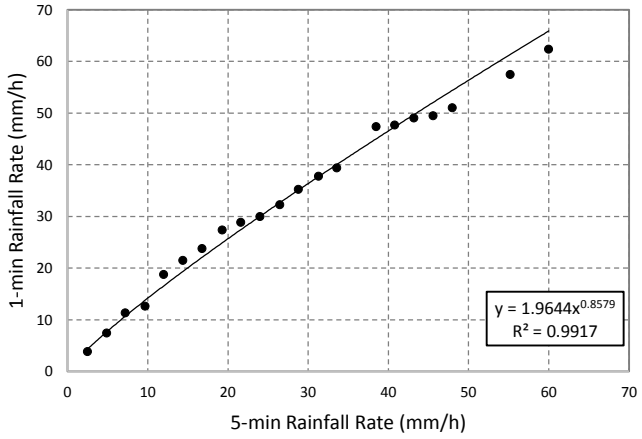

Figure 3.3 Conversion factors for one-minute integration time over Durban

Table 3.3 Validation of the proposed one-minute conversion model for Durban

Model	$R_\tau = \mu(R_T)^\lambda$ $[mm/h]$, for τ = 1 min				Error (%)
	T (min)	μ	λ	$R_{0.01}$	
Ajayi and Ofoche (1984)	5	0.991	1.098	81.0	36.1
Owolawi (2011)	5	1.062	1.051	71.9	20.8
Flavin (1982)	6	0.990	1.054	67.9	14.1
Proposed (Durban)	5	1.964	0.858	61.3	3.0

Using (3.2) and regression fitting shown in Figure 3.3, 60-second rainfall conversion coefficients are determined for the location of Durban are given as:

$$R_1 = 1.964\left(R_{5,DBN}\right)^{0.858} \quad [mm/h] \tag{3.3}$$

where R_1 and R_5 are one-minute and 5-minute integration times, respectively.

Application of the model in (3.3) for prediction of one-minute rainfall rates from 5-minute measured data over Durban is presented in Table 3.3. The predicted one-minute $R_{0.01}$ value is now 61.3 mm/h, which is above the 5-minute $R_{0.01}$ value of 55.2 by 6.1 mm/h rainfall rate intensity.

Results of Table 3.3 show the comparison of regression coefficients μ and λ obtained over Durban at one-minute integration time with those obtained by *Flavin* [1982] in Australia, USA, Europe and Canada and *Ajayi and Ofoche* (1984) over Ile-Ife in Nigeria.

From error analysis *Ajayi and Ofoche* (1984) model resulted in an error of 36.1%, the *Owolawi* (2011) model gave error of 20.8%, Flavin (1982) model gave 14.1% and the proposed model in (5) produced an error of 3.0%. The highest error is thus observed from *Ajayi and Ofoche* (1984) model. The tropical climate of Ile-Ife, characterized by heavy rainfall may be one factor contributing to this large error, bearing in mind that Durban is mainly subtropical. From Table 3.3, it is observed that the *Flavin* (1982) model is closer to the measurements in Durban with an error of 14.1%.

3.3.2 Determination of Conversion Factors for 30-second integration time

Rainfall rate conversion models from 5-minute and one-minute data to 30-second data were determined using regression fittings in Fig. 3.4 (a) and 3.4 (b):

$$R_{30s} = 2.078\left(R_{5,DBN}\right)^{0.868} \quad [mm/h] \tag{3.4}$$

$$R_{30s} = 1.051\left(R_{1,DBN}\right)^{1.004} \quad [mm/h] \tag{3.5}$$

where R_{30s} is the rainfall rate in mm/h at 30-second integration time, while, R_1 and R_5 are one-minute and 5-minute integration times rainfall rates, respectively.

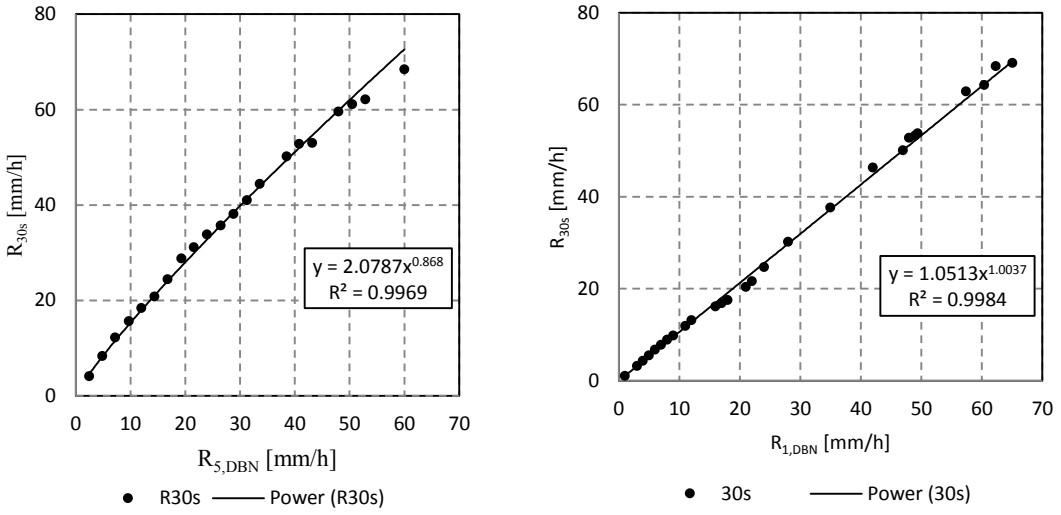

(a) (b)

Figure 3.4 Conversion factors for 30-second integration time from (a) 5-min to 30-sec and (b) 1-min to 30-sec integration times

Table 3.4: Predicted rainfall rates at 30-second integration time

Integration Time, (T sec)	$R_\tau = \mu(R_T)^\lambda$ [mm/h], for τ = 30s				
	R_1	$R_{0.3}$	$R_{0.1}$	$R_{0.03}$	$R_{0.01}$
60	6.1	13.3	24.7	40.8	63.6
300	5.4	13.3	24.1	42.1	67.6

It observed from Table 3.4 that predicted 30-second rainfall rates are higher than measured one-minute and 5-minute rainfall rates and especially at 99.99% system availability requirement. There is a margin of 4.1 mm/h rainfall rate between these two integration times. Likewise, predicted rainfall rate at 30-second from 5-minute data is 67.6 mm/h, up from a measured value of 55.2 mm/h at 5-minute integration time. Also, the predicted $R_{0.01}$ value of 63.6 mm/h is quite close to measured value of 59.5 mm/h.

3.3.3 Error Analysis for Durban Models

Estimates from our proposed rainfall rate conversion models should be representative of actual measurements. In this regard, our models in (3.3) - (3.5) were validated using Root Mean Square Error (RMSE) error analysis and the Chi squared statistics (χ^2) test for goodness of fit. Expressions for these two techniques are given in (3.6) and (3.7) [*Galoie et al., 2013*]:

$$\mathrm{RMSE} = \sqrt{\frac{1}{\mathrm{K}}\sum_{\mathrm{k=1}}^{\mathrm{K}}[\mathrm{O_k} - \mathrm{E_k}]^2} \tag{3.6}$$

$$\chi^2 = \sum_{\mathrm{k=1}}^{\mathrm{K}} \frac{(\mathrm{O_k} - \mathrm{E_k})^2}{\mathrm{O_k}} \tag{3.7}$$

where O_k and E_k are the measured and predicted rainfall rates respectively, with K being the sample size.

In Table 3.5, we present a summary of results obtained from error analysis in (3.6) and (3.7) for power-law models describing our conversion models.

Table 3.5 Conversion factors for one-minute and 30-second integration times for Durban

T (Sec)	$R_\tau = \mu(R_T)^\lambda$ $[mm/h]$, for τ = 60s			Error analysis	
	μ	λ	R^2	RMSE	CHI
300	1.964	0.858	0.992	1.883	2.037[a]
	$R_\tau = \mu(R_T)^\lambda$ $[mm/h]$, for τ = 30s				
300	2.078	0.868	0.997	1.324	0.845[b]
60	1.051	1.004	0.998	1.051	1.019[c]

Significant level is given as [a]32.671, at DF = 21, [b]32.671 at DF = 21, and [c]40.113 at DF = 27

The chi-squared test was carried out at a confidence level of 0.05 and gave values of 2.037, 0.845, and 1.0193, for the three models in (3.3) - (3.5), respectively. A comparison with the chi-squared table shows that proposed rainfall rate conversion models passed the test and can be used for future conversions in Durban.

3.3.4 Validation of Durban conversion Models

Durban's one-minute measured rainfall data were compared with selected global models including the Moupfouma and Martin (1995) model, the Rice-Holmberg (1973) model and ITU-R P.837-1(1994) model, as shown in Figure 3.5. This figure shows a comparison of measured and predicted rainfall intensities exceeded in a fraction of a year.

It is seen from Table 3.6 and Figure 3.4 that the predicted values by other models agree quite well with the measured values. These models predict a rainfall rate of around 60 mm/h at 0.01% exceedence, which is relatively close to proposed $R_{0.01}$ value of 63 mm/h for Durban in region M, [*ITU-R P.837-1, 1994*] (see, Table A-1 in Appendix A). It is also noted that the R-H (1973) model underestimates rain rates for probability $P < 0.01\%$ compared with measured values. Predicted values were compared with the Durban's measured $R_{0.01}$ of 59.5 mm/h and RMS errors show that R-H model is closest to the measured value with an error of 1.3% at $P = 0.01\%$.

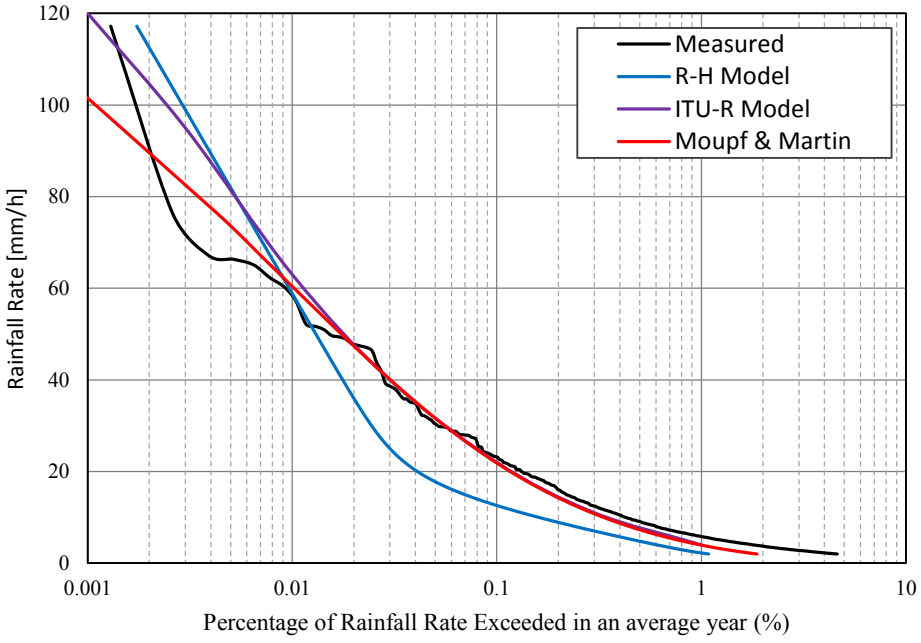

Figure 3.5 Validation of conversion models for Durban

Table 3.6. Validation of measured one-minute $R_{0.01}$ value over Durban

Model	Rainfall rates [mm/h]			RMS
	R_1	$R_{0.1}$	$R_{0.01}$	
Measured (Durban)	5.8	23.1	59.5	-
Moupfouma and Martin (1995)	3.9	22.0	59.5	-
Rice-Holmberg (1973)	2.3	12.6	60.3	1.3
ITU-R Model (*1994*)	4.0	22.0	63.0	5.9

3.4 Development of Rainfall conversion factors for other locations in South Africa

Due to scarcity of, especially one-minute and lower rainfall rates in other locations of South Africa, conversion models that were developed in (3-2) and (3-3) over Durban (29°52'S, 30°58'E) were used to convert 5-minute rainfall data available in other locations to their equivalent one-minute and 30-second data. Figure 1-1 and Figure 1-2 show selected geographical locations under study (see Fig. 3-5 and Table 3-7), representing eight out of nine provinces of South Africa, were categorized according to Köppen-Geiger classification as presented in Table 3.7. Based on earlier research by Köppen and Geiger, [*Rubel and Kottek,* 2010], the Council for Scientific and Industrial Research (CSIR) created a new Köppen-Geiger classification map for South Africa, [*Conradie,* 2012]. This classification is a 2- or 3-letter code that describes the climatic characteristics of a region by considering a combination of precipitation and temperatures. For instance, a climate described as **Cfa** is a warm temperate climate, fully humid with hot summers

Table 3.7 Geographical description of locations of study

LOCATION	Coordinates		Köppen-Geiger Classification [*Conradie*, 2012]	
	LONGT.	LAT.	Class	Description
Bethlehem (BET)	28.23ºS	28.30ºE	Cwb	Temperate, Warm summer
Bloemfontein (BLM)	29.12ºS	26.23ºS	Bsk	Cold Arid Steppe
Cape Town (CTN)	33.93ºS	18.42ºS	Csc	Temperate, Cool summer
Durban (DBN)	29.88ºS	31.05ºS	Cfa	Sub-tropical, fully humid
East London (ELD)	32.98ºS	27.87ºS	Cfa	Sub-tropical, fully humid
Irene (IRN)	25.87ºS	28.22ºS	Cwb	Temperate, Warm summer
Mafikeng (MFK)	25.85ºS	25.63ºS	BSh	Hot Arid Steppe
Mossel Bay (MSB)	34.18ºS	22.13ºS	Bsk	Cold Arid Steppe
Polokwane (PLK)	23.90ºS	29.45ºS	Bsk	Cold Arid Steppe
Upington (UPT)	28.40ºS	21.27ºS	BWh	Cold Arid

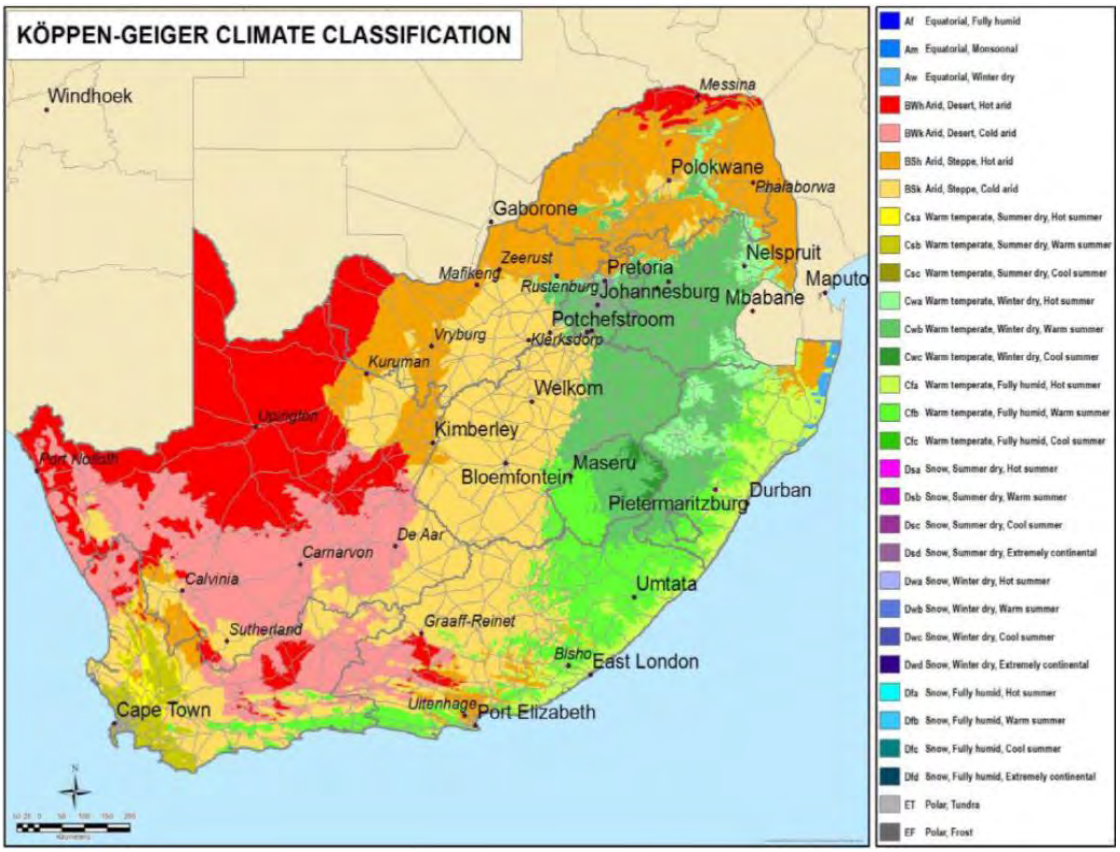

Figure 3.6 CSIR Koppen-Geiger map based on 1985-2005 SAWS data [*Conradie*, 2012]

with temperatures, $T_{max} \geq +22°C$. A **Csc** is a warm temperate climate with dry and cool summer, cold winter seasons and winter temperatures dropping to as low as -38°C. A **Cwb** climate is warm temperate with dry winter and warm summer seasons with average monthly temperatures of +10°C. The **Bs** code denotes steppe climates with **Bsh** signifying a hot steppe with annual temperatures $T_{ann} \geq +18°C$. The **BWh** is a hot steppe/desert climate with annual temperatures $T_{ann} \geq +18°C$. Classification of all locations under study are presented in Table 3.7.

3.4.1 Cumulative Distributions for 5-minute Data

Empirical rain rate distributions for different climatic locations within South Africa at 5-minute integration time are presented in Fig. 3.7. These distributions show probabilities of occurrences of rainfall rate distributions of specified intensities for each location. A summary of measured rainfall rates are summarized in Table 3.8.

As observed in Fig. 3.7 and Table 3.8, Durban recorded higher values of rainfall rates exceeded at 0.002% and below compared to other locations, followed by Mafikeng. In the lower end is Mossel Bay and Cape Town with low rainfall rates at the same probability of exceedence. Also, it is observed from Table 3.8 that there is no obvious correlation between mean annual rainfall and rainfall exceeded for a percentage of time. As an example, East London recorded the second highest annual mean rainfall of 830.7 mm, yet its $R_{0.01}$ rainfall rate was only 41 mm/h as compared with Polokwane's $R_{0.01}$ value of 51.0 mm/h with an annual mean rainfall of 426.0 mm/h. One explanation for this could be that Polokwane receives heavy rains of convective type within short periods as compared with East London that experiences lighter rains of stratiform type for relatively longer periods. Also, other topographical features, including hills, water masses and presence of mountains, may influence the rain climate of a region.

Observations from Table 3.8 also affirms Köppen-Geiger classification map for South Africa. For instance, it is observed that Cape Town, with a **Csc** climate, has a relatively low $R_{0.01}$ rainfall rate of 26.0 mm/h. Cool summers, in this location, experience low amounts of precipitation contributed by less evaporation due to low temperatures.

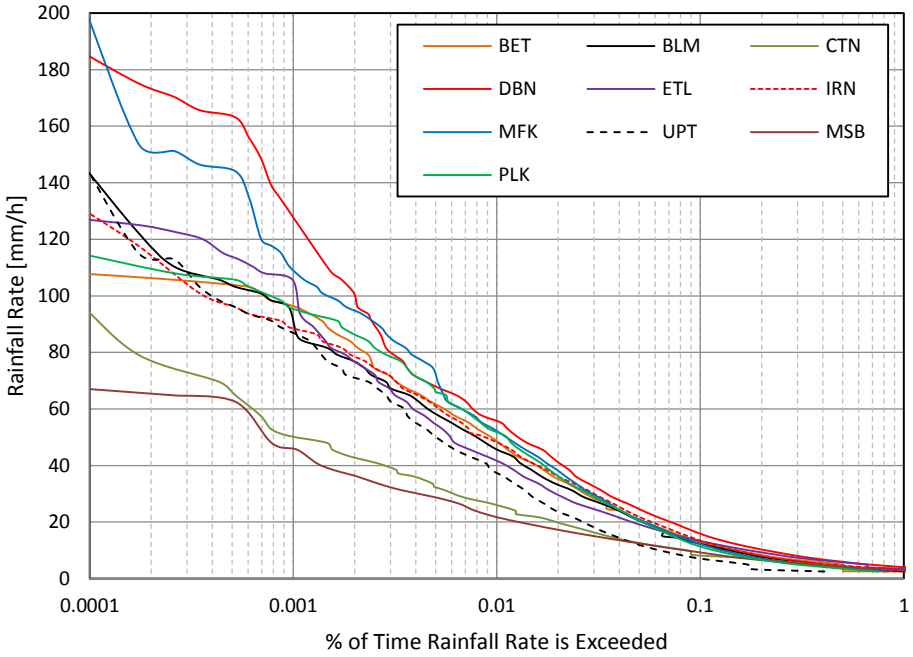

Figure 3.7: Cumulative distributions for 10 locations at 5-minute integration time

Table 3.8. Rainfall rate exceeded at 5-minute integration time for 10 locations

Location	**Rainfall rates [mm/h]**				**Rainfall Statistics**	
	R_1	**$R_{0.1}$**	**$R_{0.01}$**	**$R_{0.001}$**	***M* [mm]**	**Samples**
BET	2.5	12.0	48.0	96.0	624.0	15,833
BLM	2.5	12.0	45.6	96.0	507.7	11,648
CTN	3.0	8.0	26.0	50.5	464.0	15,407
DBN	4.0	16.0	55.2	130.0	889.0	23,241
ELD	3.5	13.0	41.0	105.0	830.7	23,938
IRN	2.8	12.0	48.0	88.0	581.5	23,938
MFK	2.3	12.0	52.9	110.4	470.0	14,139
MSB	2.7	9.7	21.6	45.6	403.6	4,346
PLK	2.6	12.0	51.0	96.0	426.0	8,610
UPT	2.1	7.2	36.0	86.4	229.2	4,714

Correspondingly, Durban, classified with a **Cfa** climate, recorded higher rainfall rates of 55.2 mm/h compared with other locations.

3.4.2 Rain rate conversion factors for other locations in South Africa

Available 5-minute data in 9 other locations in conjunction with the 5-minute, one-minute and 30-second data available in Durban (29°52'S, 30°58'E), led to development of conversion models for other locations. Following a confirmation drawn from Table 3.4 that lower integration time data provide more information on rainfall statistics of a location as compared with a higher integration time data, it was deemed necessary to generate conversion factors for other locations to obtain lower integration time data that can be useful in the design of reliable microwave links.

3.4.2.1 Rain rate conversion factors for one-minute conversion factors

Having obtained useful rain rate values from 5-minute cumulative distributions from selected locations, it is most important to convert these values to their lower integration time equivalents as undertaken in [*Owolawi,* 2011] and [*Akuon and Afullo,* 2011]. Akuon and Afullo (2011) proposed a mathematical technique of executing this by comparing and substituting the values from rain conversion power-law functions. Firstly, parameters for other locations were determined using the power-law function proposed by *[Watson et al.,* 1982*; ITU-R P.837-5,* 2007] as given in (3-1). Consequently, conversion factors for Durban were determined as:

$$R_{1,DBN} = \mu\left(R_{5,DBN}\right)^{\lambda} \tag{3.8}$$

where μ and λ are conversion factors obtained for Durban.

The 5-minute equiprobable rainfall rates at each of the 9 locations were used in the determination of regression factors, [*Akuon and Afullo,* 2011], using (3-8),

$$R_{5,Y} = \phi\left(R_{5,DBN}\right)^{\beta} \tag{3.9}$$

where $R_{5,Y}$ is 5-minute rainfall rate equivalent of Durban's 5-minute rainfall rate at region *Y,* whereas ϕ and β are regression factors for region *Y*.

Accordingly, from (3.7) and (3.8), conversion factors from 5-minute data to one-minute data for Location *Y* in South Africa, can be determined using (3.9),

$$R_{1,Y} = \mu\left(\phi\left(R_{5,DBN}\right)^{\beta}\right)^{\lambda} \cong m\left(R_{5,DBN}\right)^{n} \tag{3.10a}$$

$$R_{1,Y} = \mu\left(\phi\left(R_{5,DBN}\right)^{\beta}\right)^{\lambda} \cong m\left(R_{5,DBN}\right)^{n} \quad (3.10b)$$

where $R_{1,Y}$ is the derived one-minute equivalent rainfall rate for location *Y,* and μ, λ, ϕ, β, m and n, are regression coefficients with m and n given by:

$$m = \mu\phi^{\lambda} \quad (3.10c)$$

$$n = \beta\lambda \quad (3.10d)$$

with $\mu = 1.9644$, $\lambda = 0.858$ over Durban and values of ϕ and β as generated for each location and given in Table 3.9.

Table 3.9. Conversion factors for one-minute models for 10 locations

LOCATION	$R_{5,DBN} \rightarrow R_{5,Y}$		$R_{5,DBN} \rightarrow R_{1,Y}$	
	ϕ	β	m	n
BET	0.910	0.968	1.8117	0.8305
BLM	0.893	0.966	1.7826	0.8288
CTN	0.777	0.875	1.5820	0.7508
ELD	0.970	0.943	1.9137	0.8091
IRN	1.141	0.918	2.1998	0.7876
MFK	0.727	1.057	1.4943	0.9069
MSB	0.951	0.800	1.8815	0.6864
PLK	0.645	1.066	1.3484	0.9146
UPT	0.289	1.191	0.6771	1.0219

3.4.2.2 Rain rate conversion factors for one-minute conversion factors

Applying a similar concept, used in (3-7) – (3-9), a conversion model for conversion from 5-minute data to 30-second data is given as:

$$R_{30s,DBN} = \phi\left(R_{5,DBN}\right)^{\theta}, \quad (3.11)$$

and,

$$R_{30s,Y} = \varphi\left(\phi\left(R_{5,DBN}\right)^{\beta}\right)^{\theta} \equiv \; p\left(R_{5,DBN}\right)^{q} \quad (3.12a)$$

where $R_{30,Y}$ is the equivalent 30-seconds rainfall rates for location Y, and p and q are regression coefficients determined as:

$$p = \varphi\phi^{\theta} \tag{3.12b}$$

$$q = \beta\theta \tag{3.12c}$$

with $\varphi = 2.0780$, $\theta = 0.8680$ over Durban and values of ϕ and β as given in Table 3.9.

In Table 3.10, we present conversion factors for different climatic locations in South Africa as processed from 11-year, 5-minute integration time data. From this table, it may be deduced from these coefficients that Durban has higher rainfall rates than other locations under study at the same probability of exceedence.

Table 3.10. Conversion factors for 30-second model for 10 locations

LOCATION	$\boldsymbol{R_{30s} = p(R_{5,DBN})^{q}\ [mm/h]}$	
	$\boldsymbol{p}$	$\boldsymbol{q}$
DBN	2.0780	0.8680
BET	1.9147	0.8402
BLM	1.8836	0.8385
CTN	1.6693	0.7595
ELD	2.0238	0.8185
IRN	2.3301	0.7968
MFK	1.5756	0.9175
MSB	1.9893	0.6944
PLK	1.4202	0.9253
UPT	0.7075	1.0338

3.4.3 Rain rate distributions for predicted rainfall rates

Cumulative distributions over various locations in South Africa at one-minute and 30-second predicted data are presented in Fig. 3.8 (a) and 3.8 (b). Once again, observations show that predicted data at 30-second integration time are higher than at one-minute integration time, as expected.

Table 3.11 presents predicted rainfall rates at one-minute and 30-second integration times after application of conversion models in (3.9) and (3.11). Observations from this table reveals that rainfall rates at 30-second integration time are higher than those at one-minute integration time at same probability of exceedence. Generally, there is an average margin of 0.95 mm/h at 99% system availability between one-minute and 30-second rainfall rates when all 10 locations are considered. In the same way, margins are 2.04 mm/h and 4.66 mm/h at 99.9% and 99.99% system availability requirements, respectively. The higher margin at high system availability requirement buttresses the need for using rainfall rate measuring equipment with lower integration times during data collection.

Table 3.11. One-minute and 30-second predicted rainfall rates exceeded at various percentages

Loc.	$R_{1,Y} = m(R_{5,DBN})^n$ **[mm/h]**			$R_{30s,Y} = p(R_{5,DBN})^q$ **[mm/h]**		
	R_1	$R_{0.1}$	$R_{0.01}$	R_1	$R_{0.1}$	$R_{0.01}$
BET	4.5	17.0	50.7	6.3	19.5	55.7
BLM	4.5	16.3	49.5	6.0	19.2	54.4
CTN	3.2	11.7	32.1	4.8	13.6	35.1
DBN	5.8	20.3	61.3	6.8	23.0	67.6
ELD	5.5	17.7	49.1	6.3	19.5	53.9
IRN	5.7	19.2	51.8	7.1	20.1	56.9
MFK	5.6	16.8	56.8	5.8	19.9	62.5
MSB	4.2	11.7	29.5	5.2	13.6	32.2
PLK	5.2	17.8	52.9	5.2	18.4	58.1
UPT	2.8	10.3	40.8	3.0	12.4	44.7

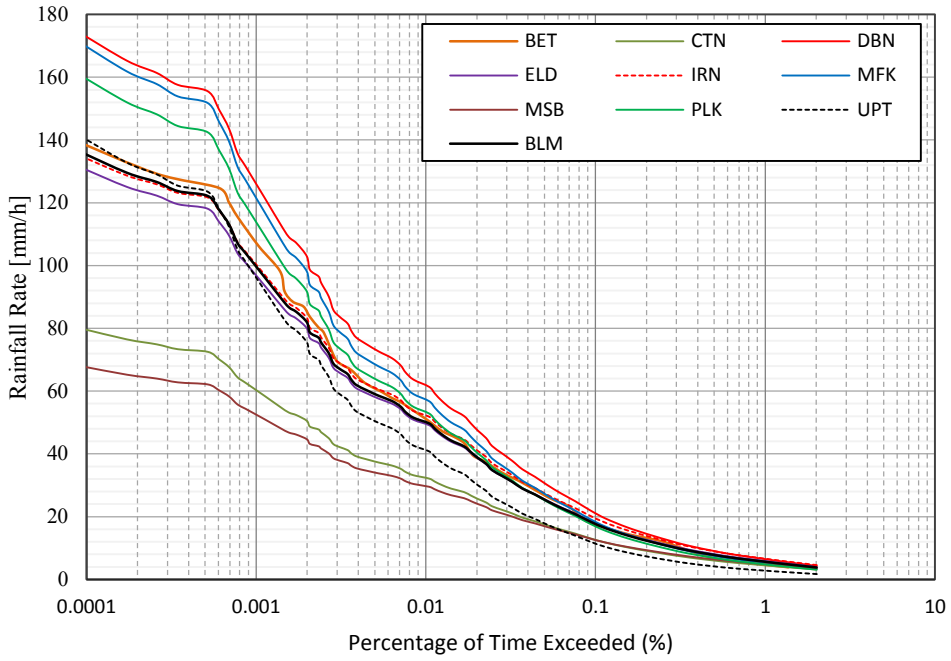

(a)

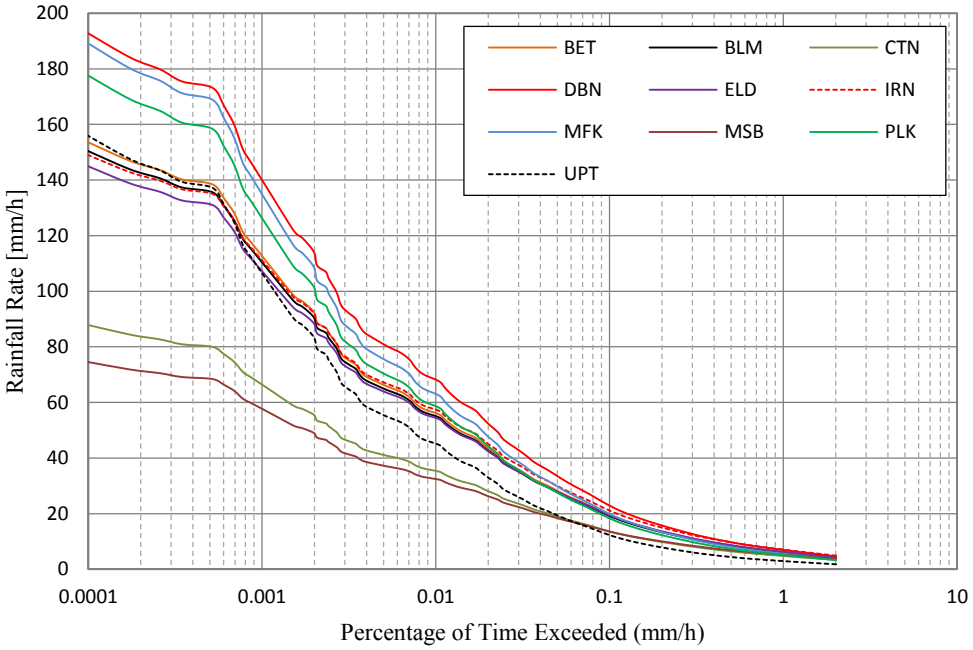

(b)

Figure 3.8: Cumulative distributions for predicted rainfall rates at (a) one-minute and (b) 30-second integration times

3.5 Error Analysis for Proposed Power-law conversion Models over Durban

Owing to lack of measured one-minute data for other locations under study, predicted one-minute values are compared with [*ITU-R P.837-6, 2012*] proposed one-minute rainfall rate exceedence values. Table 3.12 shows these comparisons at 99.99% system availability. The lowest deviation error of -1.0% was observed from the proposed model for Bloemfontein, whereas the highest error of 7.0% is observed in the model proposed for Cape Town. Nevertheless, it is observed that predicted values are comparable to ITU-R values with some slight deviations. This is expected because the empirical measurement analysis gives more accurate values of rainfall intensities for a particular location under study as opposed to regional values that are more generalized. These deviations may be caused by variations in climatic conditions from one location to another within the same region.

Table 3.12 Comparison of predicted $R_{0.01}$ for one-minute with ITU-R proposed values (*See* Figure A-1 in Appendix A)

	$\boldsymbol{R_{1,Y} = m(R_{5,DBN})^n}$ [mm/h]		
Loc.	**$R_{1,Y}$**	**ITU-R**	**Deviation (%)**
BET	50.7	50	1.4
BLM	49.5	50	-1.0
CTN	32.1	30	7.0
DBN	61.3	63	-2.7
ELD	49.1	50	-1.8
IRN	51.8	50	3.6
MFK	56.8	60	-5.3
MSB	29.5	30	-1.7
PLK	52.9	50	5.8
UPT	40.8	40	2.0

3.6 Specific Attenuation Prediction at Ku, Ka and V bands

The fast growing need for high capacity and high speed links for wireless communications is pushing network service providers towards utilization of Ku, Ka and V bands for both terrestrial and satellite communications. Services that need high channel capacity include multipoint video distribution services (MVDS), wireless broadband access (WBA) and other broadband services [*Emiliani et al.,* 2009]. The major obstacle in operating at high frequency-bands is signal attenuation caused by electromagnetic wave absorption and scattering in high intensity rainfall rates. An empirical procedure based on the power-law function relating rainfall rate and specific attenuation as proposed by [*ITU-R P.838-3,* 2005] is applied in this section. Specific attenuation values were determined at Ku, Ka and 60 GHz bands as shown in Fig. 3-9 and Table 3-14. The 60 GHz channel is an unlicensed band that has been identified for use in short range wireless communications due to its high speed capability and frequency reuse [*Guo et al., 2004*]. As was given in Section 2.9, ITU-R P.838-3 [2005] provides a systematic guide in the calculation of specific attenuation, γ_R, for one-minute rainfall on the link as:

$$\gamma_R = kR_1^{\alpha} \quad [dB/km] \tag{3.13}$$

where R_1, in mm/h, is the rainfall rate at one-minute, while k and α are frequency and polarization dependent coefficients, usually provided by ITU-R P.838-3 (2005).

By following the assumption that values of k and α in (3.13) are wholly frequent-dependent, as deduced in the technical publication of ITU-R P.838-3 (2005), it then logically follows from the earlier procedure in (3.7) - (3.9) that the equivalent computation of specific attenuation for 30-seconds rainfall rate over any location in South Africa is given as:

$$\gamma_{R,30s} = k(xR_{30}^{y})^{\alpha} \quad [dB/km] \tag{3.14}$$

where x and y represent the required power-law coefficients for conversion of 30-second rainfall data to one minute as obtained over the investigated locations.

A set of coefficients for the three frequencies considered are given in Table 3-13. Specific attenuation values were estimated at one-minute integration time at Ku (12 GHz), Ka (30 GHz) and 60-GHz bands and are presented in Figure 3-9 and Table 3-14 for all locations under study.

Table 3.13 ITU-R frequency-dependent coefficients for estimation of specific attenuation [ITU-R P.838-3, 2005].

FREQUENCY (GHz)	k_H	$\propto_H$	k_V	$\propto_V$
12	0.0236	1.1825	0.02455	1.1216
30	0.2403	0.9485	0.2291	0.9129
60	0.8606	0.7656	0.8513	0.7486

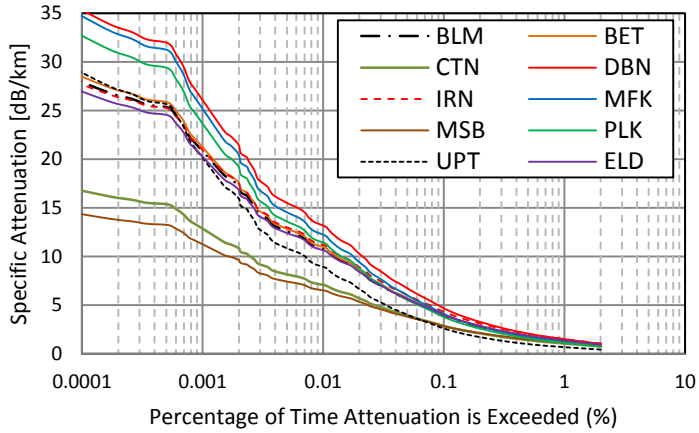

(a)

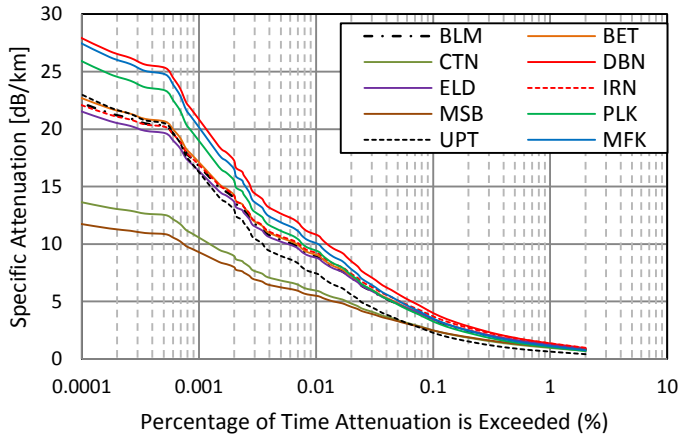

(b)

Figure 3-9 Specific attenuation estimates from predicted one-minute data at 30 GHz Band for (a) Horizontal polarization (b) vertical polarization

Table 3.14 Predicted Specific Attenuation calculation over South Africa using at 99.99% system availability requirements

LOCATION	FREQUENCY (GHz)	Specific Attenuation [dB/km]			
		H_{60s}	H_{30s}	V_{60s}	V_{30s}
BET	12	2.48	2.77	2.01	2.23
	30	9.95	10.9	8.25	8.99
	60	17.4	18.7	16.1	17.3
BLM	12	2.41	2.69	1.95	2.17
	30	9.73	10.6	8.07	8.8
	60	17.1	18.3	15.8	17
CTN	12	1.44	1.6	1.2	1.33
	30	6.45	7.02	5.44	5.9
	60	12.3	13.1	11.4	12.2
DBN	12	3.1	3.47	2.48	2.77
	30	11.9	13.1	9.81	10.7
	60	20.1	21.6	18.5	19.9
ELD	12	2.38	2.67	1.94	2.15
	30	9.65	10.6	8.01	8.74
	60	17	18.2	15.7	16.9
IRN	12	2.54	2.85	2.06	2.29
	30	10.2	11.1	8.41	9.2
	60	17.7	19	16.4	17.6
MFK	12	2.83	3.18	2.28	2.54
	30	11.1	12.2	9.15	10
	60	19	20.4	17.5	18.8
MSB	12	1.31	1.45	1.09	1.21
	30	5.95	6.49	5.03	5.47
	60	11.5	12.3	10.7	11.5
PLK	12	2.6	2.92	2.1	2.34
	30	10.4	11.3	8.58	9.36
	60	18	19.3	16.6	17.8
UPT	12	1.92	2.14	1.57	1.75
	30	8.1	8.85	6.77	7.37
	60	14.7	15.8	13.7	14.7

Observations from Table 3-14 indicate that, for instance, there is need to allocate more fade margins for communication links over Durban than Mossel Bay over the same link length. Otherwise, communication links over Durban need to be shorter than those at Mossel Bay at the same frequency. Another observation drawn from this table shows that predicted specific attenuation values using horizontal polarization, are higher than those obtained when using vertical polarization. For instance, there is general average margin of 0.45 dB/km at 12 GHz, 1.56 dB/km at 30 GHz and 1.24 dB/km at 60 GHz for one-minute rainfall at the considered locations in South Africa. Similarly, the trend observed for predictions over 30-second are 0.50 dB/km, 1.76 dB/km and 1.3 dB/km respectively. This suggests that specific attenuation at 30-second integration time requires a slightly higher margin to achieve rain fade mitigation at all these locations. Also, it is confirmed that specific attenuation due to rainfall increases as frequency of operation increases, as expected. This implies that a consequent increase or decrease in rainfall rate also affects the system availability. As a result, the occurrence of high rainfall rate in Durban will affect the performance of radio links.

3.7 Chapter Summary

Using cumulative distributions obtained from measured data, rainfall rate conversion models for 10 locations over South Africa were successfully determined via the power-law function. Subsequently, outputs from predicted one-minute models for all locations under study were compared with ITU-R proposed $R_{0.01}$ values and errors generated indicate that these new models can be relied on in conversion of available 5-minute data to one-minute and 30-second data for planning of reliable communication systems over South Africa.

In Chapter four, disdrometer rainfall DSD data over Durban are used to model raindrop size distributions for one-minute and 30-second integration times using the lognormal and modified gamma rainfall DSD models. Also, a conversion model for conversion from 60-second to 30-second using measured DSDs is proposed. Afterwards, results of these models are then compared and discussed for 30-seond and one-minute integration times.

CHAPTER 4

Rainfall Drop Size Distribution Modelling and Conversions

4.1 Introduction

In Chapter three, rainfall rate conversion models were developed over 10 regions in South Africa for conversion of rainfall rates from higher integration time to lower integration time. Predicted rainfall rates from these models confirmed that lower integration time statistics improves the accuracy in estimating specific attenuation on wireless microwave links. This improvement is realized by higher values of rainfall rates obtained from rainfall statistics with measurements at lower integration times. These rainfall rates can then be utilized in the accurate estimation of rainfall attenuation along the links. An alternative to the use of rainfall rates in the estimation is the application of raindrop size distribution. Hence, information on raindrop size distribution (DSD), volumetric concentrations and their variability with rainfall rates and seasons is indispensable and becomes beneficial in the development of accurate models that can be used for accurate estimation of rainfall attenuation. Higher accuracy in estimation of attenuation then gives rise in the design of reliable microwave and millimeter wave communication links. Rainfall DSD studies are therefore very important and useful in various fields including microwave communication, cloud physics, satellite meteorology, tele-detection, soil erosion [*Ochou et al.,* 2007].

In this chapter, rainfall DSD measurements obtained from the Joss Waldvögel instrument are studied at two integration times of 30-second and 60-second. Previous studies related to rainfall DSDs in South Africa have utilized rainfall DSD measurements at 60-second integration time [*Owolawi,* 2011*; Afullo,* 2011*; Adetan and Afullo,* 2012*; Alonge and Afullo,* 2011*; Malinga et al.,* 2014]. In this study, rainfall DSD measurements at an integration time of 30-second are analyzed alongside the 60-second over Durban using lognormal and modified gamma rainfall DSD models and thereafter, a comparison carried out based on the two rainfall integration times and seasonal variations.

4.2 Rainfall Drop Size Distributions Over Durban

As was mentioned in Chapter two, a number of research studies on drop size distributions have been done for investigation of the behavior of rainfall microstructural properties over Durban. These studies include research work by *Afullo* (2011), *Alonge and Afullo* (2011), *Owolawi* (2011), *Alonge and Afullo* (2012b), *Alonge and Afullo* (2014), *Adetan and Afullo* (2014). In these previous studies, one-minute integration time measurements have been so far considered. In this study, rainfall DSDs are developed for rainfall measurements at 30-second and 60-second integration time for comparisons and determination of statistical rainfall DSD models that best fit each category. Lognormal and Gamma

rainfall DSD models are employed in this study with method of moment (MM) and maximum likelihood estimation (ML) parameter estimation techniques.

4.2.1 Method of Moments (MM) Parameter Estimation Technique

This technique requires the grouping of data, the knowledge of Moment Generating Function (MGF) and the statistical distribution to be used [*Garcia*, 2008; *Kreyszig*, 2011].

The *i*th moment of the distribution of a random variable, if it exists, is given by:

$$\mu_i = E\{X^i\} \tag{4.1}$$

Hence, the estimate for μ_i from $X_1, X_2, \ldots X_n$ independent and identically distributed (i.i.d.) becomes,

$$\hat{u}_i = \frac{1}{n}\sum_{i=1}^{n} X^i \tag{4.2}$$

The Method of moments is based on the assumption that parameters θ_1, θ_2 to be estimated can be written as functions of the moments resulting to:

$$\theta_1 = f_1(\mu_1, \mu_2) \tag{4.3}$$

and

$$\theta_2 = f_2(\mu_1, \mu_2) \tag{4.4}$$

With these assumptions, then the natural estimates for θ_1 and θ_2 become:

$$\hat{\theta}_1 = f_1(\hat{u}_1, \hat{u}_2) \tag{4.5}$$

$$\hat{\theta}_2 = f_2(\hat{u}_1, \hat{u}_2) \tag{4.6}$$

where $\hat{u}_1$ and $\hat{u}_2$ are the estimates for the ith moments of the distribution.

A general moment generation function for a continuous random variable *x* is given as:

$$M_n = \int_{-\infty}^{\infty} x^n f_x(x)\, dx \tag{4.7}$$

where M_n is the *n*th moment function of the random variable *X*.

Hence, the moment generation function for a discretized random variable, x, can be estimated as:

$$M_n \approx \sum_{i=1}^{N} x_i^{\,n}\, p_x(x_i)\Delta x_i \tag{4.8}$$

where $p_x(x_i)$ is the discrete probability function, Δx_i is the interval between adjacent classes and N is the sample size

From (4.8), the moment function for a discrete random variable in DSD studies is given by [*Ajayi and Olsen,* 1985*; Afullo,* 2011*; Alonge,* 2011]

$$M_n = \sum_{i=1}^{N} D_i^{\,n}\, N(D_i) dD_i \tag{4.9}$$

where $N(D_i)$ is the drop size distribution, dD_i is the mean drop diameter interval between two successive drop sizes and D_i is the mean drop diameter in the ith class and N is the sample size.

From (4.9), the most commonly used method of moments are M_0, M_3, M_4 and M_6. Research has indicated that the third, fourth and sixth moments are very useful in the estimation of distribution parameters N_T, μ and σ [*Timothy et al., 2002; Das et al,* 2010*; Kozu and Nakamura,* 1991]. Commonly used moments are:

$$M_0 = \sum_{i=1}^{N} N(D_i)\, dD_i \tag{4.10a}$$

$$M_3 = \sum_{i=1}^{N} D_i^{\,3} N(D_i)\, dD_i \tag{4.10b}$$

$$M_4 = \sum_{i=1}^{N} D_i^{\,4} N(D_i)\, dD_i \tag{4.10c}$$

$$M_6 = \sum_{i=1}^{N} D_i^{\,6} N(D_i)\, dD_i \tag{4.10d}$$

where M_0, M_3, M_4 and M_6 represent rainfall drop concentration, rainfall rate and water liquid content, rainfall specific attenuation and radar reflectivity, respectively.

The mean, μ, and standard deviation, σ, are computed from experimental DSD measurements as:

$$\mu = \frac{1}{N}\sum_{i=1}^{N} \ln(D_i) \tag{4.11}$$

$$\sigma = \left[\frac{1}{N}\sum_{i=1}^{N} (\ln(D_i) - \mu)^2\right]^{0.5} \tag{4.12}$$

where D_i is the mean drop diameter in the ith class and N is the total number of drops per rain sample.

4.2.1.1 Lognormal DSD Input Parameters from MM Parameter Estimation

From discussion in Section 2.7, the general lognormal DSD probability density function is given in [*Ajayi and Olsen,* 1985] as:

$$N(D_i) = \frac{N_T}{\sigma D_i \sqrt{2\pi}} \exp\left\{-\frac{1}{2}\left[\frac{\ln(D_i) - \mu}{\sigma}\right]^2\right\} \qquad [m^{-3}mm^{-1}] \tag{4.13}$$

where $N(D_i)$ is the rain drop size distribution and N_T is the drop concentration and μ and σ are the mean and standard deviation respectively.

The three parameters of the lognormal model in (4.13) were estimated using the method of moment parameter estimation technique that estimates input parameters of a statistical distribution by means of equating theoretical moments of a known distribution to actual moments of the sampled data.

The moments M_3, M_4 and M_6 in (4.10), are computed using the moment generation function expressed in the form:

$$M_k = N_T \exp[k\mu + 0.5(k\sigma)^2] \tag{4.14}$$

Consequently, using M_3, M_4 and M_6, values of lognormal DSD parameters N_T, μ and σ, are estimated by expressions proposed by [*Kozu and Nakamura,* 1991]:

$$N_T = \exp[(24L_3 - 27L_4 + 6L_6)/3] \tag{4.15}$$

$$\mu = (-10L_3 + 13.5L_4 - 3.5L_6)/3 \tag{4.16}$$

$$\sigma^2 = (2L_3 - 3L_4 - L_6)/3 \tag{4.17}$$

where L_3, L_4, L_6 are natural logarithms of M_3, M_4 and M_6 measured moments given by $L_n = ln\left(\mathrm{M_n} = \sum_{\mathrm{i=1}}^{\mathrm{N}} \mathrm{D_i}^{\mathrm{n}}\, \mathrm{N(D_i)dD_i}\right)$.

Lognormal parameters N_T, μ and σ obtained in (4.15) - (4.17) are hereby related to rainfall rate, R, as:

$$N_T = a_T R^{b_T} \tag{4.18}$$

$$\mu = b_\mu + a_\mu \ln(R) \tag{4.19}$$

$$\sigma = [b_\sigma + a_\sigma + \ln(R)]^{0.5} \tag{4.20}$$

where R is the rainfall rate, a and b are regression coefficients and N_T as defined in (4.18).

4.2.1.2 Modified Gamma DSD Method of Moments Estimation

The gamma rainfall DSD model, discussed in Section 2.7, is expressed as [*Atlas and Ulbrich,* 1974; *Ulbrich*, 1983; *Kozu and Nakamura* 1991]:

$$\mathrm{N(D_i) = N_m(D_i)^{\mu} exp(-\Lambda D_i)} \qquad [\mathrm{m^{-3}mm^{-1}}] \tag{4.21}$$

where $N(D_i)$ is the rain drop size distribution, N_m is the scaling parameter, μ is the shape parameter and Λ is the slope parameter and D_i is the mean rain drop diameter in the interval D to $D+\Delta D$.

For estimation of gamma DSD model parameters in (4.21), method of moments were also used here, with a moment function in the modified Gamma model given as:

$$M_n = N_m \frac{\Gamma(\mu + n + 1)}{\Lambda^{\mu+n+1}} \tag{4.22}$$

where N_m is the intercept parameter, Λ is the slope parameter and μ, the shape parameter.

Solutions to theoretical moments in (4.22) are given in [*Kozu and Nakamura,* 1991; *Lakshmi et al*., 2011] as:

$$\mu = \frac{11\mathrm{F} - 8 + \sqrt{\mathrm{F(F+8)}}}{2(1-\mathrm{F})} \tag{4.23}$$

where F is a function of the third, fourth and fifth moments and is given by:

$$F = \frac{M_4{}^3}{M_3{}^2 M_6} \tag{4.24}$$

In the same way, the two remaining parameters, N_m and Λ, are expressed as:

$$N_m = \frac{M_3 \Lambda^{\mu+4}}{\Gamma(\mu+4)} \tag{4.25}$$

$$\Lambda = \frac{M_3(\mu+4)}{M_4} \tag{4.26}$$

Alternatively, the value of μ can be set to fixed value such that Λ and N_m are estimated by the only two moments, M_3 and M_4. In this study, the fixed μ model is used with $\mu = 3$. The other remaining two parameters of the Modified Gamma DSD are fitted against measured rainfall rate, R, and represented as:

$$N_m = a_m (R)^{b_m} \tag{4.27}$$

$$\Lambda = a_\Lambda (R)^{b_\Lambda} \tag{4.28}$$

where a_m, b_m, a_Λ and b_Λ are regression coefficients.

4.2.2 Lognormal rainfall DSD Method of Maximum Likelihood (ML) Estimation

In finding a point estimator, the maximum likelihood estimation method selects at its best, the parameter value that maximizes the probability of the observed data. For observed data $X_n = (X_1, X_2, \ldots X_n)$, the maximum likelihood method selects the parameter that maximizes the probability of occurrence of X_n [*Garcia*, 2008; *Kreyzig*, 2011]. If observable values of a random variable, X, are $X_n = (x_1, x_2, \ldots, x_n)$, then the likelihood function of the sample is a function defined as:

$$l(x_n; \theta) = l(x_1, x_2, \ldots, x_n; \theta) \tag{4.29}$$

$$= \begin{cases} p_X(x_1, x_2, \ldots, x_n|\theta), & X \text{ discrete random variable} \\ f_X(x_1, x_2, \ldots, x_n|\theta), & X \text{ continous random variable} \end{cases} \tag{4.30}$$

where p_X and f_X are the joint pmf and joint pdf respectively.

As $X_1, X_2, \ldots X_n$ are iid, the resultant likelihood function is expressed as:

$$p_X(x_1, x_2, \ldots, x_n|\theta) = p_X(x_1|\theta) p_X(x_2|\theta) \ldots p_X(x_n|\theta) = \prod_{j=1}^{n} p_X(x_j|\theta) \tag{4.31}$$

and correspondingly,

$$f_X(x_1, x_2, \dots, x_n|\theta) = f_X(x_1|\theta) f_X(x_2|\theta) \dots f_X(x_n|\theta) = \prod_{j=1}^{n} f_X\left(x_j|\theta\right) \tag{4.32}$$

For maximization of the likelihood function, selection of the estimator value $\hat{\Theta} = \theta'$ with θ' as the parameter value that maximizes the likelihood function, the following expression holds:

$$l(x_1, x_2, \dots, x_n; \theta^*) = \max_{\theta} l\,(x_1, x_2, \dots, x_n; \theta) \tag{4.33}$$

For convenience, the log likelihood function is used due to ease of working with sum of terms as compared to the product of terms, thus:

$$L(\mathbf{x}_n|\theta) = \ln l\,(\mathbf{x}_n; \theta) \tag{4.34}$$

$$= \begin{cases} \sum_{j=1}^{n} \ln p_X\left(x_j|\theta\right) = \sum_{j=1}^{n} L\left(x_j|\theta\right) \quad , & \text{X discrete random variable} \\ \sum_{j=1}^{n} \ln f_X\left(x_j|\theta\right) = \sum_{j=1}^{n} L\left(x_j|\theta\right) \quad , & \text{X continous random variable} \end{cases} \tag{4.35}$$

The method of maximum likelihood was used in the estimation of the lognormal DSD model in (4.13) and parameters μ and σ from measured data were determined as:

$$\mu_{ML} = \frac{1}{n} \sum_{n=1}^{n} \ln(D_i) \tag{4.36}$$

$$\sigma_{ML} = \left[\frac{1}{n} \sum_{n=1}^{n} (\ln(D_i) - \mu_{ML})^2\right]^{0.5} \tag{4.37}$$

The third parameter, N_T was optimized from the self-consistency rule of rainfall DSD such that:

$$N_{T,opt} = \frac{R}{6\pi \times 10^{-4} \sum_{i=1}^{N} D^3 f(D) V(D) dD} \tag{4.38}$$

Thereafter, using (4.36) - (4.38), estimation of lognormal parameters by the method of maximum likelihood are presented as:

$$N_{T,opt} = a_T(R)^{b_T} \quad (4.39)$$

$$\mu_{ML} = b_\mu + a_\mu \ln(R) \quad (4.40)$$

$$\sigma_{ML} = b_\sigma + a_\sigma \ln(R) \quad (4.41)$$

4.3 Measurement and Data Processing

Rainfall DSD measurements that are used in this chapter were obtained from disdrometer instruments described in Section 3.2. This instrument is capable of measuring both rainfall rates and rain drop statistics concurrently and hence is a vital tool provision of both rainfall rates and rainfall DSD measurements. The set up that is used in this chapter is similar to that presented in Fig.3.1, but with the main parameter of interest in the measurement being the rainfall drop size distribution.

The 30-second (30s) data and one-minute (60s) data were categorized into annual and seasonal categories as presented in Table 4.1. The term 'annual' in this context refers to overall data at a given integration time, comprising of all seasons. Regarding seasonal category, South Africa, experiences four seasons namely: Summer (mid October to mid February), Autumn (mid February to April), Winter (May to July) and Spring (August to mid October). It is to be noted the boundaries between seasons are not certain due to seasonal overlaps, but for data categorization purposes, we need to have our running boundaries.

Table 4.1 Rainfall DSD measurements over Durban

Int. time (sec)		**Summer**	**Autumn**	**Spring**	**Winter**	**Annual**
30	Samples	29,110	14,738	7,881	6,721	71,552
	Total Rain [mm]	31,622	17,659	4,729	7,150	79,491
	Max. drops	1,067	1,019	725	826	1,067
60	Samples	9,324	9,325	10,951	5,652	58,031
	Total Rain [mm]	10,455	10,455	4,415	6,570	45,937
	Max. drops	2,118	2,118	1,846	1,971	2,532

4.4 Seasonal variations of rainfall DSD

Estimation of statistical model parameters for different seasons was carried out using the Method of Moments and the maximum likelihood method. Table 4.2 shows lognormal DSD estimated parameters using the method of moments. From this table, at 30-second integration time, it is observed that the drop concentration N_T, varies randomly for the seasons of summer, autumn, spring and winter, with spring having the highest value of 70.6 and winter with lowest value of 32.2. On the other hand, at 60-second, this parameter is observed to decrease from summer, autumn, spring and winter.

From Table 4.3, it is generally observed that at 60-second, there is a decreasing trend of the concentration parameter from summer, spring, autumn and winter at 60-second integration time. At 30-second integration time, this parameter is seen to decrease from spring, autumn, summer and winter. Hence, it is observed that the month of winter has the least value of this parameter at both integration times.

Table 4.4 presents modified gamma parameter with method of moments parameter estimation. At 30-second, optimized values of the N_m parameter is highest in spring, followed by autumn, then summer and lastly winter. At 60-second integration time, this parameter is highest in autumn

Table 4.2 Estimation of Lognormal parameters using Method of Moments technique over Durban

Integ. Time (sec)	**Category**	$N_T = a_T R^{b_T}$		$\mu_{MM} = a_\mu \ln(R) + b_\mu$		$\sigma^2{}_{MM} = a_\sigma \ln(R) + b_\sigma$	
		a_T	b_T	a_μ	b_μ	a_σ	b_σ
30	Summer	247.5	0.3693	0.1395	-0.3062	0.0118	0.0806
	Autumn	169.3	0.2964	0.1421	-0.3181	0.0107	0.0769
	Spring	246.7	0.3482	0.1411	-0.3111	0.0137	0.0834
	Winter	245.9	0.3661	0.1377	-0.3118	0.0137	0.0849
60	Summer	443.9	0.4644	0.1158	-0.4343	0.0104	0.0693
	Autumn	238.9	0.3748	0.1454	-0.2671	0.0081	0.0669
	Spring	183.2	0.4589	0.1225	-0.2269	0.0086	0.0803
	Winter	57.5	0.2490	0.1876	0.1017	0.0056	0.0709

Table 4.3 Estimation of Lognormal parameters using Maximum Likelihood technique

Integ. Time (sec)	**Category**	$N_{T,opt} = a_T R^{b_T}$		$\mu_{ML} = a_\mu \ln(R) + b_\mu$		$\sigma_{ML} = a_\sigma \ln(R) + b_\sigma$	
		$a_{T,ML}$	$b_{T,ML}$	$a_{\mu,ML}$	$b_{\mu,ML}$	$a_{\sigma,ML}$	$b_{\sigma,ML}$
30	Summer	56.1	0.4027	0.1948	-0.4040	0.0323	0.3293
	Autumn	43.4	0.4209	0.1965	-0.3266	0.0194	0.3487
	Spring	70.6	0.1906	0.2147	-0.4041	0.0649	0.3009
	Winter	49.1	0.4003	0.1776	-0.3490	0.0302	0.3491
60	Summer	234.0	-0.109	0.3033	-0.6954	0.0630	0.2447
	Autumn	107.8	0.1737	0.2529	-0.5577	0.0396	0.3001
	Spring	123.0	0.1176	0.2337	-0.5611	0.0356	0.3137
	Winter	32.2	0.4602	0.2072	-0.3459	0.0289	0.4267

Table 4.4 Estimation of Modified Gamma parameters using Method of Moments technique with parameter μ = 3

Integ. Time (Sec)	**Data Cat.**	$N_m = a_m(R)^{b_m}$		$\Lambda = a_\Lambda(R)^{b_\Lambda}$	
		N_m	b_m	a_Λ	b_Λ
30	Summer	9.7589×10^5	-0.032	6.6504	-0.141
	Autumn	1.09126×10^5	-0.533	6.5406	-0.195
	Spring	4.01582×10^5	-1.540	7.9270	-0.333
	Winter	9.2010×10^4	-0.759	7.1599	-0.229
60	Summer	2×10^6	-1.564	9.6740	-0.333
	Autumn	3.68752×10^5	-0.934	7.8013	-0.251
	Spring	492895×10^5	-0.764	8.0817	-0.226
	Winter	18801×10^4	-0.943	5.3221	-0.257

Figure 4.1 plots show summer rainfall distributions at 3.5 mm/h and 25.5 mm/h. It is observed that at 3.5 mm/h in Figure 4.1(a) and Figure 4.1(b), rainfall drop size distributions are almost similar at both integration times. This is more evident especially when all models underestimate measured DSDs with mean rain drop sizes above 3 mm. At 25.5 mm/h, it is observed that for lower rain drop sizes, the 60-

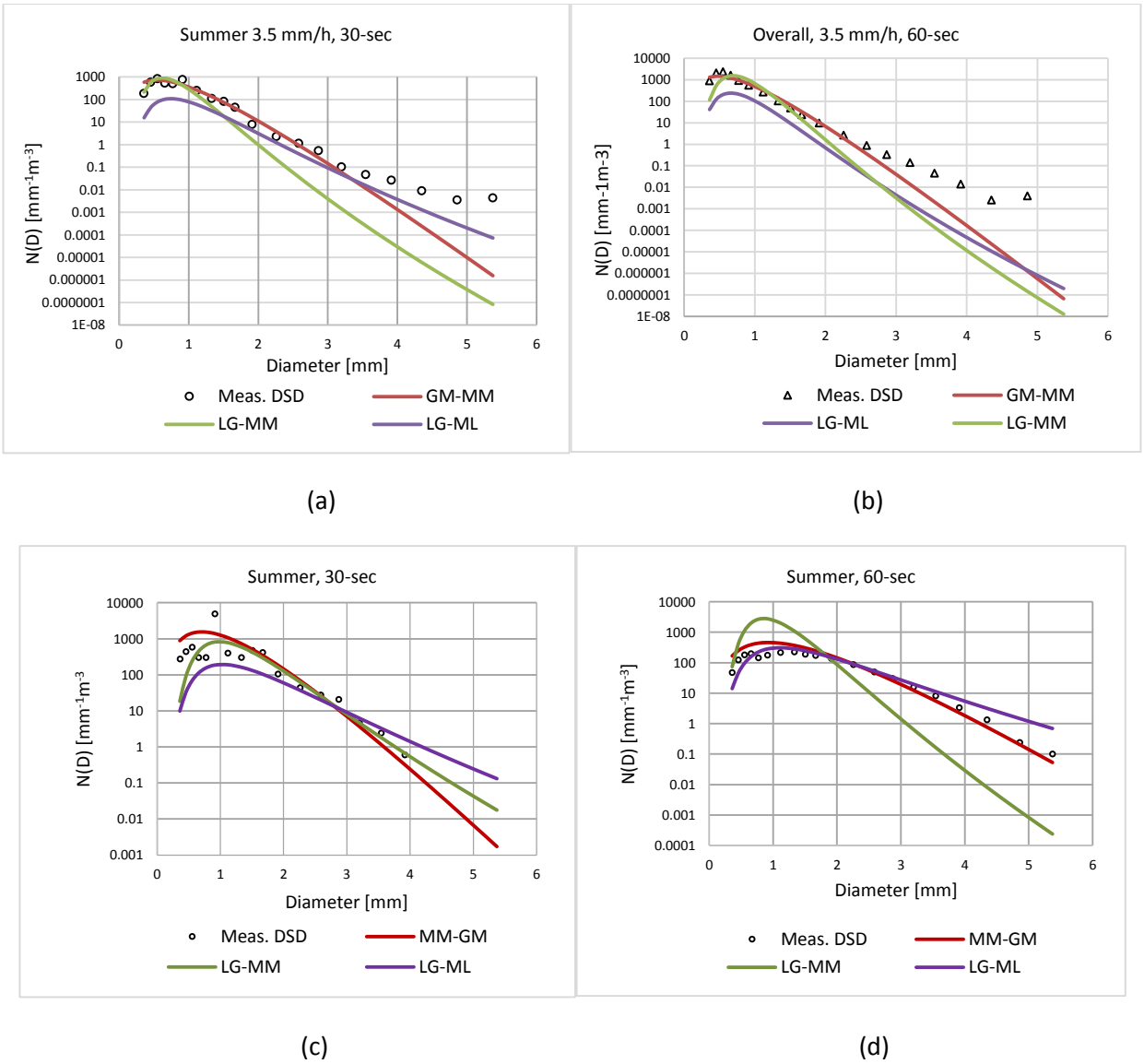

Figure 4.1 Seasonal rainfall DSDs for summer at (a)-(b) 3.5 mm/h (c)-(d) 25.5 mm/h

second DSDs, though lower in magnitude, vary evenly as compared to the pattern at 60-second integration time. The results further reveal that the gamma model correlates more with measured data than other models, at both integration times of 30-sec and 60-sec.

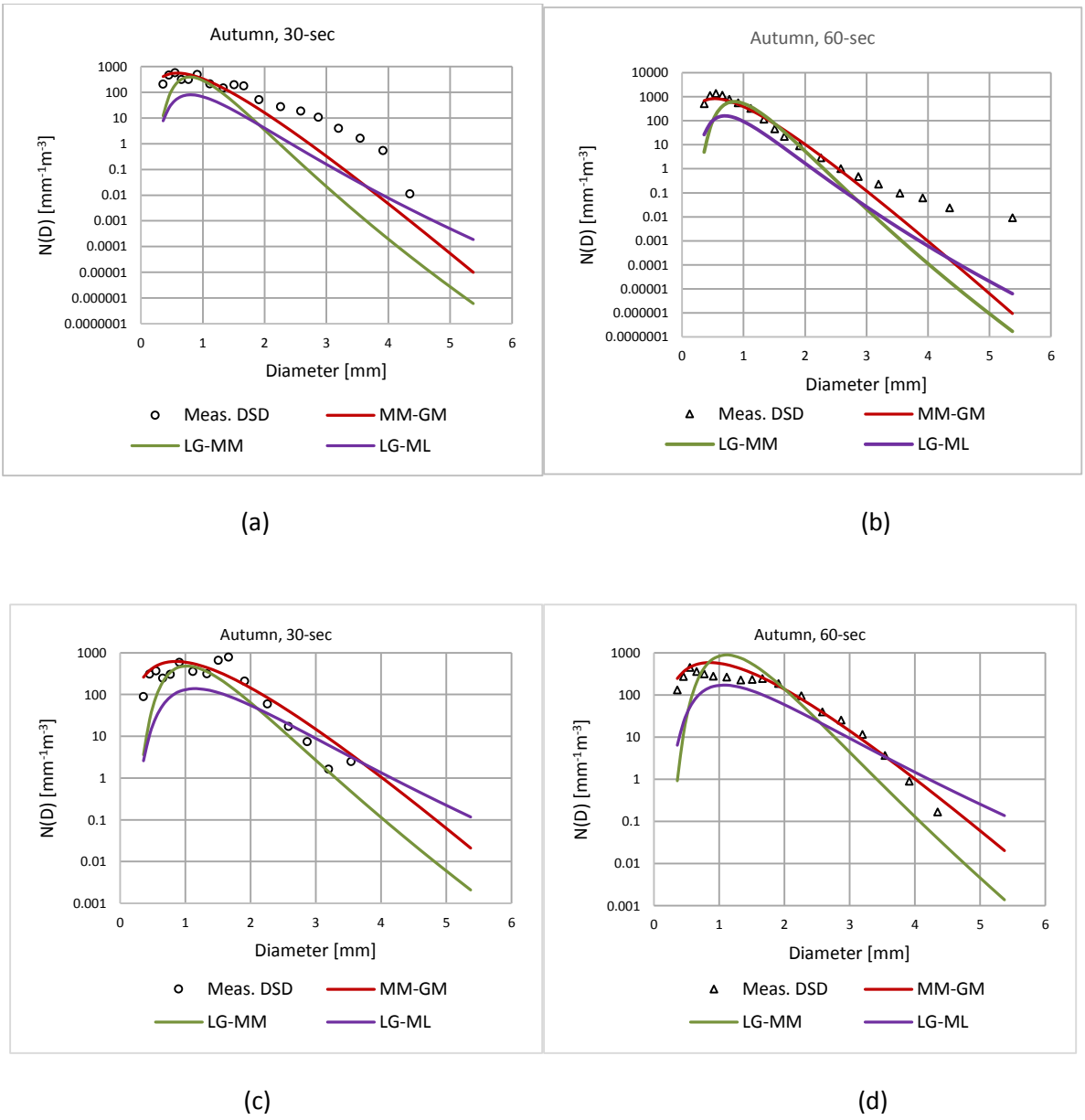

Figure 4.2 Seasonal rainfall DSDs for autumn at (a)-(b) 3.5 mm/h (c)-(d) 24.5 mm/h

In Figure 4.2, there is shown rainfall drop distributions for the season of autumn. From this figure, it is observed that drop distributions are higher at 30-sec for drop sizes in the range 2 mm < D < 4 mm than at 60-sec integration time. As regards the statistical models, they almost show similar results at both 60-second and 30-second integration times. The model that matches well the measured data at 60-sec integration time is the gamma model, especially at higher rainfall rates surrounding 24 mm/h.

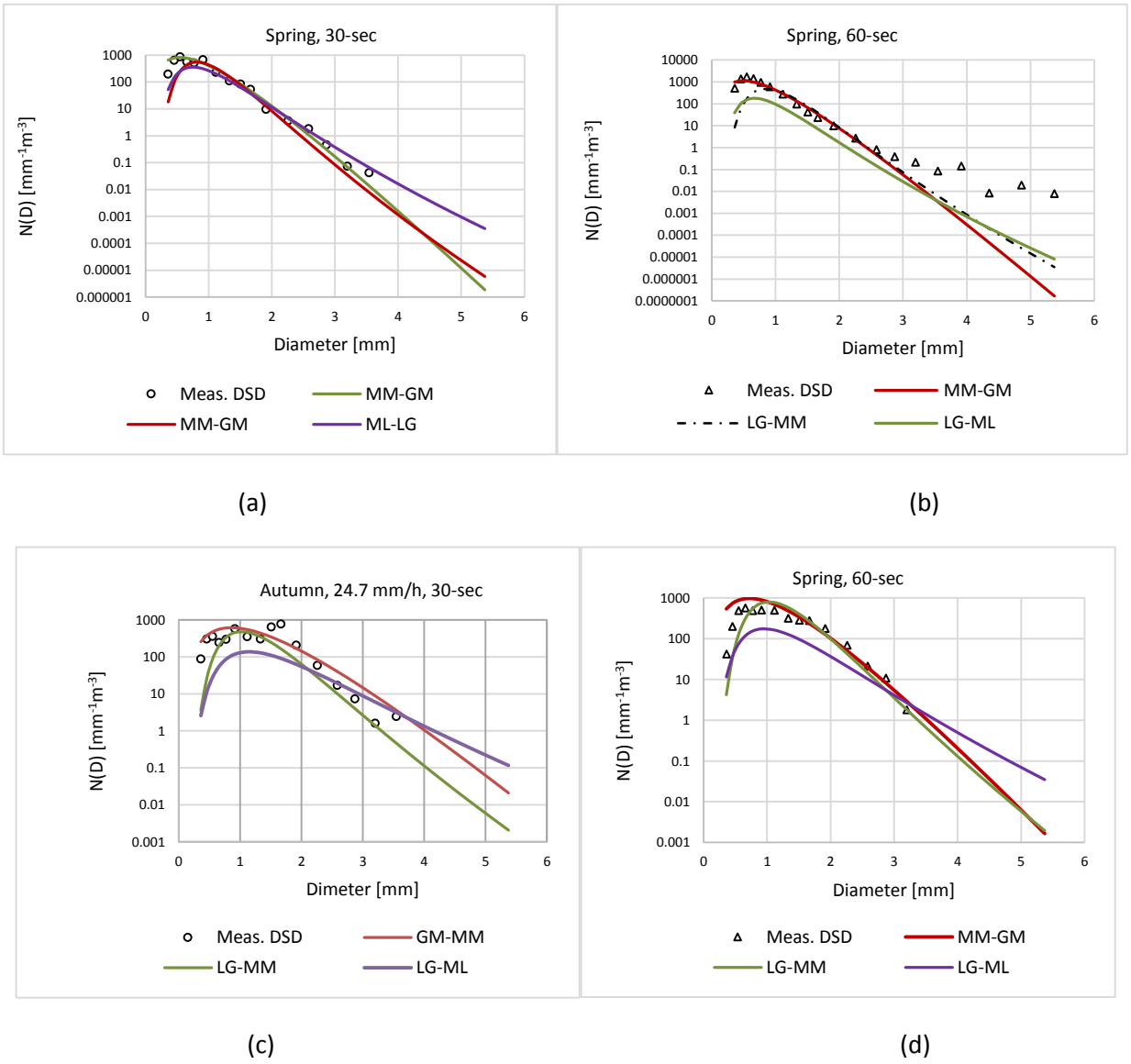

Figure 4.3 Seasonal rainfall DSDs for spring at (a)-(b) 3.5 mm/h (c)-(d) 20.5 mm/h

Figure 4.3 shows the DSD results for the season of spring. At a rainfall rate of 3.5 mm/h, all models approximate well measured DSDs with drop sizes larger than 3 mm at 30-second. On the other hand they all underestimate the measured DSDs for drops with diameters greater than 3 mm. At 20.5 mm/h rainfall rate, LG-MM model estimates well the measured DSDs for rain drops with diameters greater than 3 mm, whereas all models underestimate the DSDs for drops with diameters around 1 mm.

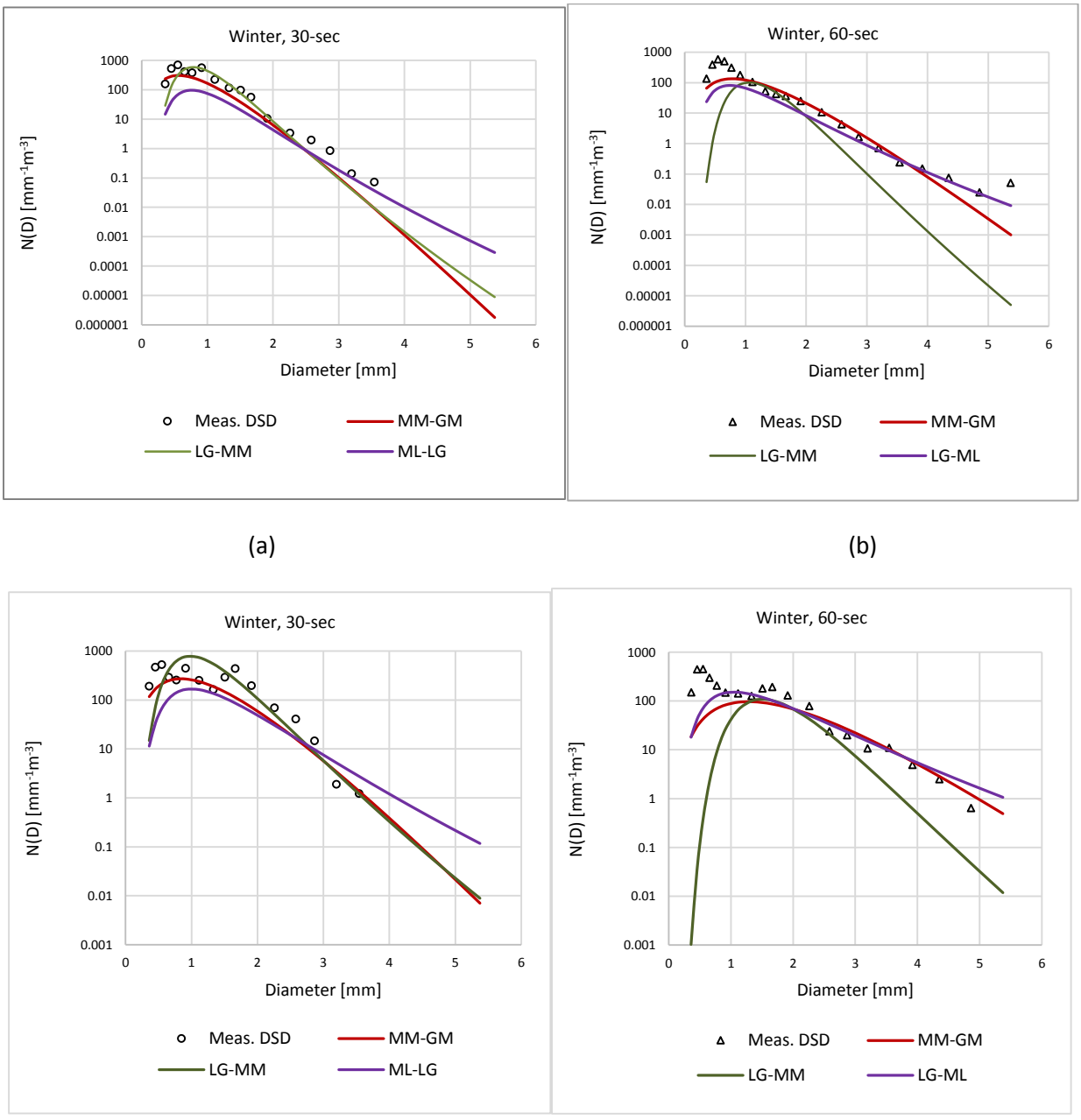

Figure 4.4 Seasonal rainfall DSDs for winter at (a)-(b) 3.5 mm/h (c)-(d) 22.5 mm/h

In Figure, 4.4, the rainfall DSD for winter is presented, where the Lognormal (MM) models estimates well rain drops below 2 mm diameter compared to other models at 30-seconds integration time. At 60-second integration time, all models underestimate drops below 1 mm, with the modified gamma model estimating well drops in the diameter range $2mm < D < 4$ mm. At 22.5 mm/h, at both integration times, there is uneven distribution pattern of drops below 2 mm diameter. Regarding the models used, the

lognormal is observed to greatly underestimate drops below 1 mm and above 2 mm. But generally, the gamma model best estimates the measured data at low rainfall rates especially at 60-second integration time. At 30-sec, the LG-MM model correlates well with measured data at higher rainfall of around 22 mm/h during the winter season.

4.5 Annual variations of rainfall DSD

Based on the fitted results from measured rainfall DSDs in Section 4.2, estimation of parameters for proposed statistical models are as presented in Table 4.5. From this table, it is observed that values of the raindrop concentration parameters N_T, $N_{T,opt}$ and N_m are higher for 60s data as compared with the same parameters at 30s data. Larger raindrop concentration at 60s is expected due to the longer sampling time. Other parameters are relatively close at both integration times.

Resultant rainfall DSDs arising from parameters estimated and presented in Table 4.5 are shown in Figure 4.6. A closer observation in this figure shows that at rain rates of R = 3.5 mm/h, the Modified Gamma model under-estimates raindrops with mean diameters above 2.584 mm. Nonetheless, this is not a major problem because at lower rainfall rates, the number of larger drops is considerably small, and the contribution of raindrops with small diameters to rainfall attenuation at lower rainfall rates is minimal. At 3.5 mm/h, LG-ML estimates well drops above 1 mm diameters sizes at 30-second, whereas at 60-second, it is observed that all models underestimate drops above 2.5 mm diameter sizes. But is observed that the modified gamma model estimates well drops with sizes below 1 mm.

At 61.2 mm/h, drop distributions are seen to be uneven for drops with diameters below 2 mm sizes at 30-second integration time compared to distributions for 60-second integration time. Also, it is observed that LG-MM model overestimates greatly drops with diameters in the range 1.5 mm < D < 2.5 mm but it performs well for drops with diameters greater than 3 mm.

Table 4.5 Estimated annual parameters for proposed rainfall DSD models over Durban

Model	Int. time (sec)	Parameters					
LG-MM		$N_T = a_T R^{b_T}$		$\mu_{MM} = a_\mu \ln(R) + b_\mu$		$\sigma_{ML} = a_\sigma \ln(R) + b_\sigma$	
		a_T	b_T	a_μ	b_μ	a_σ	b_σ
	30	230.1	0.3555	0.1454	-0.289	0.0112	0.0817
	60	270.2	0.4133	0.1309	-0.3141	0.0101	0.0743
LG-ML		$N_T = a_T R^{b_T}$		$\mu_{ML} = a_\mu \ln(R) + b_\mu$		$\sigma_{ML} = a_\sigma \ln(R) + b_\sigma$	
		$a_{T,ML}$	$b_{T,ML}$	$a_{\mu,ML}$	$b_{\mu,ML}$	$a_{\sigma,ML}$	$a_{\sigma,ML}$
	30	253.6	0.1449	0.1894	-0.3882	0.0447	0.3182
	60	545.6	-0.073	0.2585	-0.6311	0.0343	0.3513
GM-MM		$N_m = a_m (R)^{b_m}$		μ	$\Lambda = a_\Lambda (R)^{b_\Lambda}$		
		a_m	b_m		a_Λ		b_Λ
	30	2.36244×10^5	-0.653	3	6.9928		-0.191
	60	3.99070×10^5	-0.980	3	7.8760		-0.257

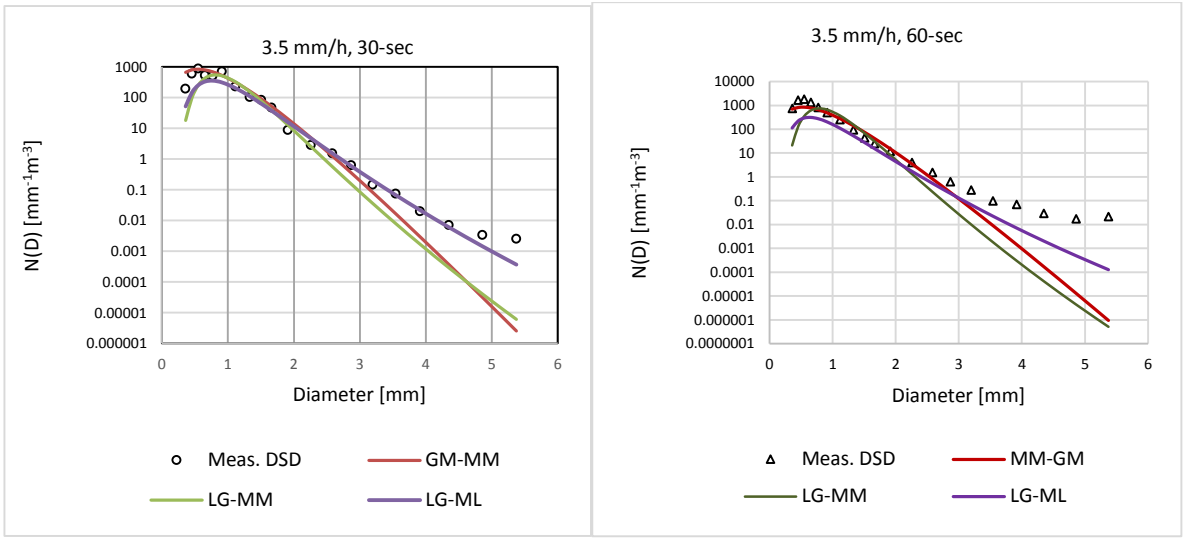

(a) (b)

Figure 4.5 Annual rainfall DSDs for at (a) 30-second (b) 60-second for rainfall rate for rainfall rate $R = 3.5$ mm/h

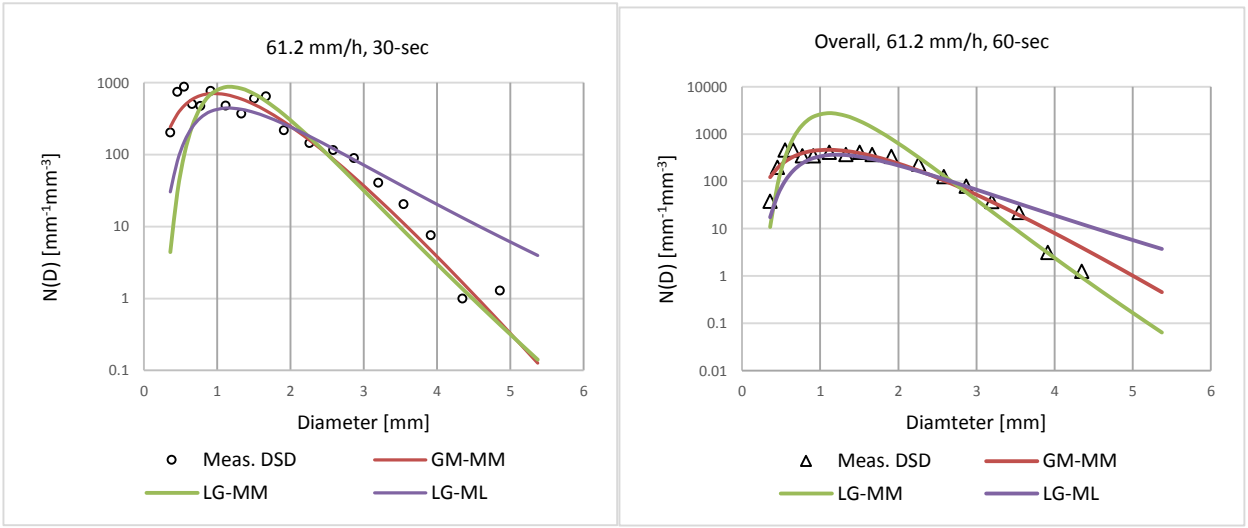

(a) (b)

Figure 4.6 Annual rainfall DSDs for different models at (a) 30-second (b) 60-second for rainfall rate for rainfall rate $R = 61.5$ mm/h

4.6 Determination of DSD Conversion between two integration times

Due to scarcity of rainfall statistics at lower integration times in most parts of the world, there is need to convert available higher rainfall measurements to their lower integration time equivalents. Therefore, from empirical DSD measurements over Durban, we investigated if there existed a relationship between measured 30-second and 60-second rainfall DSDs.

4.6.1 Channel-by-channel DSD correlations at 30-second and 60-second integration times

At equal rainfall rates, a fitting was done for corresponding 20 disdrometer channels (see Appendix C) at each integration time. Results of this channel-to-channel correlation are presented in Table 4.6. From this table, it is observed that a good correlation exists for drops in channels with mean drop diameters above 1 mm diameters. At small drops sizes in the bins with mean drop diameter below 0.3711 mm, the correlation is very poor. For the coefficient *b,* it is observed that for drop diameters above 4 mm diameter, the correlation is not as good as mean diameters below 4 mm.

From Table 4.6, coefficients *a* and *b*, were each fitting against the mean drop diameter, *D*, and the results of this fitting is shown in Figure 4.7 and Figure 4.8.

Table 4.6 Correlation of channel drops between 30-second and 60-second for annual data

Channel	$C_{i,30s} = a(C_{i,60s})^b$		
	a	***b***	**R^2**
C_1	5.4034	-0.0690	0.1054
C_2	24.095	-0.1000	0.0886
C_3	21.874	-0.0070	0.0016
C_4	17.555	-0.0118	0.0005
C_5	18.464	0.0227	0.104
C_6	7.315	0.4772	0.3711
C_7	1.5806	0.7276	0.6794
C_8	1.2197	0.7776	0.8289
C_9	1.4469	0.8442	0.9148
C_{10}	1.0708	0.9436	0.9555
C_{11}	0.3454	1.0108	0.9782
C_{12}	0.3272	1.0304	0.9848
C_{13}	0.4268	1.0606	0.9785
C_{14}	0.4343	1.0806	0.9757
C_{15}	0.294	1.1275	0.9569
C_{16}	0.3707	1.2034	0.9316
C_{17}	0.4143	1.2907	0.8244
C_{18}	0.429	1.2400	0.6641
C_{19}	1.0888	1.6232	0.7281
C_{20}	0.5198	1.3726	0.8004

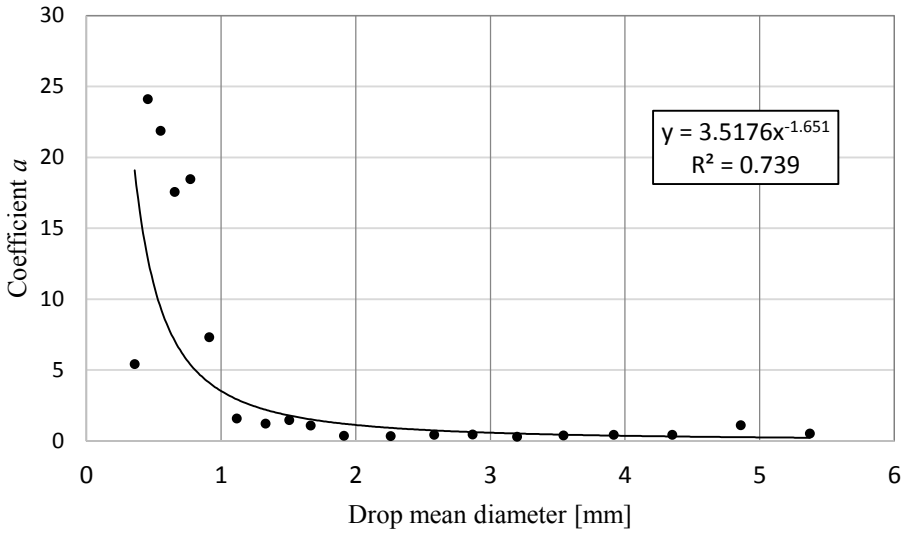

Figure 4.7 Fitting of coefficient *a* against drop mean diameter, *D*

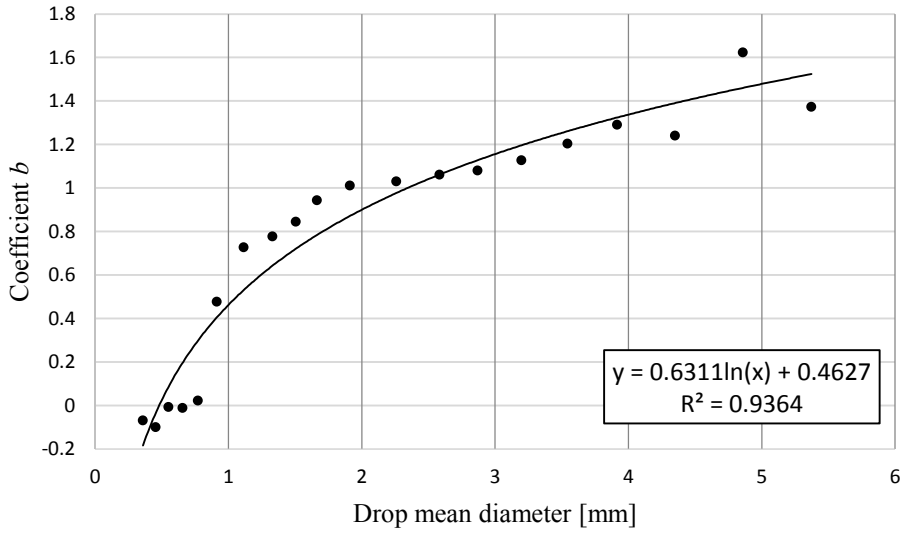

Figure 4.8 Fitting of coefficient *b* against drop mean diameter, *D*

Results of Fig. 4.7 and 4.8 shows that there exists a good channel-to-channel DSD for rain drops with a mean drop diameter of 1.116 mm (C_7) and above (See *Appendix C*). Medium to large sized rain drops dominate higher rainfall events and hence the channel-to-channel DSD conversions that are carried out between these two integration times will result in small deviations at higher rainfall rates.

4.6.2 Channel DSD conversion factors

From rainfall DSD measurements carried out over Durban as described in Section 4.3, a relationship exists between measured 30-second and 60-second DSDs given by:

$$\mathrm{C_{i,30}} = \mathrm{a_{ci}}\left(\mathrm{C_{i,60}}\right)^{\mathrm{b_{ci}}} \tag{4.42}$$

where $C_{i,30}$, and $C_{i,60}$ are average number of drops in the ith channel at 30-second and 60-second integration times respectively, and a_{ci} and b_{ci} are regression coefficients.

The values of coefficients a_{ci} and b_{ci} over Durban were established as:

$$\mathrm{a_{ci}} = 3.5176(\mathrm{D_i})^{-1.651} \tag{4.43a}$$

$$\mathrm{b_{ci}} = 0.4627 + 0.6311\ln(\mathrm{D_i}) \tag{4.43b}$$

Rain drop size distribution from empirical data is given by:

$$\mathrm{N(D_i)} = \frac{\mathrm{C_i}}{\mathrm{A \times T \times V_t \times dD_i}} \tag{4.44}$$

where C_i is the number of rain drop in the ith channel, A is the surface area of the disdrometer, V_t is the drop fall velocity and dD_i is the drop diameter interval.

Hence, by substituting the value of C_i in (4.44) with (4.42), the estimated 30-second DSD is therefore computed by:

$$\mathrm{N(D_i)} = \frac{\mathrm{a_{ci}}\left(\mathrm{C_{i,60}}\right)^{\mathrm{b_{ci}}}}{\mathrm{A \times T \times V_t \times dD_i}} \tag{4.45}$$

with the values of a_{ci} and b_{ci} as given in (4.43).

4.6.3 Error analysis for the DSD conversion model

The channel DSD model developed in (4.27) was used in the determination of rainfall DSD in (4.30) and results of the measured and estimated DSDs are shown in Figure 4.9 for rainfall rates, R = 3.5 mm/h and R = 34.5 mm/h. From these two figures, it is observed that the estimated 30-second DSD well estimates rain drops especially in the middle range of the disdrometer drop mean diameters. At R = 34.5 mm/h, it is observed that the proposed model slightly overestimates channel drops above 2 mm.

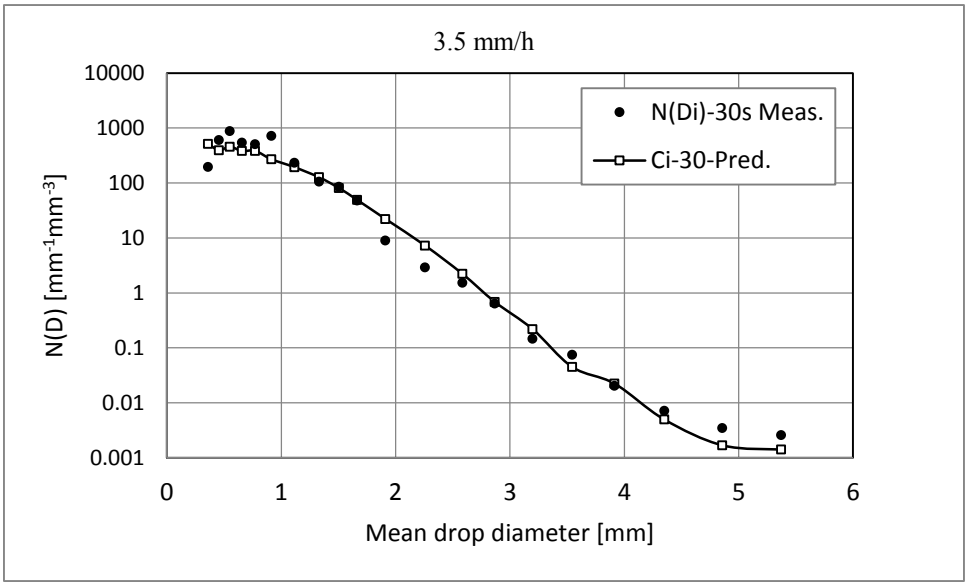

(a)

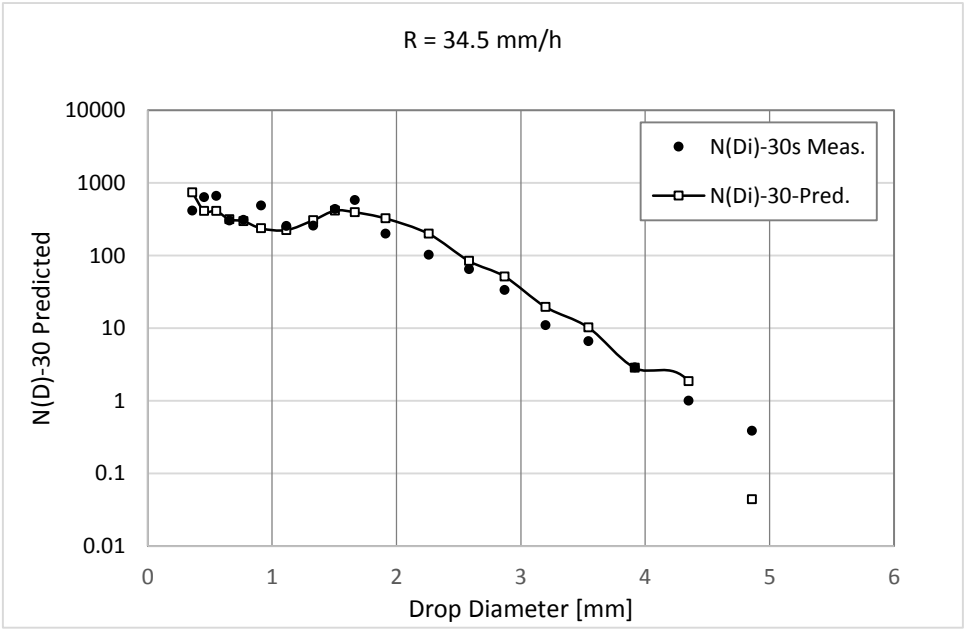

(b)

Figure 4.9 Comparison of measured and predicted rainfall DSD for 30-second at (a) R = 3.5 mm/h, (b) R = 34.5 mm/h

4.7 Error Analysis for Seasonal and Annual DSD models

Rodgers et al., (1976) and *Medeiros et al*. (1986), together with other researchers agree that due to complexity nature in the formation of rainfall, it is not easy to represent rainfall statistics by a universal rainfall DSD model. For the unfolding of suitable statistical rainfall DSD models over Durban, all proposed models were subjected to error analysis via the Root Mean Square Error (RMSE) technique presented in Section 3.2. This expression is given as:

$$\mathrm{RMSE} = \sqrt{\frac{1}{\mathrm{K}}\sum_{\mathrm{k}=1}^{\mathrm{K}}[\mathrm{O_k} - \mathrm{E_k}]^2} \tag{4.46}$$

where O_k and E_k are the measured and predicted rainfall rates respectively, with K being the sample size.

From analysis of the data measured at different integration times in this study, it is evident that the rainfall data sampling time may determine the suitable model that best fits. Further on, even at the same integration time, different models are best suited at different rainfall rates. This is evident in the error analysis of annual Rainfall DSD results presented in Table 4.7, where it is observed that the suitability of a model may be dependent on the rainfall rate and the integration time. For instance, at the same rainfall rate of 9.5 mm/h, the lognormal (MM) is best suited at 30s, whereas the modified gamma model is chosen at 60s integration time. In the case of same integration time of 60s, it is observed that the lognormal (ML) is preferred at 3.5 mm/h while the modified gamma is selected at 9.5 mm/h.

Further observations in Table 4.7 show that at lower rainfall rates, the lognormal (ML) performs better than other models at both integration times. Additionally, this model is seen to be suited at very high rainfall rates when data is sampled at 30s.

Table 4.8 shows error analysis on estimated 30-second rainfall DSDs at different rainfall rates. From this table, it is observed DSD predictions are fairly good at annual and seasons of summer, autumn and spring. The model is poorly represented in the month of winter.

Table 4.7 Model Error Analysis on annual DSD models

Rainfall, (R) (mm/h)	30s			60s			Suitable Model	
	LG MM	LG-ML	GM-MM	LG MM	LG-ML	GM-MM	30s	60s
3.5	0.6726	0.4774	0.8196	0.7553	0.5006	0.6119	Lognormal (ML)	Lognormal (ML)
9.5	0.4715	8.3462	0.7256	0.6812	0.7494	0.4912	Lognormal (MM)	Modified gamma
25.5	0.4929	1.6268	0.3973	1.5724	1.4627	0.6125	Modified gamma	Modified gamma
61.2	0.6315	3.0634	0.4055	1.2272	2.4752	0.8701	Modified gamma	Modified gamma
80<R<120	0.7343	0.6099	1.0300	1.6476	2.2831	0.8418	Lognormal (ML)	Modified gamma

Table 4.8 Error analysis on DSD conversion model

Data Category	RMSE
Annual	0.5588
Summer	0.5283
Autumn	0.6763
Spring	0.5336
Winter	1.3291

4.8 Chapter Summary

In this chapter, lognormal and modified gamma rainfall DSD model parameters were estimated using the Method of Moments and the Maximum Likelihood methods. These proposed models were then used to generate rainfall distributions for various data categories. Error analysis on the derived models revealed that the modified gamma model was best suited for rainfall measurements at 60-seconds whereas at 30-second, lognormal DSD model was best suited at lower rainfall rates at less than 10 mm/h and at high rainfall rates above 80 mm/h.

Additionally, correlation of 30-second and 60-second DSD was performed on measured data and the results showed a good correlation between the two integration times. This is evident in error lower RMSE errors that were generated. In the next chapter, rainfall DSDs that were modelled in this chapter will be utilized in the estimation of specific attenuation due to rain over Durban.

CHAPTER 5

Specific Attenuation patterns over Durban using 30-seconds data over Durban

5.1 Introduction

Using statistical distributions, rainfall DSDs for 30-second and 60-second data were investigated in Chapter four based on annual and seasonal rainfall variations. It was observed that rainfall DSDs vary with both the integration time and the season of the year. Additionally, we were able to estimate raindrop size distribution at 30-second integration time from 60-second integration time at a given rainfall rate. Raindrops are well known for their behavior or scattering and absorbing energy present in electromagnetic waves. When the wavelength of an electromagnetic wave is larger than the size of the raindrop, the signal is scattered. Conversely, when the wavelength is small compared to signal wavelengths, signal absorption occurs. Two useful scattering analysis techniques commonly employed for rain droplets are the Mie scattering and Rayleigh scattering.

With an assumption of spherical shape of a rain drop, *Alonge* (2011), in one of his studies, applied Mie scattering technique to develop extinction cross section power law coefficients for Durban. It is with immense agreement that Mie scattering analysis is often preferred due to its ability to provide reliable results beyond 3 GHz, as compared to Rayleigh scattering technique [*Mie,* 1908*; Bohren and Huffman,* 2004*; Naicker,* 2006*; Alonge,* 2011]. Drop size distribution and drop size density are among microscopic characteristics of rain that greatly affect microwave and millimeter wave links operating at frequencies above 10 GHz [*Ippolito,* 2008; *Emiliani et al.,* 2009]. Effects of these microscopic characteristics contribute greatly to attenuation and more so, *specific attenuation*, which is defined as attenuation measured for a path length of 1 km. The specific attenuation plays a major role in determination of the reliability of microwave and millimeter wave systems, and therefore, it is important that this value is estimated based on rainfall statistics of a location. For estimation of slant path attenuation, specific attenuation along the path becomes mandatory [Crane, 2003]. Specific attenuation can be computed directly from the rain rate as expressed in (2.31) or from rain drop distribution using (2.30) in which the extinction cross section parameter is involved. In this chapter, rainfall drop size distributions in Chapter four, in conjunction with the extinction cross section scattering parameters obtained by *Alonge* (2011) over Durban, are used in the estimation of specific rainfall attenuation, based on seasonal and annual data categories at 30-second and 60-second integration times.

5.2 Extinction Cross Section

An interaction between an electromagnetic wave and a rain drop of considerable size results in part of the wave energy being absorbed, another part being scattered and the reminder of the energy allowed to

flow through the raindrop. This area of interaction, also termed the *extinction cross section*, is very vital in the estimation of specific attenuation due to rain. *Mie* (1908), formulated equations related to complete scattering/absorption theory describing the interaction of electromagnetic wave energy and a spherical particle. According to Mie theory, the extinction cross section, σ_e, is expressed :

$$\sigma_e = \sigma_a + \sigma_s \tag{5.1}$$

where σ_a and σ_s are the absorption cross section and scattering cross section respectively.

The real part and the imaginary part of the refractive index of the scatter represent the scattering loss and absorption loss respectively [*Mie*, 1908]. Rain drops are known to be major scatters of electromagnetic waves of considerably small wavelengths. Hence, knowledge of the refractive index of water is vital in solving scientific and practical problems caused by water [*Schiebener et al.*, 1990].

5.2.1 Complex Refractive Index of water

In [*Mie*, 1991; *Alonge,* 2011], the complex refractive index of water, *m*, is mathematically given as:

$$m(f,T) = \sqrt{\epsilon(f,T)} \tag{5.2a}$$

and

$$\epsilon(f,T) = \epsilon' + i\epsilon'' \tag{5.2b}$$

where $\epsilon(f,T)$, a function of frequency and temperature, is the dielectric constant of water, with $\in'$ and $\in''$ being the real and loss parts respectively.

In the estimation of the dielectric constant of water for frequencies below 100 GHz, the single Debye model is commonly used for this estimation using the expression [*Liebe et al.,* 1991]:

$$\epsilon_D(f,T) = \frac{(\epsilon_0 - \epsilon_\infty)}{1 - i(f/\gamma_D)} + \epsilon_\infty \tag{5.3a}$$

and

$$\epsilon_0(T) = 77.66 - 103.3\theta \tag{5.3b}$$

$$\theta = 1 - \frac{300}{[273.15 + T]} \tag{5.3c}$$

$$\epsilon_\infty = 0.066\epsilon_0 \tag{5.3d}$$

$$\gamma_D(T) = 20.27 + 146.5\theta + 314\theta^2 \quad (5.3e)$$

where ϵ_0 is the static dielectric of pure water, ϵ_∞ is the high frequency constant and γ_D is the relaxation frequency.

5.2.2 Computation of the Extinction of Cross Section

In computation of scattering parameters, the real part of the forward scattering amplitude is useful in estimation of scattering parameters and is given by *Mie* [1908] as:

$$s(0) = \frac{1}{2}\sum_{n=1}(2n-1)[a_n + b_n] \quad (5.4)$$

where a_n and b_n are temperature and frequency dependent Mie scattering coefficients given in [*Odedina and Afullo,* 2009].

Using the real part of (5.4), the ECS of a transmitted wave can be estimated by [*Van de Hulst*, 1957]:

$$Q_{ext}(D) = \frac{4\pi}{k^2}\mathrm{Re}\{s(0)\} \quad (5.5)$$

where *D* is the mean raindrop diameter of the raindrop.

Research has established that ECS can also be related to raindrop diameter by the expression [*Olsen,* 1978*; Odedina and Afullo,* 2009*; Afullo,* 2011*; Alonge,* 2011]:

$$Q_{ext}(D_i) = a_{ext}\left(\frac{D_i}{2}\right)^{b_{ext}} \quad (5.6)$$

where a_{ext} and b_{ext} are coefficients dependent on temperature and frequency.

In the estimation of specific attenuation in this study, values of a_{ext} and b_{ext} computed by *Alonge* (2011) using Mie scattering technique are utilized. These values are shown in Table 5-1 over a frequency range from 2 GHz to 300 GHz.

Table 5.1: Extinction cross section power law coefficients for Durban at 20°C using Mie scattering technique [*Alonge,* 2011]

Frequency (GHz)	Complex Refractive Index	a_{ext}	b_{ext}
2	8.9014 + 0.4843*i*	0.0027	3.2737
4	8.7763 + 0.9442*i*	0.0191	3.7875
6	8.5830 + 1.3599*i*	0.0851	4.3988
8	8.3396 + 1.7196*i*	0.217	4.5805
10	8.0649 + 2.0188*i*	0.3857	4.5272
12	7.7755 + 2.2594*i*	0.5866	4.4443
15	7.3405 + 2.5234*i*	0.955	4.3453
18	6.9272 + 2.6934*i*	1.3883	4.2576
19.5	6.7332 + 2.7509*i*	1.6169	4.2104
20	6.6705 + 2.7667*i*	1.6936	4.194
25	6.1026 + 2.8532*i*	2.4567	4.0186
28	5.8107 + 2.8603*i*	2.8544	3.9035
30	5.6345 + 2.8532*i*	3.1204	3.8323
35	5.2500 + 2.8072*i*	3.7452	3.6639
40	4.9322 + 2.7383*i*	4.3106	3.5077
45	4.6668 + 2.6586*i*	4.8223	3.3646
50	4.4428 + 2.5752*i*	5.2855	3.2353
60	4.9322 + 2.7383*i*	6.0493	3.0094
70	3.8182 + 2.2560*i*	6.625	2.8209
90	3.4421 + 1.9907*i*	7.4097	2.5284
100	3.3061 + 1.8778*i*	7.6874	2.4156
150	2.9154 + 1.5083*i*	8.3061	2.0691
200	2.7103 + 1.2655*i*	8.3464	1.9293
250	2.5871 + 1.1051*i*	8.2291	1.8785
300	2.5029 + 0.9932*i*	8.0777	1.8672

5.3 Estimation of specific Attenuation over Durban

In this section and subsections thereafter, estimation of specific attenuation values are carried out using the drop size distribution as earlier mentioned in Section 5.1. The contribution of each drop size to the specific attenuation is calculated by integrating over each rain drop size, resulting from the expression [*Ajayi et al.,* 1996*; Alonge and Afullo,* 2012]:

$$A_S = 4.343 \times 10^{-3} \sum_{i=1}^{n} Q_{ext}(D_i) N(D_i).dD_i \qquad [dB/km] \tag{5.7}$$

where A_S is the specific attenuation, Q_{ext} is the extinction cross-section and $N(D_i).dD$ is the number density of the rain drop with equivalent diameter D in the interval dD.

In the computation of the specific attenuation using (5.7), the value of N(D) for each model that was developed in Chapter four were used in the estimation of specific attenuation resulting from each model.

Similarly, from measured rainfall DSD data at 30-seconds and 60-seconds, a correlation between the number of drops in the *i*th channel at 30-seconds integration time was derived from the corresponding *i*th channel at 60-second integration time. Therefore, following (4.44) – (4.45) and (5.7), the specific attenuation estimated using converted DSD from 60-second DSD is computed as:

$$A_{S,30s} = k \sum_{i=1}^{20} N(D_i)_{30s}. Q_{ext}(D_i). dD_i \qquad [dB/km] \tag{5.8}$$

and

$$N(D_i)_{30s} = \frac{C_{i,30-est}}{A \times T \times V_t \times dD_i} \tag{5.9}$$

where $N(D_i)_{30s}$ is the rain drop size distribution at 30-second integration time, $C_{i,30\text{-}est}$ is the number of estimated rain drops in the *i*th channel at 30s integration time, A is the disdrometer surface area, T is the sampling time in seconds, V_t is the rain drop fall velocity, dD_i the rain drop mean diameter and $k = 4.343 \times 10^{-3}$.

5.3.1 Estimation of specific attenuation from seasonal data

From seasonal data category, specific attenuation was determined for each of the four seasons over Durban and results for estimated specific attenuation values for selected frequencies of 10 GHz, 50 GHz, 100 GHz and 250 GHz were computed and presented in Table 5.2. It is to be noted that frequencies that are used in this table have no special significance attached, other than just elaboration purpose.

For the summer season, it is observed that specific attenuation estimates from measured rainfall DSDs are higher at 30-second integration time compared to their 60-second counterparts for same frequencies, except at 10 GHz. Alongside this table, Figure 5.1(a) also shows that the modified gamma model closely gives better estimates of specific attenuations, though with slightly higher values, at frequencies above

100 GHz. On the other hand, both lognormal models in summer season greatly underestimate the specific attenuation for frequencies above 50 GHz. At 60-second integration time, it is observed from Figure 5.1 (b) that all models other than LG-ML overestimates the specific attenuation.

In the autumn season, at 30-second integration time, it is observed that the Modified Gamma model gives better estimates than both lognormal models. From Figure 5.2 (a), it is observed that both lognormal models greatly underestimate the specific attenuation. At 60-second integration time, all models except the LG-ML give higher estimates for frequencies of 50 GHz and above, as shown in Figure 5.2 (b).

Similar to the season of autumn at 30-second integration time, the modified gamma model, though with slightly higher values, gives better estimates than other models in the season of spring at 30-second integration time. This is evident in Figure 5.3 (a). Again, in autumn season, the modified gamma model gives better estimates at 30-second integration time. Similarly, specific attenuation estimates at 60-second integration time are shown in Figure 5.3 (b). At this integration time, it is observed that the lognormal model (MM) gives better estimates for frequencies from 200 GHz and above.

In the winter season, better estimates are observed from the LG-MM model for frequencies below 100 GHz, at 30-second integration time. This is shown in Figure 5.4 (a). In this season, the modified gamma model gives lowest estimates before shifting positions with the LG-ML model at a frequency just below 150 GHz. Considering the specific attenuation range at 100 GHz for this season, at 30-second integration time, the lowest measured attenuation is 4.09 dB/km given by the modified gamma model while the highest is 10.97 dB/km, produced by the lognormal (MM). At 60-second integration time, all models give lower estimates as shown in Figure 5.4 (b).

A general observation from the four seasons shows that the seasons of summer and autumn results in higher values of specific attenuation compared to the seasons of spring and winter. These higher values can be explained by higher rainfall rates that are experienced during these two seasons over Durban.

Table 5.2 Specific Attenuation Estimation for different seasons over Durban

Seasons	*Freg.* (GHz)	**Seasonal Specific Attenuation [dB/km]**							
		30-second				60-second			
		Meas.	**LG-MM**	**LG-ML**	**GM-MM**	**Meas.**	**LG-MM**	**LG-ML**	**GM-MM**
Summer	10	0.41	0.22	0.81	0.42	0.68	0.19	0.33	0.57
	50	6.38	3.34	5.41	6.94	6.33	4.12	2.97	6.58
	100	11.92	5.82	5.74	12.83	8.32	8.70	3.80	9.72
	250	16.05	7.32	5.42	17.05	8.82	12.33	4.00	11.17
Autumn	10	0.40	0.19	0.80	0.49	0.50	0.36	0.26	0.47
	50	6.14	2.98	5.21	6.27	5.81	5.96	2.63	5.96
	100	10.29	5.29	5.41	9.91	8.46	10.49	3.65	9.40
	250	12.47	6.72	5.02	11.70	9.55	13.17	4.03	11.27
Spring	10	0.68	0.32	0.28	0.49	0.31	0.28	0.13	0.30
	50	5.25	4.95	2.33	4.87	4.72	4.64	1.59	4.78
	100	6.17	8.62	2.89	6.55	7.94	8.35	2.47	8.68
	250	6.31	10.86	2.99	7.07	9.78	10.68	2.93	11.40
Winter	10	0.37	0.33	0.64	0.20	0.54	0.49	0.38	0.59
	50	5.11	5.06	4.30	2.55	5.25	4.39	3.00	4.83
	100	8.06	8.87	4.57	4.09	7.21	5.26	3.52	5.66
	250	9.50	11.22	4.34	4.95	8.07	5.12	3.53	5.57

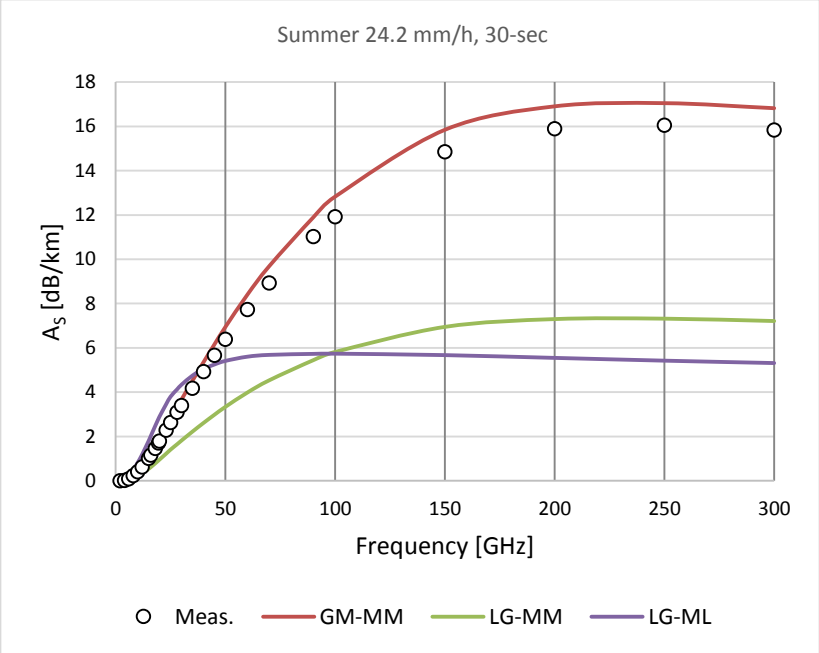

(a)

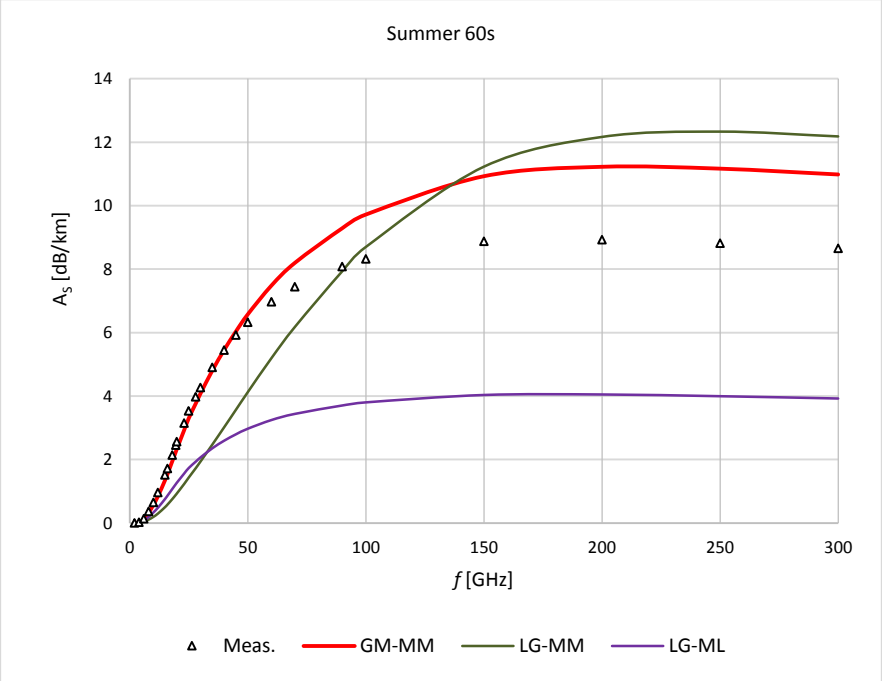

(b)

Figure 5.1 Specific attenuation estimation for Summer Season at (a) 30-second and (b) 60-second integration times

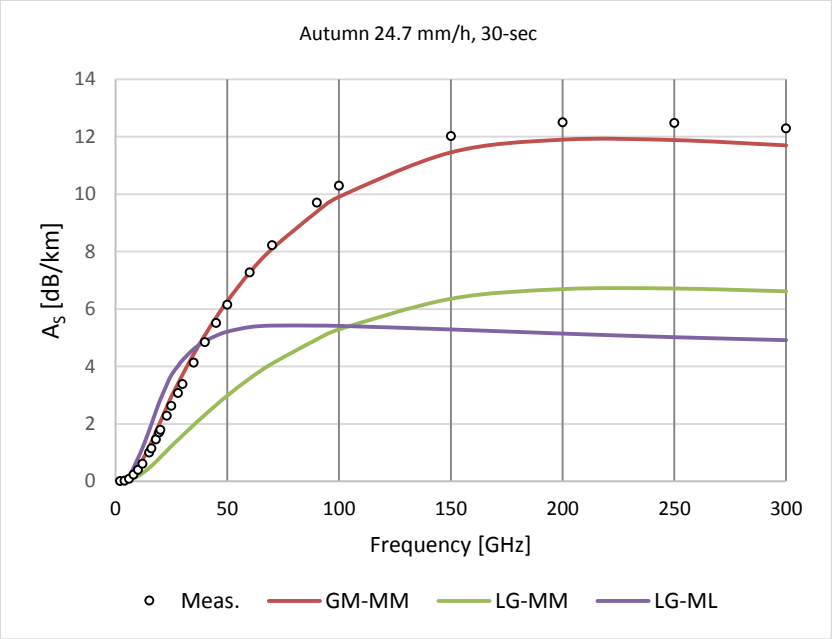

(a)

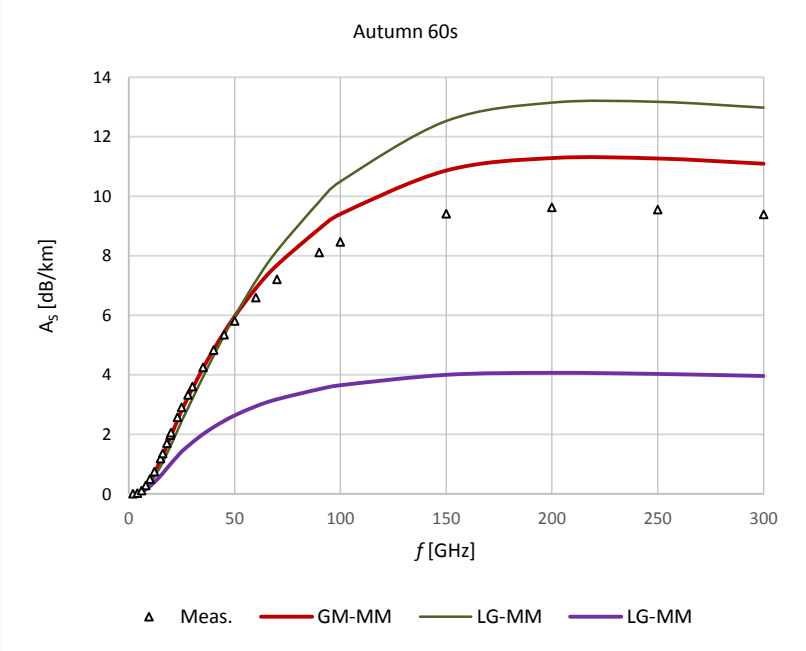

(b)

Figure 5.2 Specific attenuation for Autumn Season at (a) 30-second and (b) 60-second integration times

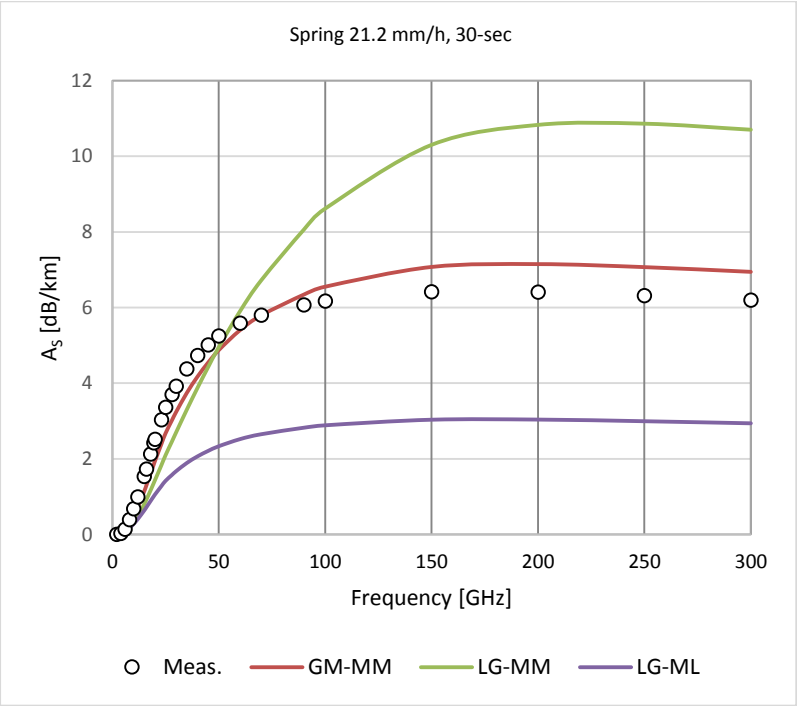

(a)

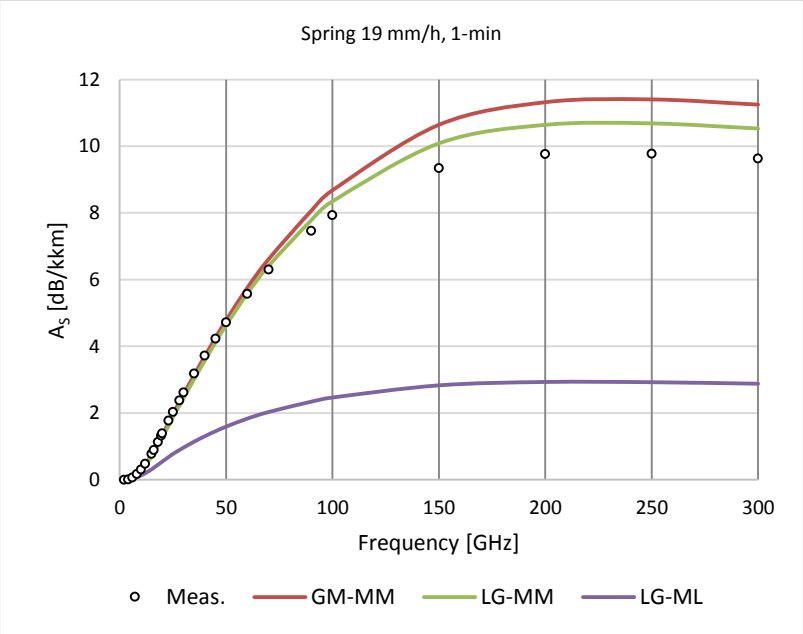

(b)

Figure 5.3 Specific attenuation for Spring Season at (a) 30-second and (b) 60-second integration times

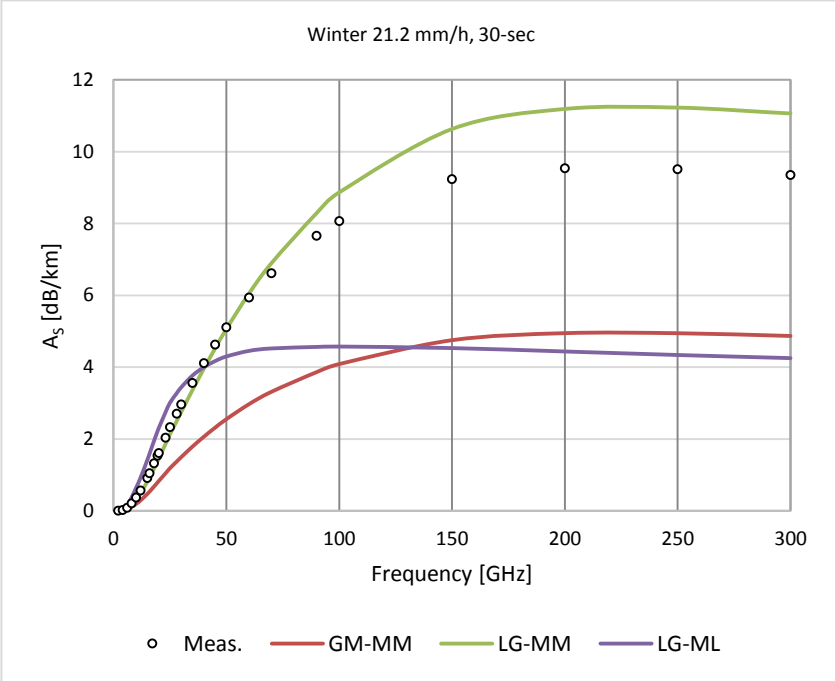

(a)

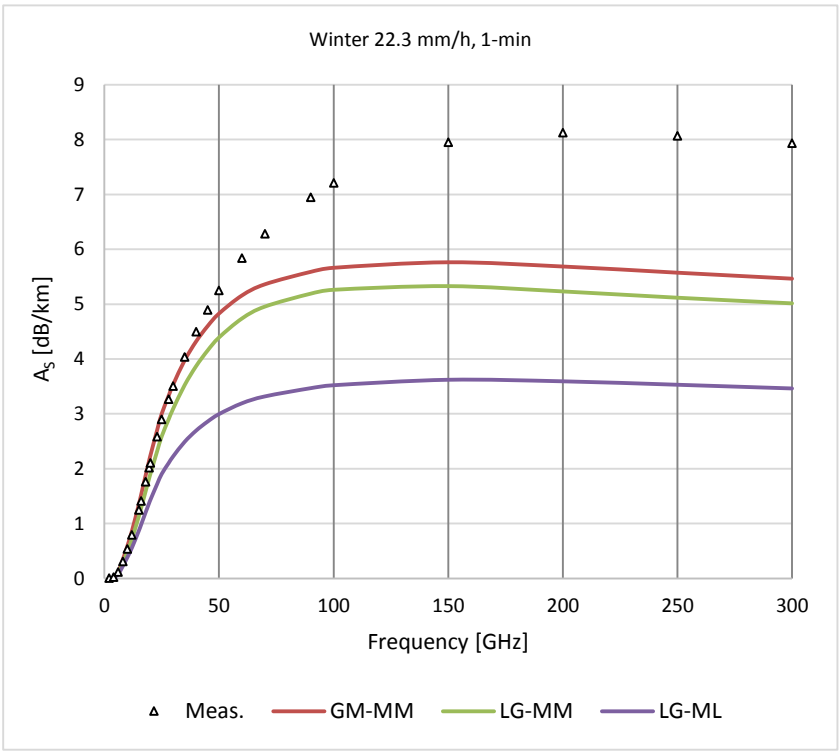

(b)

Figure 5.4 Specific attenuation for Winter Season at (a) 30-second and (b) 60-second integration times

5.3.2 Estimation of specific attenuation from annual data over Durban

Estimates of specific attenuation in this subsection are realized from the use of the expression given in (5.7) and rainfall DSD data measured and modeled at 30-second integration time and 60-second integration time. These estimates are carried out over frequencies from 2 GHz to 300 GHz and the results are presented in Table 5.3. Figure 5.5(a) and Figure 5.5(b) show model estimates at 30-second and 60-second integration times respectively, whereas in Figure 5.6, estimates at both integration times are presented for a general view on the trend of the estimated specific attenuation from all proposed models over Durban. An observation from Table 5.3 shows that specific attenuation increases with increase in frequency for frequencies from 2 GHz to 250, thereafter these estimates begin to decrease slowly as the frequency increases. Also, it is revealed from this table that estimates from the Gamma rainfall DSD are almost similar at both 30-second and 60-second integration times as is evident in Table 5.3 and Figure 5.6. From this figure, the two graphs completely overlap each other over the whole frequency range. Likewise, it is observed that the two ITU-R graphs overlap as they give better estimates for frequencies above 100 GHz.

Additionally, the influence of the integration time on specific attenuation estimation is also supported here. For example, it is observed that specific attenuation estimates from measured DSDs are higher at 30-second integration time compared to their counterparts at 60-second integration time and especially for frequencies above 100 GHz, as is revealed in Figure 5.6. For instance, there is a margin of 1.04 dB/km at 250 GHz between estimates from the two integration times as opposed to a margin of 0.66 dB/km at 100 GHz. Also, it is observed that both ITU-R models maintain a lead in overestimation of the specific attenuation at both integration times, with higher margins at frequencies below 150 GHz. This is evidenced in Figure 5.5 and Figure 5.6. Yet again, in consideration of the two integration times, it is interestingly noted that the Modified Gamma model gives same estimates of the specific attenuation over the whole of range of frequencies, as is noticed in Figure 5.6, in which the two graphs are completely overlapped.

Table 5.3 Specific Attenuation estimation for various models for 2 GHz $\leq f \leq$ 300 GHz and rainfall rate R = 61.2 mm/h

f (GHz)	Specific Attenuation [dB/km]									
	30s				60s				ITU-R P838-3	
	Meas.	LG-MM	LG-ML	GM-MM	Meas.	LG-MM	LG-ML	GM-MM	(H)	(V)
2	0.0075	0.0052	0.0065	0.0059	0.007	0.006	0.0063	0.0059	0.0068	0.0050
4	0.0598	0.0364	0.0574	0.0443	0.056	0.047	0.0552	0.0445	0.0779	0.0418
6	0.3212	0.1693	0.3469	0.222	0.289	0.228	0.3353	0.2228	0.4906	0.3160
8	0.8735	0.4412	0.9769	0.5913	0.776	0.601	0.9457	0.5934	1.2587	1.0094
10	1.5230	0.7788	1.6858	1.0372	1.358	1.0573	1.6313	1.0409	2.1498	1.6812
12	2.2494	1.1729	2.4503	1.5464	2.020	1.5837	2.3697	1.5518	3.1004	2.4828
15	3.5400	1.8892	3.783	2.4613	3.202	2.5347	3.6559	2.4697	4.5635	3.6799
16	4.0158	2.1578	4.2675	2.8013	3.641	2.8896	4.1232	2.8109	5.0635	4.0467
18	4.9988	2.7234	5.252	3.5105	4.551	3.6332	5.0721	3.5224	6.0765	4.7746
19.5	5.7337	3.1588	5.9694	4.0484	5.238	4.2011	5.7628	4.0620	6.8511	5.3444
20	5.9743	3.3041	6.2003	4.2263	5.464	4.3897	5.9848	4.2404	7.0981	5.5328
23	7.3300	4.1563	7.4539	5.2485	6.752	5.4839	7.1884	5.2657	8.6103	6.7601
25	8.2113	4.7337	8.2383	5.9269	7.598	6.2172	7.9400	5.9462	9.5961	7.6222
28	9.2287	5.467	9.0561	6.7501	8.600	7.1262	8.7189	6.7715	11.018	8.9419
30	9.8919	5.9593	9.5751	7.2947	9.255	7.7316	9.2123	7.3176	11.918	9.8142
35	11.363	7.1226	10.65	8.5435	10.730	9.1385	10.229	8.5695	13.974	11.87
40	12.602	8.1929	11.465	9.6457	11.980	10.403	10.992	9.6742	15.733	13.681
45	13.668	9.1859	12.102	10.634	13.060	11.553	11.583	10.664	17.199	15.219
50	14.606	10.112	12.62	11.531	14.020	12.608	12.059	11.563	18.39	16.52
60	16.094	11.721	13.328	13.029	15.530	14.395	12.695	13.064	20.106	18.549
70	17.183	13.041	13.74	14.201	16.620	15.813	13.049	14.237	21.203	19.978
90	18.701	15.085	14.166	15.94	18.080	17.934	13.387	15.978	22.321	21.684
100	19.278	15.903	14.303	16.621	18.620	18.762	13.488	16.660	22.594	22.149
150	20.736	18.240	14.437	18.489	19.850	21.018	13.518	18.528	22.914	22.756
200	20.942	18.859	14.21	18.909	19.930	21.526	13.264	18.948	22.650	22.377
250	20.706	18.800	13.919	18.78	19.660	21.385	12.977	18.818	22.190	21.907
300	20.340	18.500	13.644	18.466	19.300	21.028	12.718	18.503	21.739	21.437

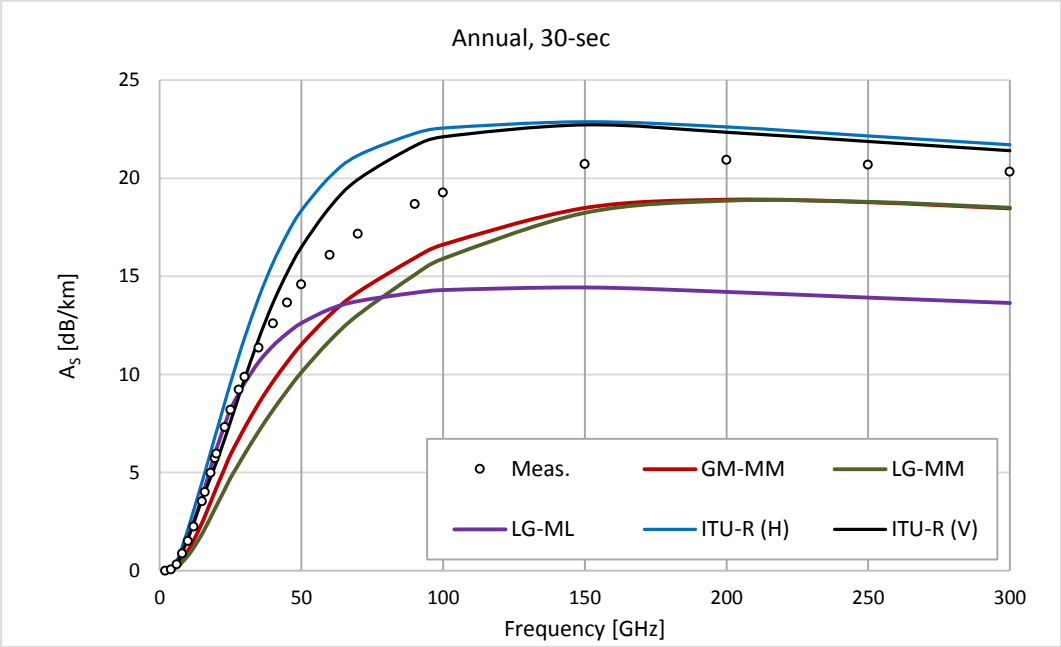

(a)

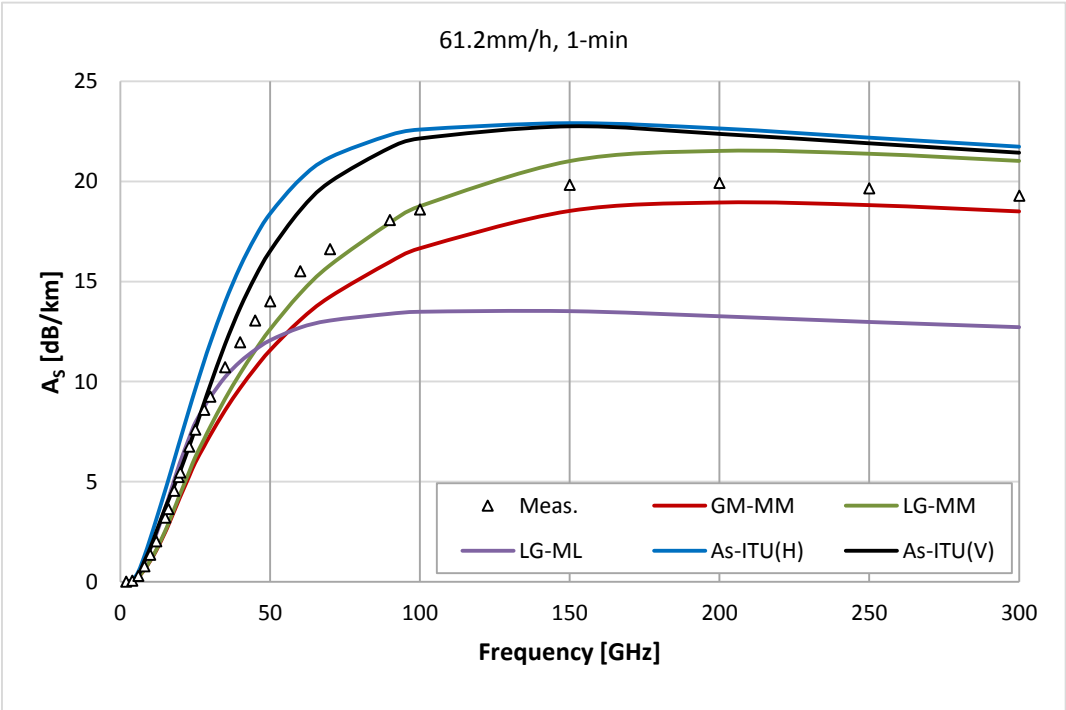

(b)

Figure 5.5 Specific Attenuation computed from annual data at (a) 30-second (b) 60-second integration times for rainfall rate R = 61.2 mm/h

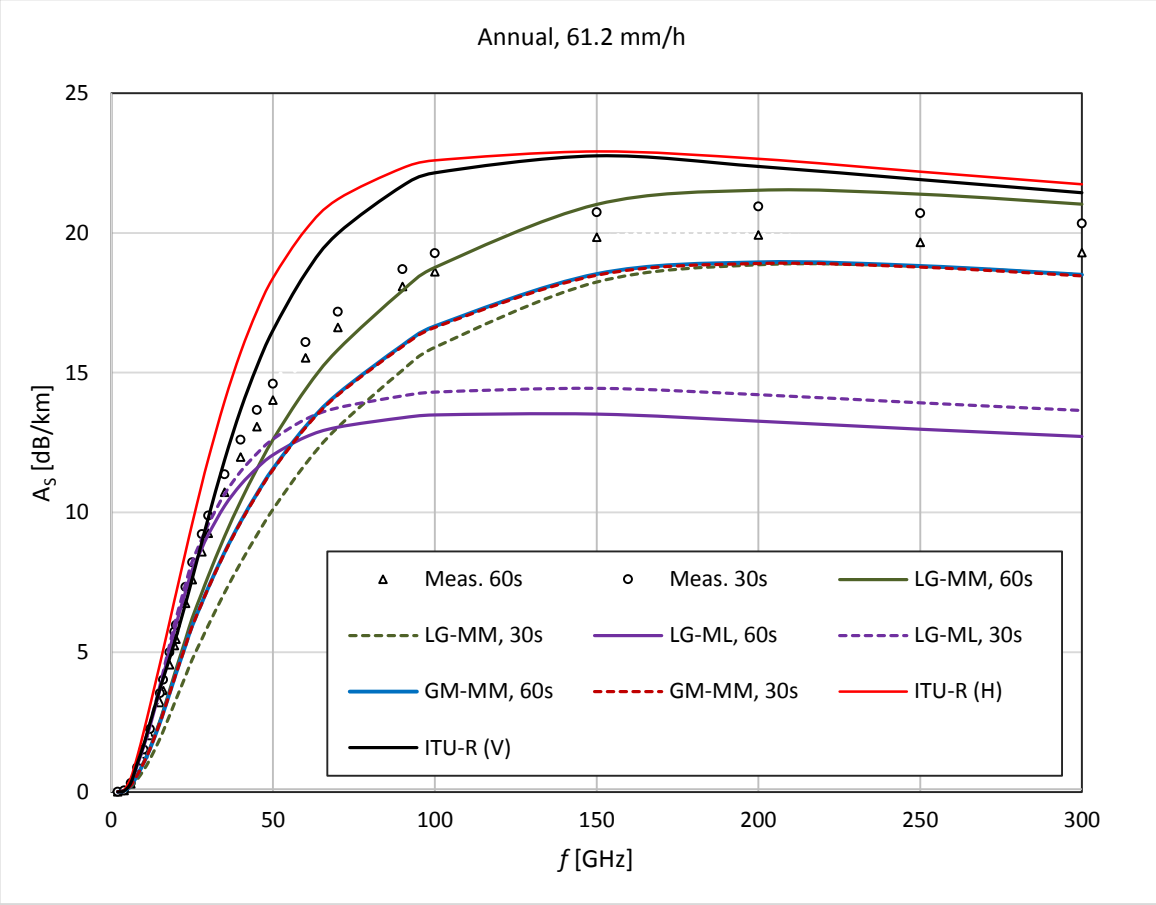

Figure 5.6 Specific Attenuation estimated from computed from annual data at both 30-second and 60-second integration times at a rainfall rate R = 61.2 mm/h

Specific attenuation estimates obtained from the Modified Gamma rainfall DSD model and the Lognormal model with Method of Moments parameter estimation technique were also fitted against selected frequencies in the range 2 GHz and 300 GHz. These fittings resulted in the generation of new k and α regression coefficient pairs for the two models, following the specific attenuation power-law function expressed in (2.31) as:

$$A_S = kR^{\alpha} \qquad [dB/km] \tag{2.55}$$

where k and α are frequency and temperature dependent regression coefficients.

The values of k and α shown in Table 5.4. From this table and Figure 5.7, it is observed that the coefficient k increases with increase in frequency. Also, it is observed that the lognormal model at 30-second

integration time has higher values of k for frequencies above 100 GHz, followed by the Modified Gamma model at 60-second integration time. On the other end, the Lognormal (MM) model at 30-second has lowest values of the k coefficient. For both ITU-R models, they overlap throughout the whole frequency range.

In Figure 5.8, the coefficient α increases sharply in magnitude with increase in frequency up to about 8 GHz and thereafter starts to decrease slowly with further increase in frequency. This is observed for all models except for the two ITU-R models which peak earlier at 6 GHz, with the ITU-R (H) giving rise to the highest peak of the coefficient α. But as much as ITU-R models give highest peaks, their graphs descend faster and acquire the lowest values α for frequencies above 20 GHz.

Table 5.4 Determination of regression coefficients k and α for various models for Durban at 20°C

Freq. [GHz]	**Coefficients k and α**							
	Lognormal - MM				Modified Gamma			
	k_{30s}	α_{30s}	k_{60s}	α_{60s}	k_{30s}	α_{30s}	k_{60s}	α_{60s}
2	0.0002	0.8857	0.0002	0.8954	0.0003	0.9249	0.0002	1.0535
4	0.0008	0.9801	0.0008	0.9807	0.0016	1.0067	0.0011	1.1596
6	0.0025	1.0960	0.0024	1.0854	0.0055	1.0947	0.0035	1.2797
8	0.0057	1.1312	0.0055	1.1172	0.0130	1.1191	0.0081	1.3142
10	0.0105	1.1208	0.0102	1.1079	0.0236	1.1120	0.0147	1.3041
12	0.0168	1.1048	0.0163	1.0934	0.0370	1.1009	0.0234	1.2884
15	0.0290	1.0857	0.0285	1.0761	0.0626	1.0874	0.0402	1.2694
18	0.0446	1.0689	0.0439	1.0609	0.0943	1.0753	0.0613	1.2525
20	0.0567	1.0568	0.056	1.0499	0.1181	1.0663	0.0775	1.2401
25	0.0921	1.0235	0.0919	1.0199	0.1847	1.0412	0.1243	1.2057
30	0.1322	0.9885	0.1333	0.9882	0.2556	1.0135	0.1765	1.1686
35	0.1778	0.9571	0.1808	0.9599	0.3330	0.9877	0.2352	1.1345
40	0.2278	0.9283	0.2335	0.9339	0.4153	0.9631	0.2994	1.1025
45	0.2818	0.9022	0.2914	0.9103	0.5019	0.9399	0.3683	1.0727
50	0.3386	0.8788	0.3517	0.8891	0.5917	0.9184	0.4410	1.0454
60	0.4567	0.8383	0.4794	0.8526	0.7746	0.8798	0.5926	0.9969
70	0.5755	0.805	0.6092	0.8224	0.9556	0.8465	0.7464	0.9556
90	0.8049	0.7541	0.8628	0.7764	1.3030	0.7928	1.0485	0.8901
100	0.9120	0.7347	0.9822	0.7589	1.4655	0.7714	1.1921	0.8643
150	1.3000	0.6762	1.4194	0.7058	2.0615	0.7038	1.7299	0.7832
200	1.4650	0.653	1.6078	0.6848	2.3199	0.6756	1.9697	0.7497
250	1.5064	0.6446	1.6564	0.6771	2.3857	0.6653	2.0340	0.7375
300	1.4926	0.6427	1.6419	0.6755	2.3641	0.663	2.0173	0.7347

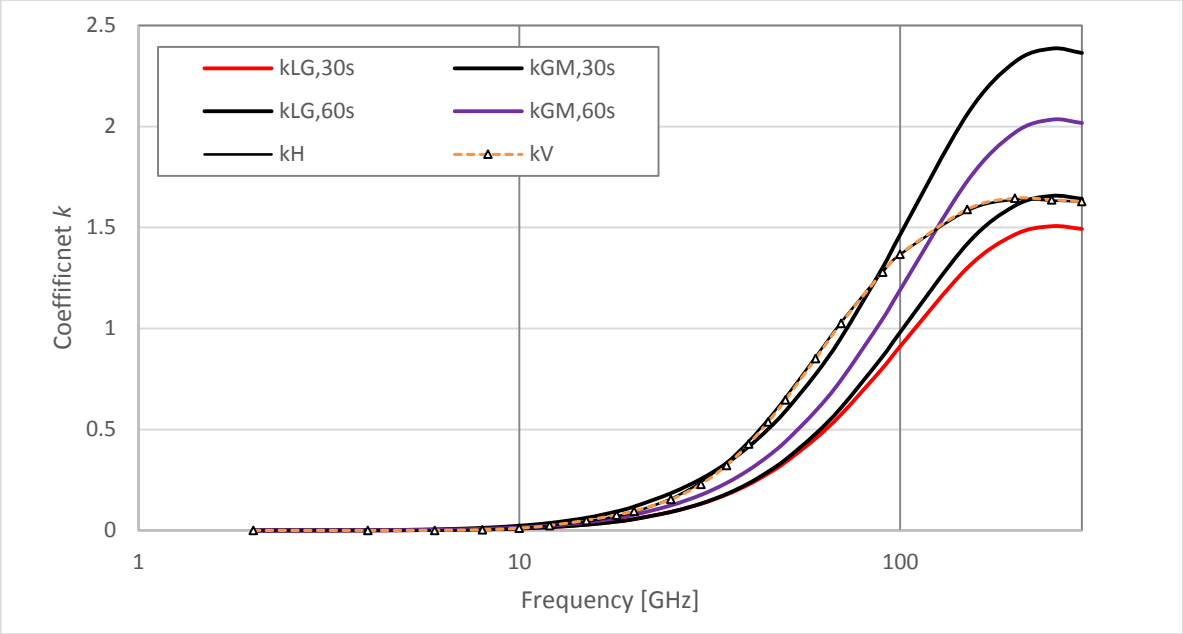

Figure 5.7 Variation of coefficient *k* with frequency over Durban at 20°C

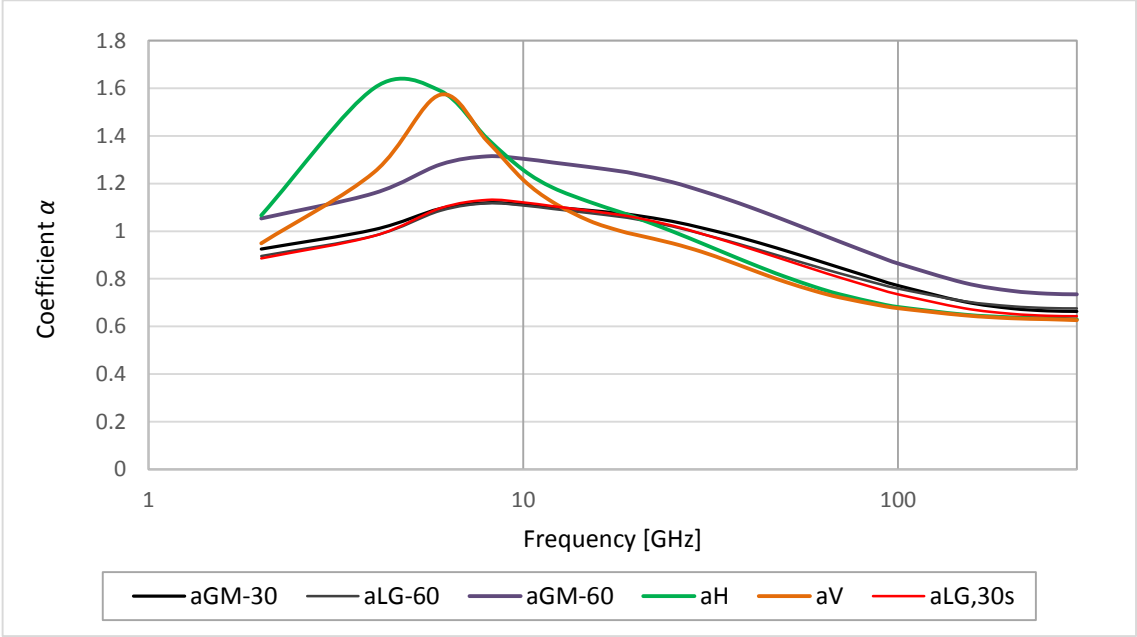

Figure 5.8 Variation of coefficient α and frequency over Durban at 20°C

5.4 Error Analysis on Annual Models

The Root Mean Square Error technique was carried out on specific attenuation estimates that were obtained from proposed models over Durban to find the suitability of models on seasonal and annual rainfall statistics. Results of the error analysis are represented in Tables 5.5, Table 5.6 and Table 5.7. Error analysis on specific attenuation due to seasonal variations is presented in Table 5.5. From this table, it is observed that the modified gamma model gives the lowest RMSE value of 0.0702 and 0.1294 for summer season at 30-second and 60-second integration times, respectively.

In autumn season, the trend of results is almost similar to the summer season, with the Modified Gamma model, yet still, giving the lowest RMSE values of 0.1274 and 0.0807 at both 30-second and 60-second respectively.

In spring, it is yet again observed that the modified gamma model gives better estimates, followed by the lognormal (MM) model at both integration times. The RMSE values resulting from the lognormal model are 0.1818 and 0.0721 at 30-second and 60-second integration times respectively. Corresponding values for the lognormal (MM) model are 0.4299 and 0.0782.

In the fourth season, winter, the lognormal (MM) model is the best model with closest estimates. This model results in the RMSE value of 0.1006 followed by the lognormal (ML) model with a value of 0.4401, at 30-second integration time. At 60-second integration time, the modified gamma gives better estimates followed by the lognormal (MM) model with RMSE values of 0.1446 and 0.1897 respectively.

In Table 5.6, error analysis results are presented for annual DSD variations at frequencies from 2 GHz to 300 GHz over Durban. Out of the five models considered, ITU-R (V) model gives better estimates at 30-second integration times with RMSE value of 0.1265, followed closely by lognormal (MM) with a value of 0.1638. At 60-second integration time, the modified gamma model is the best choice with RMSE value of 0.0481 followed by ITU-R (V), with a value of 0.1633.

Regression coefficient k and α, shown in Table 5.4, were also subjected to error analysis and their results are summarized in Table 5.7. From this table, it is established that for the coefficient k, the modified gamma results in lowest RMSE values at both integration times. For the coefficient α, the modified gamma gives better estimates at 30-second integration times, whereas at 60-second integration time, the lognormal (MM) model gives better estimates.

Table 5.5 Error analysis on specific attenuation due to seasonal variations

Int. Time (sec)	Seasons	Lognormal Model		gamma (MM) model	Suitable Model
		MM	**ML**		
30	Summer	0.4848	0.5858	0.0702	modified gamma
	Autumn	0.5143	0.5640	0.1274	modified gamma
	Spring	0.4299	0.5640	0.1818	modified gamma
	Winter	0.1006	0.4401	0.4877	lognormal - MM
60	Summer	0.5150	0.5193	0.1294	modified gamma
	Autumn	0.2145	0.5284	0.0807	modified gamma
	Spring	0.0782	0.6279	0.0721	modified gamma
	Winter	0.1897	0.4069	0.1446	modified gamma

Table 5.6 Specific Attenuation Error Analysis on annual data for frequencies 2 GHz to 300 GHz

Integration Time (sec)	**Model**	**RMSE**	**Suitable Model**
30s	LG-MM	0.3664	ITU-R (V)
	LG-ML	0.1638	
	GM-MM	0.2804	
	ITU-R (H)	0.2523	
	ITU-R (V)	0.1265	
60s	LG-MM	0.2235	modified gamma
	GM-MM	0.1857	
	GM-MM	0.0481	
	ITU-R (H)	0.3503	
	ITU-R (V)	0.1633	

Table 5.7 Error analysis on coefficients k and α on proposed models

Integration Time (sec)	Model	Coefficients	
		k_m	α_m
30s	LG-MM	0.9270	0.1850
	GM-MM	0.8750	0.1661
60s	LG-MM	0.9231	0.1679
	GM-MM	0.9041	0.2046

5.5 Chapter Summary

In this chapter, specific attenuation estimates were obtained from proposed rainfall DSD models over Durban at frequencies from 2 GHz to 300 GHz. From seasonal error analysis, it is observed that the modified gamma model performs better than the two lognormal models for all seasons except in winter, where the lognormal (MM) model gives better estimates. For annual DSD models error analysis, an observation shows that the ITU-R (V) model generates lower RMSE error of 0.1265 and becomes the better model at 30-second integration time, followed by the lognormal (MM) model with an error value of 0.1633. In general all models proposed gave estimates closer to measured specific attenuation.

In the next chapter, the conclusion of the study will be presented, together with recommendations for future work.

CHAPTER 6

Conclusion and Further Work

6.1 Conclusion

For design and implementation of more reliable microwave communication systems with minimal signal outages, design engineers require more accurate information on rainfall rates exceeded for a fraction of an average year. This information is crucial in estimation of rainfall attenuation on microwave and millimeter links operating at frequencies above 10 GHz.

In Chapter three, using cumulative distributions obtained from measured data, rainfall rate conversion models for 10 locations over South Africa were successfully determined using the power-law function. Error analysis on the proposed models indicate that these new models can be relied on in the conversion of available 5-minute data to one-minute and 30-second data for planning of reliable microwave communication systems over South Africa.

In Chapter four, lognormal and modified gamma rainfall DSD model parameters were estimated using the method of moments and the maximum likelihood methods. These proposed models were then used to generate rainfall distributions for various data categories. Error analysis on the derived models revealed that the modified gamma model is best suited for rainfall measurements above 10 mm/h at 60-second. At 30-second integration time, the modified gamma model still preferred for mid rain rates of 10 mm/h < R < 80 mm/h, with the lognormal DSD model being suited for lower rainfall rates less than 10 mm/h and at high rainfall rates above 80 mm/h. Also, the DSD conversion model for channel-to-channel drop conversion from 60-second to 30-second was successfully implemented in this chapter.

In Chapter five, results of specific attenuation estimates from semi-empirical measurements and proposed rainfall DSD models showed a close match. From seasonal data analysis, it is observed that the modified gamma model performs better than the two lognormal models for all seasons except in winter. From the analysis of annual data, it was revealed that the ITU-R (V) model gives better specific attenuation estimates at 30-second integration time, whereas at 60-secon integration time, estimates closer to semi-empirical specific attenuation values were given by lognormal (MM) model.

6.2 Suggestions for Future Work

- More extensive research using rainfall data measured at 30-second integration time is recommended for more conclusive results on both rainfall rates and drop size distribution behaviors.

- The number of localities with disdrometer data measurements should be increased for availability of rainfall DSD data so that investigations on rainfall DSD studies can be extended to other locations with different climatic conditions.

References

Afullo, T. J. O., 2011, "Raindrop size distribution modelling for radio link design along the eastern coast of South Africa," Progress In Electromagnetics Research B, Vol. 34, 345-366.

Ajayi, G. O. and Ofoche E.B.C., 1984: "Some Tropical Rain Rate Characteristics at Ile-Ife for Microwave and Millimeter Wave Applications," Journal of Climate and Applied Meteorology, Vol. 23, 562-567.

Ajayi, G. O., and R. L. Olsen, 1985: "Modelling of a tropical raindrop size distribution for microwave and millimeter wave applications," Radio Science, Vol. 20, No. 2, 193-202, Apr.

Ajayi, G. O., and I. A. Adimula, 1996: Variations in raindrop size distribution and specific attenuation due to rain in Nigeria, *Ann. Telecommun.*, 51(1–2), 87–93.

Ajayi, G. O., S. Feng, S. M. Radicella and B.M. Reddy (1996): Handbook on Radio Propagation Related to Satellite Communications in tropical and sub-tropical countries. ICTP, Trieste. 7-14.

Akintunde A. Alonge, 2011: "Correlation of Rain Dropsize Distribution With Rain Rate Derived from Disdrometers and Rain Gauge Networks in Southern Africa," Msc. Eng. Thesis, University of KwaZulu-Natal, South Africa, Dec.

Akuon P. O., and T. J. O. Afullo, 2011: "Rain cell sizing for the design of high capacity radio link systems in South Africa," Progress in Electromagnetics Research B, Vol.35, 263-285.

Alonge A. A. and T. J. Afullo, 2012a: "Regime analysis of rainfall drop-size distribution models for microwave terrestrial networks," IET Microwave, Antennas and Propagat., Vol. 6 (4).

Alonge A. A. and T. J. Afullo, 2012b: "Seasonal analysis and prediction of rainfall effects in eastern South Africa at Microwave Frequencies," Progress in Electromagnetics Research B, Vol. 40, 279-303.

Alonge A. A. and T. J. O. Afullo, 2014: "Rainfall Microstructural Analysis for Microwave Link Networks: Comparison at Equatorial and Subtropical Africa," Progress In Electromagnetics Research B, Vol. 59, 45-58.

Alonge, A. A., 2011: "C*orrelation of rain dropsize distribution with rain rate derived from disdrometers and rain gauge networks in Southern Africa*, Msc. Thesis, University of KwaZulu Natal, South Africa.

Alonge, A.A. and T. J. O. Afullo, 2012: "Prediction of Specific Attenuation of Rain for Wireless Networks by Probability Density Analysis in South Africa," SATNAC, 2012

Altshuler, E. E., 1984: "A simple expression for estimating attenuation by fog at millimeter wavelengths," IEEE Transactions on Antennas and Propagation, Vol. AP-32, No. 7, 757-758.

Asiyo, M. and Thomas J. O. Afullo, 2013: "Statistical Estimation of fade depth and outage probability due to multipath propagation in Southern Africa," Progress in Electromagnetics Research B, Vol. 46, 251-274.

Atlas, D. and C.W. Ulbrich, 1974: 'The physical basis for attenuation-rainfall relationships and the measurement of rainfall parameters by combined attenuation and radar methods,' *J. Rech.Atmos.*, 8, pp. 275–298.

Bartholomew, M. J. (2009): Disdrometer and tipping bucket raingauge handbook, DOE/SC-ARM/TR-079, ARM Climate Research Facility.

Bohren, C.F. and D.R. Huffman (2004): Absorption and scattering of light particles, Wienheim:

Chebil, J. and T. A. Rahman (1999), "Development of 1min rain rate contour maps for Microwave applications in Malaysia Peninsula," Electronics Letts., Vol.35, 1712-1774.

Chun, O. W. and J. S. Mandeep, "Empirical Methods for converting rainfall rate distribution from several higher integration times into a 1-minute integration time in Malaysia," GEOFIZIKA, Vol.30, 144-154, 2013

Cioni, S. R. De Gaudenzi, and R. Rinaldo, 2004: "Adaptive coding and modulation for the reverse link of broadband satellite networks," in *IEEE Global Telecommunications Conference*, vol. 2, 1101–1105

Cioni, S., R. D. Gaudenzi, and R. Rinaldo, 2003: "Adaptive coding and modulation for the forward link of broadband satellite networks," in *IEEE Global Telecommunications Conference*, vol. 6, 3311–3315.

Conradie, D. C. U. 2012: "South Africa's Climatic Zones: Today, Tomorrow," International Green Building Conference and Exhibition.

Crane, R. K. (1996): Electromagnetic Wave Propagation through Rain, Wiley Interscience, New York.

Crane, R. K. (2003): Propagation Handbook for Wireless Communication System Design, CRC Press, New York.

Crane, R. K., 1977: "Stratospheric Turbulence", Rep No. AFGL. TR. 77-0207. Air Force Geophys. Lab., Hanscom AFB, Massachusetts.

Crane, R.K., "Prediction of Attenuation by Rain," IEEE Trans. Commun., Vol.28, No.6, 1717-1733, 1980

Crane, R.K., 1985: "Evaluation of Global and CCIR models for estimation of rain rate statistics," *Radio Science*, Vol.20, No.4, 865-879.

Das, S., A. Maitra and A. K. Shukla, 2010: "Rain attenuation modelling in the 10-100 GHz frequency using drop size distributions for different climatic zones in Tropical India," Progress In Electromagnetics Research B, Vol. 25, 211-224.

Dissanayake A., J. Allnutt and F Haidara, 1997: "A prediction Model that combines Rain Attenuation and other propagation impairments along earth-satellite paths," IEEE Transactions and Propagation, Vol. 45, No. 10, Oct.

Dissanayake, A, J. Allnutt and F. Haidara (2002), "A prediction model that combines rain attenuation and other propagation impairments along earth-satellite paths," Online Journal of Space Communication, Issue No. 2, 1-29.

Distromet system (2000), The Joss-Waldvogel Disdrometer Handbook, Basel, Switzerland.

Dutton, E. J., Dougherty, H. T. and Martin Jr., R. F., 1974: "Prediction of European rainfall and link performance coefficients at 8 to 30 GHz," Techn. Report No. ACC-ACO-16-74, Office of Telecommunications, U. S. Dept. of Commerce.

Elbert, B. R. (2008). *Satellite Communication Applications Handbook*, Second Edition, Artech House Inc., USA

Elbert, B. R., (2004): Satellite Communication Applications Handbook, Artech House, USA.

Emiliani D. L., L. Luini, and C. Capsoni (2009), "Analysis and parameterization of methodologies for the conversion of rain rate cumulative distributions from various integration times to one minute," IEEE Antennas and Propagation Magazine, Vol.51, No.3, pp. 70-84.

Fashuyi, M. O. and T. J. Afullo, 2007: "Rain attenuation and modelling for line-of-sight links on terrestrial paths in South Africa," Radio Science, Vol. 42, RS5006, doi:10.1029/2007RS003618, pp. 1-15.

Federal Communications Commission (FCC), (1997), *Millimeter Wave Propagation: Spectrum Management Implications,* Bulletin, Number 70, USA

Feingold, G. and Z. Levin, 1986: "The lognormal fit to raindrop spectra from frontal convective clouds in Israel," *J. Appl. Meteorol*., 25, 1346–1364.

Flavin, R. K. (1982), "Rain attenuation considerations for satellite paths," Telecom Australia Research Laboratories Report No 7505.

Freeman, R. L., (2007): Radio System Design for Telecommunications, John Wiley and Sons, New York.

Garcia, A. L., (2008): Probability, Statistics, and Random Processes for Electrical Engineering, 3rd Ed. Prentice Hall, USA.

Goddard, J, W. F. (2011): Propagation in Rain and clouds, in *Propagation of Radiowaves*, ed. Les Barclay, Institution of Electrical Engineers, UK.

Green, H.E., "Propagation on Ka-Band SATCOM Links in Tropical and Equatorial Regions," IEEE Antennas and Propagation Magazine,Vol. 46, No.2, 31-43, 2004

Ippolito, L. J. Jr., 2008: Satellite Communications Systems Engineering: Atmospheric Effects, Satellite Link Design and System Performance, John Wiley and Sons Ltd, UK.

Islam, M. R. UI, T. A. Rahman, S. K. A. Rahim, K. F. Al-Tabatabaie and A. Y. Abdulrahman (2009), " Fade margins prediction for broadband fixed wireless access (BFWA) from measurements in tropics," Progress In Electromagnetics Research C, Vol. 11, pp. 199-212.

ITU-R F.1703 Recommendation (2005), "Availability objectives for real digital fixed wireless links in 27,500 km hypothetical reference paths and connections," Geneva.

ITU-R P.530-15, 2013: "Propagation data and prediction methods required for the design of terrestrial line-of-sight systems," Recommendation, Geneva.

ITU-R P.618-11 (2013), "Propagation data and prediction methods required for the design of Earth-space telecommunication systems," Recommendation, Geneva.

ITU-R P.618-11, 2013: "Propagation data and prediction methods required for the design of Earth-space telecommunication systems," Recommendation, Geneva.

ITU-R P.837-1, 1994, "Characteristics of precipitation for propagation modelling," Recommendation, Geneva.

ITU-R P.837-4 2003: "Characteristics of precipitation for propagation modelling," Recommendation, Geneva.

ITU-R P.837-5, 2007: "Characteristics of Precipitation for Propagation Modelling," Recommendation, Geneva.

ITU-R P.837-6, 2012: "Characteristics of Precipitation for Propagation Modelling," Recommendation, Geneva.

ITU-R P.838-3, 2005: "Specific attenuation model for use in prediction methods," Recommendation, Geneva.

Jones, D. M. A. and A. L. Sims (1978). "Climatology of Instantaneous Rainfall Rates", Journal of Applied Meteorology, Vol. 17, pp. 1135-1140.

Kozu, T. and K. Nakamura 1991: "Rainfall parameter estimation from dual-radar measurements combining reflectivity profile and path-integrated attenuation," *J. of Atmos. and Oceanic tech.*, 259–270.

Kumar, L.S. and Y.H. Lee, 2010: "Shape Slope parameter distribution modelling for electromagnetic scattering by rain drops," Progress In Electromagnetics Research B, Vol. 25, 191-209.

Kumar, L.S., Y.H. Lee, J.X. Yeo, J.T. Ong, "Tropical Rain classification and estimation of rain from Z-R (Reflectivity-Rain Rate) Relationships," Progress in Electromagnetics Research B, Vol. 32, 107-127, 2011.

Laskshmi S. K., Y. H. Lee and J. T. Ong (2010), "Truncated gamma drop size distribution models for rain attenuation in Singapore," IEEE Trans Antennas Propag (USA), 58 (4), pp. 1325-1335.

Liebe, H.J., G.A. Hufford and T. Manabe (1991): 'A model for the complex permittivity of water at frequencies below 1 THz,' *Inter. J. of Infrared and Millimeter Waves*, 12 (7), 659–678.

Liebe, H.J., Takeshi Manabe, George A. Hufford (1989), "Millimeter-wave attenuation and delay rates due to fog/cloud conditions," IEEE Transactions on Antennas and Propagation, Vol.37, No. 12

Malinga, S. J., P. A. Owolawi and T. J. O. Afullo, 2013: "Computation of rain attenuation through scattering at microwave and millimeter bands in South Africa," Progress in Electromagnetics Research Symposium Proceedings, Taipei, pp. 959-971.

Massambani, O. and C.A.M. Rodriguez (1990): 'Specific attenuation as inferred from drop size distribution measurements in the tropics,' *Proc. URSI Comm. F. Sym. on Regional Factors in predicting Radiowave Attenuation*, Rio de Janeiro, Brazil, pp. 25-28.

Matricciani, E., 2011: "A mathematical theory of de-integrating long-time integrated rainfall and its application for predicting 1-min rain rate statistics," International Journal of Satellite Communications and Networking, 29 (501-530).

Medeiros Filho, F. C, R. S. Cole and A. D. Sarma, 1986: "Millimeter-wave induced attenuation: Theory and Experiment," IEEE Proc., part H, Microwave Antennas Propag., 133(4), 308-314.

Mie, G. (1908): 'Beiträge zur optik trüber medien, speziell kolldaler metallösungen,' *Ann. Phys*.,25, pp. 377–445, doi:10np.19083300302.

Milda Tamošiunaite, Stasys Tamošiunas, Mindaugas Žilinskas and Milda Tamošiuniene (2011): Atmospheric Attenuation due to Humidity, in *Electromagnetic Waves*, ed Vitaliy Zhurbenko, ISBN: 978-953-307-304-0, InTech, Croatia, pp. 157-172

Misme, P and J Fimbel (1975), "Determinatin theoretique et experimentale de l'afflaiblissement par la pluie sur un trajet radiolectrique," Ann. Telecommn., 30, pp. 149-158.

Moupfouma, F, and S. Martins (1995), "Modeling of the rainfall rate cumulative distribution for design of satellite and terrestrial communication systems," International Journal of Satellite Communication, 13(2) 105-115

Moupfouma, F., 1987: "More about rainfall rates and their prediction for radio systems," IEEE Proceedings, Vol. 134 (6), Pt. H, 527-537.

Naicker, K., 2006: Rain attenuation modelling for line-of-sight terrestrial links, M.Sc thesis,School of Electrical, Electronics and Computer Engineering, Uni. of KwaZulu-Natal,Durban, South Africa. Sept.

Ojo, J. S., M. O. Ajewole and L.D. Emiliani (2009), "One-Minute Rain-Rate Contour Maps for Microwave-Communication-System Planning in a Tropical Country: Nigeria," IEEE Antennas and Propagation Magazine, Vol.51, No. 5, pp. 82-89.

Ojo, J.S., M.O. Ajewole, and S.K. Sarkar (2008), "Rain rate and rain attenuation Prediction for Satellite Communication in Ku and Ka Bands Over Nigeria," Progress In Electromagnetics Research B, Vol.5, 207-223.

Olsen, R. L., D. V. Rogers, and D. B. Hodge, 1978: "The aR^b relation in the calculation of rain attenuation," IEEE Trans. Antennas Propagat., vol. AP-26, pp. 318-329.

Olsen, R.L. 1999: "Radioclaimatological Modelling of Propagation Effects in Clear-Air and Precipitation Conditions: Recent Advances and Future Directions," Radio Africa.

Ooi, C. W. and J. S. Mandeep, 2013: "Empirical methods for converting rainfall rate distribution from several higher integration times into a one-minute integration time in Malaysia," GEOZIFIKA, Vol. 30, pp. 143-154.

Owolawi P. A., T. J. Afullo and S. B. Malinga, 2009: "Effect of rainfall on millimeter wavelength radio in Gough and Marion Islands," Progress in Electromagnetics Research Symposium, Beijing, China, March 23-27.

Owolawi, P. A., 2011: "Derivation of one-minute rain rate from five-minute equivalent for the calculation of rain attenuation in South Africa," PIERS Online, Vol.7, No.6, pp 524-535.

Rappaport, T. S., (1996): Wireless Communications: Principles and Practice, Prentice Hall, Englewood Cliffs, NJ, USA.

Rappaport, T. S., R. W. Heath Jr., R. C. Daniels and J. N. Murdock (2015*).* Millimeter Wave Wireless Communications, Pearson Education, Inc., USA.

Rice, P.L. and N.R. Holmberg (1973), "Cumulative Time Statistics of Surface-Point Rainfall Rates," IEEE Transactions on Communications, Vol. COM-21, No. 10, 1131-1136.

Rodgers, D. V. and R. L. Olsen (1976), "Calculation of radiowave attenuation due to rain at frequencies up to 1000 GHz," Commun., Res. Cent. Rep. 1299, Ottawa Ont., Canada, Nov.

Rubel, F. and M. Kottek, 2010: "Observed and Projected Climate Shifts 1901-2100 Depicted by World Maps of the Köppen-Geiger Classification," Meteorologische Zeitschrift, Vol. 10(2), pp. 135-141.

Segal, B. (1986), "The Influence of the Raingauge Integration Time on measured Rainfall-Intensity Distribution Functions", Journal of Atmospheric and Oceanic Technology, Vol. 3, 662-671.

Soong, T.T., (2004): Fundamentals of probability and statistics for engineers, John Wiley & Sons, USA.

Tamošiunaite, M., S. Tamošiunas, M. Žilinskas and M. Tamošiuniene, (2011): Atmospheric Attenuation due to Humidity, in *Electromagnetic Waves*, ed Vitaliy Zhurbenko, ISBN: 978-953-307-304-0, InTech, Croatia, pp. 157-172

Timothy K.I., J. T. Ong and E. B. I. Choo, 2002: "Raindrop size distribution using methods of moments for terrestrial and satellite communication applications in Singapore," IEEE Transactions on Atennas and Propagation, Vol. 50, No. 10, 140-1424.

Ulbrich, C.W. (1983): 'Natural variation in the analytical form of the raindrop size distribution,' J. of *Climate and Applied Meteor.*, vol. 23, pp. 1764–1775.

Van der Hulst, H.C. (1957): Light scattering by small particles, John Wiley and Sons Inc., New York.

Wang, J., B.L. Fisher and D.B. Wolff (2006): "Estimating rain rates from tipping-bucket rain measurements," Journal of Atmospheric and Oceanic Technology.

Watson, P.A., V. Sathiaseelan and B. Potter, 1982: "Development of a Climatic map of rainfall attenuation for Europe," No. 300, 134, Post Graduate School of Electrical and Electronic Engineering, University of Bradford, U.K.

Williams, C. R. and K. S. Gage, 2009: "Raindrop Size Distribution variability estimated using ensemble statistics," Ann. Geophys., Vol. 27, 555-567,

Yakubu, M. L., Z. Yusop and F. Yusof, 2014: "The modelled raindrop size distribution of Skudai, Peninsular Malaysia, using exponential and lognormal distributions," *The Scientific World Journal*, Vol. 2014, Article ID 361703, 1-7.

Zhang, G. J., J. Vivekanandan and E. Brandes, 2000: "A method of estimating rain rate and drop size distribution from polarimetric radar measurements." IEEE Transactions on Geoscience and Remote Sensing Conference.

Appendices

Appendix A

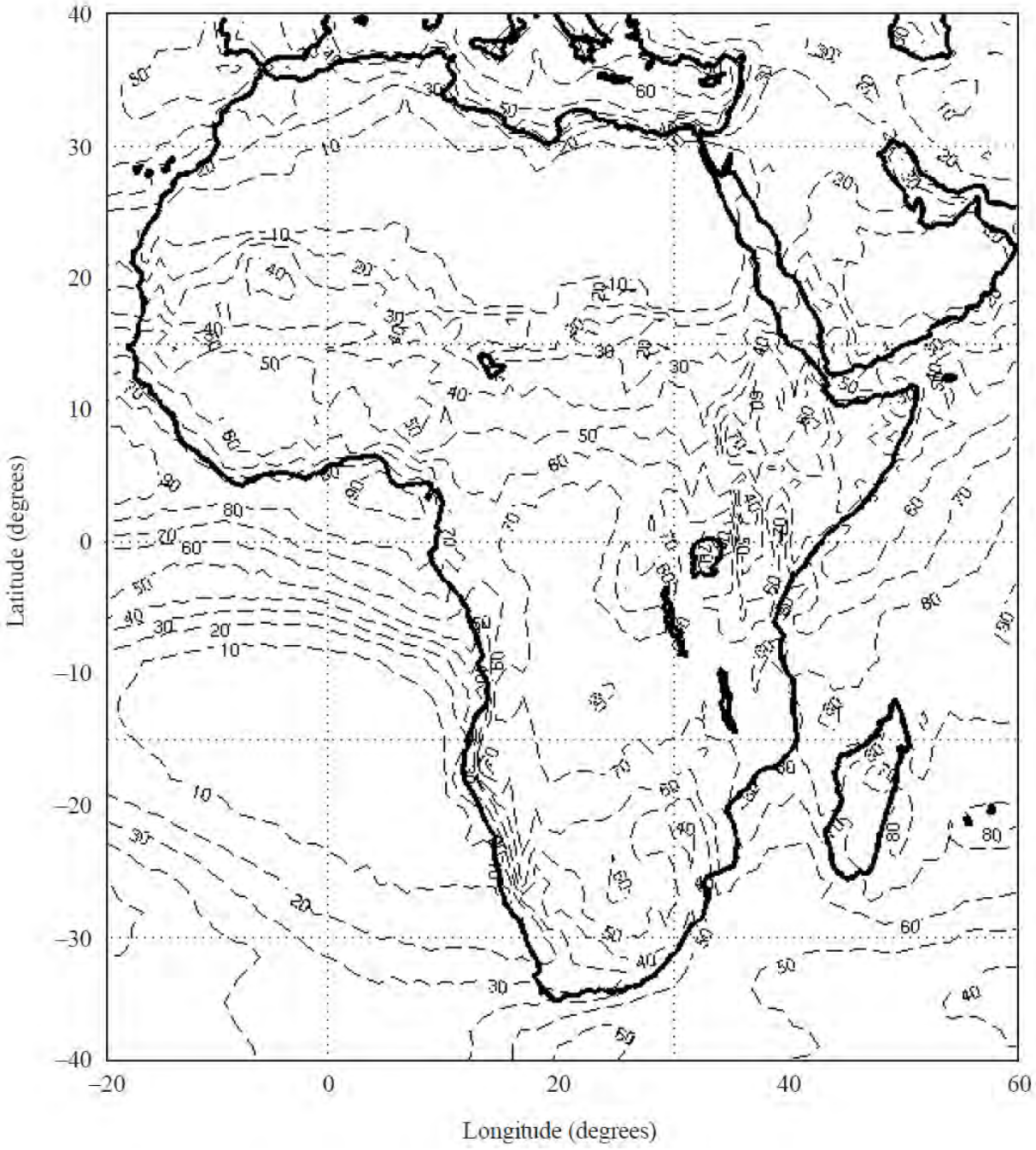

Figure A-1 Rain rate (mm/h) exceeded for 0.01% of the average year

Table A-1 Rainfall Rate intensity exceeded (mm/h) [ITU-R P.837-6, 2012]

Percentage of time (%)	A	B	C	D	E	F	G	H	J	K	L	M	N	P	Q
1.0	<0.1	0.5	0.7	2.1	0.6	1.7	3	2	8	1.5	2	4	5	12	24
0.3	0.8	2	2.8	4.5	2.4	4.5	7	4	13	4.2	7	11	15	34	49
0.1	2	3	5	8	6	8	12	10	20	12	15	22	35	65	72
0.03	5	6	9	13	12	15	20	18	28	23	33	40	65	105	96
0.01	8	12	15	19	22	28	30	32	35	42	60	63	95	145	115
0.003	14	21	26	29	41	54	45	55	45	70	105	95	140	200	142
0.001	22	32	42	42	70	78	65	83	55	100	150	120	180	250	170

Appendix B

Table B-1 Frequency-dependent coefficients for estimation of specific rain attenuation [ITU-R P.838-3, 2005]

Frequency (GHz)	k_H	α_H	k_V	α_V
1	0.0000259	0.9691	0.0000308	0.8592
1.5	0.0000443	1.0185	0.0000574	0.8957
2	0.0000847	1.0664	0.0000998	0.9490
2.5	0.0001321	1.1209	0.0001464	1.0085
3	0.0001390	1.2322	0.0001942	1.0688
3.5	0.0001155	1.4189	0.0002346	1.1387
4	0.0001071	1.6009	0.0002461	1.2476
4.5	0.0001340	1.6948	0.0002347	1.3987
5	0.0002162	1.6969	0.0002428	1.5317
5.5	0.0003909	1.6499	0.0003115	1.5882
6	0.0007056	1.5900	0.0004878	1.5728
7	0.001915	1.4810	0.001425	1.4745
8	0.004115	1.3905	0.003450	1.3797
9	0.007535	1.3155	0.006691	1.2895
10	0.01217	1.2571	0.01129	1.2156

Table B-1 Cont'd

Frequency (GHz)	k_H	α_H	k_V	α_V
11	0.01772	1.2140	0.01731	1.1617
12	0.02386	1.1825	0.02455	1.1216
13	0.03041	1.1586	0.03266	1.0901
14	0.03738	1.1396	0.04126	1.0646
15	0.04481	1.1233	0.05008	1.0440
16	0.05282	1.1086	0.05899	1.0273
17	0.06146	1.0949	0.06797	1.0137
18	0.07078	1.0818	0.07708	1.0025
19	0.08084	1.0691	0.08642	0.9930
20	0.09164	1.0568	0.09611	0.9847
21	0.1032	1.0447	0.1063	0.9771
22	0.1155	1.0329	0.1170	0.9700
23	0.1286	1.0214	0.1284	0.9630
24	0.1425	1.0101	0.1404	0.9561
25	0.1571	0.9991	0.1533	0.9491
26	0.1724	0.9884	0.1669	0.9421
27	0.1884	0.9780	0.1813	0.9349
28	0.2051	0.9679	0.1964	0.9277
29	0.2224	0.9580	0.2124	0.9203
30	0.2403	0.9485	0.2291	0.9129
31	0.2588	0.9392	0.2465	0.9055
32	0.2778	0.9302	0.2646	0.8981
33	0.2972	0.9214	0.2833	0.8907
34	0.3171	0.9129	0.3026	0.8834
35	0.3374	0.9047	0.3224	0.8761
36	0.3580	0.8967	0.3427	0.8690
37	0.3789	0.8890	0.3633	0.8621
38	0.4001	0.8816	0.3844	0.8552
39	0.4215	0.8743	0.4058	0.8486
40	0.4431	0.8673	0.4274	0.8421
41	0.4647	0.8605	0.4492	0.8357
42	0.4865	0.8539	0.4712	0.8296
43	0.5084	0.8476	0.4932	0.8236
44	0.5302	0.8414	0.5153	0.8179
45	0.5521	0.8355	0.5375	0.8123
46	0.5738	0.8297	0.5596	0.8069
47	0.5956	0.8241	0.5817	0.8017
48	0.6172	0.8187	0.6037	0.7967

Table B-1 Cont'd

Frequency (GHz)	k_H	α_H	k_V	α_V
49	0.6386	0.8134	0.6255	0.7918
50	0.6600	0.8084	0.6472	0.7871
51	0.6811	0.8034	0.6687	0.7826
52	0.7020	0.7987	0.6901	0.7783
53	0.7228	0.7941	0.7112	0.7741
54	0.7433	0.7896	0.7321	0.7700
55	0.7635	0.7853	0.7527	0.7661
56	0.7835	0.7811	0.7730	0.7623
57	0.8032	0.7771	0.7931	0.7587
58	0.8226	0.7731	0.8129	0.7552
59	0.8418	0.7693	0.8324	0.7518
60	0.8606	0.7656	0.8515	0.7486
61	0.8791	0.7621	0.8704	0.7454
62	0.8974	0.7586	0.8889	0.7424
63	0.9153	0.7552	0.9071	0.7395
64	0.9328	0.7520	0.9250	0.7366
65	0.9501	0.7488	0.9425	0.7339
66	0.9670	0.7458	0.9598	0.7313
67	0.9836	0.7428	0.9767	0.7287
68	0.9999	0.7400	0.9932	0.7262
69	1.0159	0.7372	1.0094	0.7238
70	1.0315	0.7345	1.0253	0.7215
71	1.0468	0.7318	1.0409	0.7193
72	1.0618	0.7293	1.0561	0.7171
73	1.0764	0.7268	1.0711	0.7150
74	1.0908	0.7244	1.0857	0.7130
75	1.1048	0.7221	1.1000	0.7110
76	1.1185	0.7199	1.1139	0.7091
77	1.1320	0.7177	1.1276	0.7073
78	1.1451	0.7156	1.1410	0.7055
79	1.1579	0.7135	1.1541	0.7038
80	1.1704	0.7115	1.1668	0.7021
81	1.1827	0.7096	1.1793	0.7004
82	1.1946	0.7077	1.1915	0.6988
83	1.2063	0.7058	1.2034	0.6973
84	1.2177	0.7040	1.2151	0.6958
85	1.2289	0.7023	1.2265	0.6943
86	1.2398	0.7006	1.2376	0.6929

Table B-1 Cont'd

Frequency (GHz)	k_H	α_H	k_V	α_V
87	1.2504	0.6990	1.2484	0.6915
88	1.2607	0.6974	1.2590	0.6902
89	1.2708	0.6959	1.2694	0.6889
90	1.2807	0.6944	1.2795	0.6876
91	1.2903	0.6929	1.2893	0.6864
92	1.2997	0.6915	1.2989	0.6852
93	1.3089	0.6901	1.3083	0.6840
94	1.3179	0.6888	1.3175	0.6828
95	1.3266	0.6875	1.3265	0.6817
96	1.3351	0.6862	1.3352	0.6806
97	1.3434	0.6850	1.3437	0.6796
98	1.3515	0.6838	1.3520	0.6785
99	1.3594	0.6826	1.3601	0.6775
100	1.3671	0.6815	1.3680	0.6765
120	1.4866	0.6640	1.4911	0.6609
150	1.5823	0.6494	1.5896	0.6466
200	1.6378	0.6382	1.6443	0.6343
300	1.6286	0.6296	1.6286	0.6262
400	1.5860	0.6262	1.5820	0.6256
500	1.5418	0.6253	1.5366	0.6272
600	1.5013	0.6262	1.4967	0.6293
700	1.4654	0.6284	1.4622	0.6315
800	1.4335	0.6315	1.4321	0.6334
900	1.4050	0.6353	1.4056	0.6351
1 000	1.3795	0.6396	1.3822	0.6365

Appendix C

Table C-1 RD-80 Disdrometer Bin Catalogue [*Bartholomew*,2005; www.disdromet.com].

Drop size class in DISDRODATA program	Lower threshold of drop diameter [mm]	Average diameter of drops in *i*th class D_i [mm]	Fall velocity of a drop $v(D_i)$ [m/s]	Diameter interval of drop size *i*th class ΔD_i [mm]
1	0.313	0.359	1.435	0.092
2	0.405	0.455	1.862	0.1
3	0.505	0.551	2.267	0.091
4	0.596	0.656	2.692	0.119
5	0.715	0.771	3.154	0.112
6	0.827	0.913	3.717	0.172
7	0.999	1.116	4.382	0.233
8	1.232	1.331	4.986	0.197
9	1.429	1.506	5.423	0.153
10	1.582	1.665	5.793	0.166
11	1.748	1.912	6.315	0.329
12	2.077	2.259	7.009	0.364
13	2.442	2.584	7.546	0.286
14	2.727	2.869	7.903	0.284
15	3.011	3.198	8.258	0.374
16	3.385	3.544	8.556	0.319
17	3.704	3.916	8.784	0.423
18	4.127	4.35	8.965	0.446
19	4.573	4.859	9.076	0.572
20	5.145	5.373	9.137	0.455